UNIVERSITÀ DEGLI STUDI DI PADOVA

Dipartimento di Fisica e Astronomia "Galileo Galilei"

Master Degree in Physics

Final Dissertation

Optical absorption of Si at 1550 nm at cryogenic temperatures

Thesis supervisor

Prof. Marco Bazzan

Thesis co-supervisor

Prof. Jean-Pierre Zendri

Candidate

Graziano Pascale

Academic Year 2021/2022

Introduction

Recent direct observations of gravitational waves have not only provided further confirmation of Einstein general relativity but also paved the way for a new way of observing the sky. Since the beginning of astronomy, the understanding of the universe was based only on the observation of the electromagnetic components of the spectrum. While the strong interaction of photons with matter makes these particles easily detectable, on the other hand the information they carry is easily polluted or blocked by the presence of another matter / energy between the source and the observer. In this perspective, the weakness of the gravitational interaction becomes an advantage because it allows you to probe space-time regions of the universe that are normally inaccessible. The price to pay is the great difficulty in making tools capable of revealing their passage. Indeed, the direct detection of gravitational interaction involves resorting to unconventional types of observation. Today's detection method is mainly based on two principles: resonance of solid objects and the measurement of the contraction / expansion of the distances between two or more masses.

To improve the signal-to-noise ratio of these detections, a new generation (third generation) of gravitational interferometers has been devised.

The project in Europe that will deal with the development of these third-generation interferoemters is the Einstein Telescope project (ET), a European Union project.

In order to fulfill the sensitivity requirements of a third generation detector, it will be necessary to operate the Low Frequency interferometer of the Einstein Telescope in a cryogenic environment. This will set a new technological challenge, as the substrate materials and coatings that are currently used in optical elements of second generation GW interferometers will be made unusable in a cryogenic environment due to increased mechanical losses.

Research in recent years has led to say that a suitable candidate to serve as substrate material in test masses of the Low Frequency detector of ET could be crystalline silicon.

This thesis work will contribute to the charaterization of silicon optical properties in the same environment that is designed for the ET-LF detector. In this document it will be illustrated the design and construction of an experiment that allows to measure the optical absortion coefficient of crystalline silicon at cryogenic temperatures at the foreseen ET operation wavelenght λ = 1550nm. This kind of measurement is a non trivial task due to the very small magnitude of optical absorption in silicon, that ultimately makes it a favourable candidate as a test mass substrate material. The absorption coefficient of silicon α_{Si} obtained in this work be compared to the only existing measurement of α_{Si} in analogous environmental conditions that is currently present in literature and the consequences of this results on the Einstein Telescope design will be analyzed.

Contents

Part I

Chapter 1

Gravitational wave background

The history of gravitational waves and their detection begins in 1916 [1]. They were initially theorized similarly to the electromagnetical waves in an early work on Special Relativity by Henri Poincarè, but they found their first rigorous mathematical description soon after the publication of the Theory of General Relativity, thanks to the effort of Albert Einstein that was able to find a wave-like solution to its field equations in a specific coordinate system. Yet Einsten himself was doubtful of the physicality of his solutions and his feelings were confirmed few years later when Sir. Arthur Eddington proved that two of the three of these wave solutions had a frame dependent propagation speed, so that they were a mere artifact of a wavy coordinate system. Hence Einstein reinforced his belief that gravitational waves were unphysical and went on to spread his opinion across the whole scientific community during the decades preceeding World War II.

During 1930s Einstein and Rosen published various theoretical papers demonstrating the unphysicality of wave-like solutions to the GR Equations that were eventually proven wrong by the work of H.P. Robertson. Despite Einstein admitting his mistake, Gravitational Waves remained an exotic subject among the physics community. During '50s the debate focused on whether or not Gravitational Waves would carry energy, but the dispute remained on theoretical ground as there were no experiment attempting at detecting them. This skewed state of affairs started to change after the Chapel Hill conference on General Relativity in January 1957. During the meeting devoted to Gravitational Waves, Richard Feynman persuaded the audience of their reality thanks to its famous 'Sticky Bead Argument'[1], finally settling the theoretical debate on the GW existence. One of the members of the audience happened to be Joseph Weber, an engineer from Maryland University that, fascinated by the topic, began to think about an experimental device that could achieve their detection.

  Weber was the pioneer in the search for gravitational wave signals. In a 1960 paper [2] he summarized his ideas about the most promising strategies for their detection and during the following years he worked on the construction of the first Gravitational Wave Antenna, the 'Weber Bar', that begun the first data taking attempt in 1966 [3]. The Weber Bar consisted in a big aluminum cylinder with $66\,\mathrm{cm}$ diameter and $153\,\mathrm{cm}$ lenght, for a total wheight of around $3\,\mathrm{tons}$, suspended to a system aimed to insulate the mass from enviromental vibrations. The bar was enveloped by a strip of quartz transducers that converted mechanical strains to voltage signals and the whole system was sealed in a vacuum chamber.

This particular type of detector takes advantage of the resonance frequency of a mechanical system: if a gravitational wave with frequency that match exactly the resonant frequency of the bar passes through the detector with direction of propagation that is non-parallel to the bar axis, one could hope that the induced strain on the bar will be amplified enough to overcome the enviromental noises, hence

---

[1]In Feynman's thought experiment, a gravitational wave detector simply consist of two beads sliding freely on a rigid rod, oriented transversely to the propagation direction of the wave. As the gravitational wave passes, it exerts tidal forces on the objects respect to the center of the bar. Atomic forces hold the length of the rod fixed, instead nothing prevents the beads from sliding. If there's friction between the rod and the beads, heat will be dissipated in the process. Then, the energy source can only be the gravitational wave.
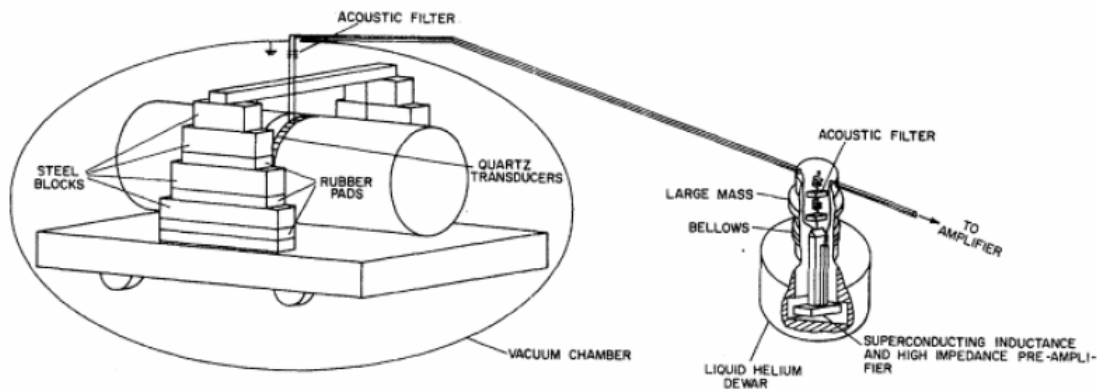
Figure 1.1: Up: Joseph Weber at work on one of his early resonant bar detector prototypes.
Down: Scheme of the apparatus of the first Weber Bar [3]

becoming detectable. Unfortunately, this approach proved to be inefficient at detecting gravitational signals. The main problem with a resonant bar detector is the fact that its sensitivity is peaked only in a narrow frequency region around the mechanical resonant frequencies of the system, so that, in order for a gravitational signal to be detectable, not only it should have large amplitude, but it should also peak its power at the exact frequency requested by the detector. Moreover, the technologies that were implemented in this early prototype detectors were inadequate to achieve a sufficient peak sensitivity to detect even the most optimistic gravitational wave event. Despite this fact, Weber was the first to understand the importance of having a global array of detectors that permits to reject local spurious signals based on coincidences, as he built two copies of his first prototype that were placed in two laboratories at a distance of $950\,\mathrm{km}$. Moreover his attempts prompted a fast development in the experimental field of gravitational wave searches in the following decades as many groups of scientists rushed to indepently check Weber's measurement that claimed several Gravitational Wave signals that conflicted with the contemporary understanding of astronophysical processes, eventually ruling them out. The peak sensitivity for resonant bar detectors was reached in the late-'90s/early-2000s with the NAUTILUS and AURIGA ultracryogenic bar antennae at the INFN laboratories, Frascati and Legnaro respectively, in Italy (Fig.1.2).

As the sensitivity of resonant bar detectors was improving, it became clear that Weber's method wasn't the optimal one for gravitational wave detection. There was a more promising strategy instead that
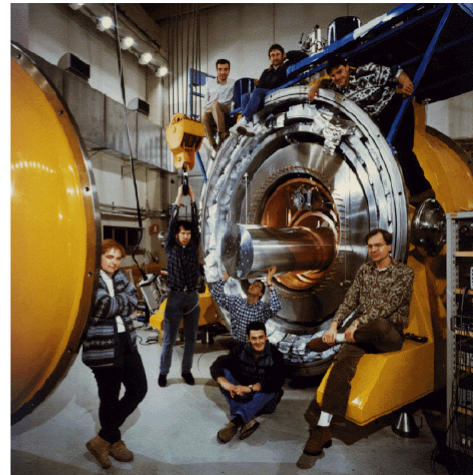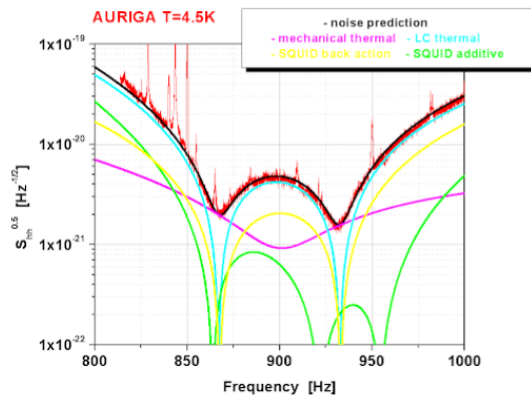
Figure 1.2: Left: Sensitivity of the AURIGA Detector, 2004. Right: Open Section of the AURIGA at the Laboratori Nazionali di Legnaro.

started developing in the 1970s: laser interferometry. The interferometric idea was nothing new between experimental physicist but it was applied for the first time to gravitational wave serches only in the early 70's, thanks to the independent efforts of Robert L. Forward [4] and Rainer Weiss [5]. In particular it was Weiss that, after having worked on an initial 1.5-m prototype at MIT and having contributed to the 30-m interferometer realized by the Garching group in Munich, Germany, laid the foundation for the LIGO (Laser Interferometer Gravitational-Wave Observatory) Project, a set of two 4-km long Michelson interferometers placed more than $3000\,\mathrm{km}$ apart at Hanford, WA and Livingstone, LA.

The LIGO large-scale interferometers were the first one to be built, as their construction started in 1994, but they were followed soon after by the VIRGO detector, a 3-km long Michelson interferometer built in Cascina, IT by a INFN-CNFR collaboration starting from the late '90s. These three detectors, togeter with the german GEO600 and the japanese TAMA, constituted the first generation of Gravitational Wave Interferometers, with the respective arm lengths of 600m and 300m. The initial version of the two LIGO interferometers started data acquisition in 2002, while VIRGO was fully operating for the first time in 2007. These early 2000s observation runs had the aim of testing a range of new technologies that were applied for the first time to large-scale interferometers and did not succeded in gravitational wave detection. Consequently the detectors were shut down between 2010 and 2011 to allow for the upgrade to their improved version, aLIGO (Advanced LIGO) [6] and AdV (Advanced VIRGO) [7] respectively. The upgraded detectors aimed for a factor 10 sensibility improvement respect to the initial versions, establishing the second generation of Gravitational Wave Interferometers. Sensitivies of these advanced gravitational wave detector reached values below $10^{-23}\sqrt{1/\mathrm{Hz}}$ accross a wide range of frequencies (Fig.1.3), a value that was expected to be comparable to the amplitudes of GW signals coming from nearest compact object inspiral events. More importantly, this was the frequency range inside which gravitational wave signals from most of Bynary systems of Black Holes (BBH) and Neutron Stars (BNS) peaked their amplitude during mergers, so that the first gravitational wave event was eventually detected on September 14, 2015 by the aLIGO detector[2] [8], in the exact year of the 100th anniversary of the General Relativity Theory publication.

In the few years following the first gravitational wave detection a variety other signal were observed. A total of three observation runs has been conducted between 2015 and 2020, the last two of which the three detectors were able to operate simultaneously. To have at least three working interferometers is

---

[2]The first gravitational wave signal, GW150914, was observed by the aLIGO detector only, while it was still in 'engeneering' operational mode (its first official observation run would have started four days later, on September 18, 2015). The AdV detector started its first observation run on August 1, 2017.
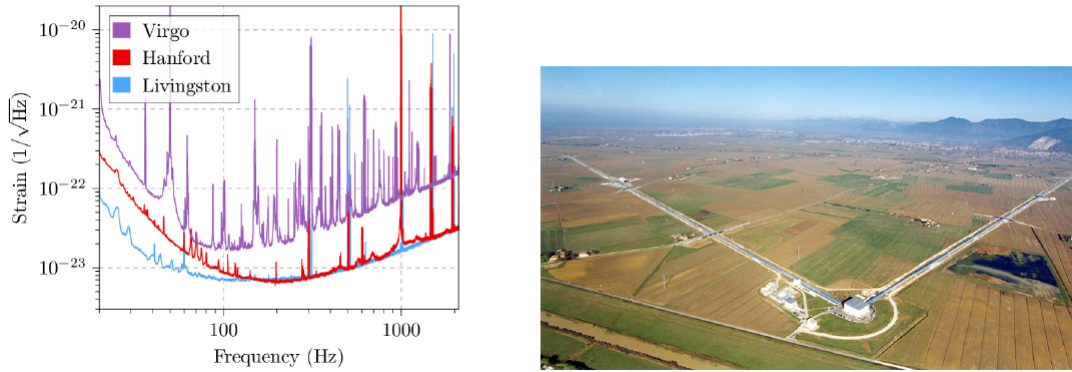
Figure 1.3: Left: Noise Spectral Density of the LIGO and VIRGO Detectors, September 2017. Right: Aerial View of the VIRGO interferometer in Santo Stefano a Macerata, IT.

crucial for triangulating the position in the sky of the signal source and it also allows to perform a better noise rejection based on multiple coincidences. During the first two runs a total of 11 gravitational wave events have been succesfully observed and the results of the first half of the third observation run has just been published, confirming the observation of 39 more GW signals, adding to a total of 50 detected merger events [9]. The majority of this events are Black Hole-Black Hole Mergers, but also two Neutron Star-Neutron Star Mergers were detected, for the first of which (GW170817) it was also detected the Electro-Magnetical counterpart of the gravitational wave signal, starting the era of multimessenger (EM-GW) astronomy [10].

Then, the Advanced LIGO and VIRGO detectors culminated the lenghty and winding hunt for gravitational waves, proving the physical existence of the fascinating space-time ripples. The number of GW events that are being digged out from the noisy interferometrical read-out signal of the three detectors is constantly increasing and this experimental findings are stimulating a multitude of theoretical and numerical reasearch to extensively test the General Relativity Theory along with expanding the current knowledge in the fields of Astrophysics, Cosmology and Fundamental Physics by directly observing the most powerful cosmic collisions.

In the coming years a new upgrade that will take the aLIGO and AdV detectors to their maximal design sensitivity is scheduled, but the three detector are already approaching their physical upper sensitivity bound. In order to understand where do the physical limitations to the aLIGO and AdV detector sensitivities come from and which strategies should be pursued to overcome them in a new generation of Gravitational Wave Interferometers, it is necessary to understand the theoretical framework of gravitational wave signals and their consequences on massive systems and the space-time fabric itself.

Chapter 2

Gravitational Waves in General Relativity

2.1 Einstein field equation

Einstein's special relativity describes the motion of bodies in inertial frames of reference; space-time is described with a flat metric by the Minkowsky tensor $\eta_{\mu\nu}$. In this perspective, the space-time interval between two separate events is given by:

$$ds^2 = \eta_{\mu\nu}dx^\mu dx^\nu$$

. In general relativity the non-inertiality of the reference systems results in a curvature in space-time, induced by the presence of matter-energy. This manifests itself in the form of the force of gravity; in Einstein's perspective, the gravitational field is given by the tensor equation that bears his name:

$$R_{\mu\nu} - \frac{1}{2}g_{\mu\nu}R = \frac{8\pi G}{c^4}T_{\mu\nu} \tag{2.1}$$

where $R_{\mu\nu}$ is the Ricci Tensor, R the Ricci Scalar[1], G the universal gravitational constant, c the speed of light, $g_{\mu\nu}(x)$ is the symmetric Metric Tensor and $T_{\mu\nu}$ is the Energy-Momentum tensor
The proportionality coefficient that relates Energy-Momentum to Spacetime Curvature is actually so small ($\frac{8\pi G}{c^4} \approx 2 \times 10^{-43}\,\mathrm{s^2 m^{-1} kg^{-1}}$) that the attention can be focused on studying the linearization of Einstein's Field Equation around the flat-space metric $\eta_{\mu\nu} = diag(-1, 1, 1, 1)$. The expansion of the Metric Tensor in the linearized theory is defined as:

$$g_{\mu\nu} = \eta_{\mu\nu} + h_{\mu\nu}; \qquad |h_{\mu\nu}| << 1 \tag{2.2}$$

---

[1]The Ricci Tensor and Scalar are defined in respect to the Riemann Tensor $R^\mu_{\nu\rho\sigma}$, which is in turn defined upon the Christoffel Symbol $\Gamma^\rho_{\mu\nu}$, a tensorial set of coefficients that refers directly to the Metric Tensor. The definition of these four quantities can be stated as follows:

$$\Gamma^\rho_{\mu\nu} = \frac{1}{2}g^{\rho\sigma}(\partial_\mu g_{\sigma\nu} + \partial_\nu g_{\sigma\mu} - \partial_\sigma g_{\mu\nu});$$

$$R^\mu_{\nu\rho\sigma} = \partial_\rho\Gamma^\mu_{\nu\sigma} - \partial_\sigma\Gamma^\mu_{\nu\rho} + \Gamma^\mu_{\alpha\rho}\Gamma^\alpha_{\nu\sigma} - \Gamma^\mu_{\alpha\sigma}\Gamma^\alpha_{\nu\rho};$$

$$R_{\mu\nu} = R^\alpha_{\mu\alpha\nu};$$

$$R = g^{\mu\nu}R_{\mu\nu}.$$

After choosing this almost Minkowskyian frame of reference one should proceed at linearizing all the quantites that are defined upon the Metric Tensor:

$$\Gamma^{\sigma}_{\mu\nu} = \frac{1}{2}(\partial_\mu h^{\sigma}_\nu + \partial_\nu h^{\sigma}_\mu - \partial^\sigma h_{\mu\nu}) \tag{2.3a}$$

$$R^{\sigma}_{\mu\nu\rho} = \frac{1}{2}(\partial_\nu\partial_\mu h^{\sigma}_\rho + \partial_\rho\partial^\sigma h_{\mu\nu} - \partial_\nu\partial_\sigma h^{\sigma}_\mu - \partial_\sigma\partial_\mu h^{\sigma}_\nu) \tag{2.3b}$$

$$R_{\mu\nu} = \frac{1}{2}(\partial_\nu\partial_\mu h + \Box h_{\mu\nu} - \partial_\nu\partial_\sigma h^{\sigma}_\mu - \partial_\sigma\partial_\mu h^{\sigma}_\nu) \tag{2.3c}$$

$$R = \Box h - \partial_\mu\partial_\sigma h^{\mu\sigma} \tag{2.3d}$$

where it was denoted $\Box = \partial_\sigma\partial^\sigma$ the D'Alembertian operator and $h = h^{\sigma}_\sigma$ the trace of the linear term of the Metric Tensor expansion. Then, defining the quantity:

$$\bar{h}_{\mu\nu} = h_{\mu\nu} - \frac{1}{2}\eta_{\mu\nu}h \tag{2.4}$$

a trivial algebraic substitution of Eqs.2.3 into Eq.2.1 leads to the linearized version of Einstein's Field Equations:

$$\Box\bar{h}_{\mu\nu} + \eta_{\mu\nu}\partial^\rho\partial^\sigma\bar{h}_{\rho\sigma} - \partial^\rho\partial_\nu\bar{h}_{\mu\rho} - \partial^\rho\partial_\mu\bar{h}_{\nu\rho} = \frac{16\pi G}{c^4}T_{\mu\nu}. \tag{2.5}$$

Having chosen a frame of reference where Eq.2.2 is valid, still leaves the freedom to perform a gauge transormation under which the equations will remain covariant. The wisest choice for the residual transformation is the Lorenz Gauge:

$$\partial^\nu\bar{h}_{\mu\nu} = 0 \tag{2.6}$$

which immediately simplify the linearized field equations to a tensorial wave equation:

$$\Box\bar{h}_{\mu\nu} = \frac{16\pi G}{c^4}T_{\mu\nu}. \tag{2.7}$$

In order to study the propagation of the wave-like perturbations that arise from this equation and their interaction with test masses, Eq.2.7 should be analyzed in vacuum, that is the condition that surround the source, where $T_{\mu\nu} = 0$:

$$\Box\bar{h}_{\mu\nu} = 0. \tag{2.8}$$

A solution to this type of equation can be found with the Green Functions Method, that yelds:

$$\bar{h}_{\mu\nu} = A_{\mu\nu}e^{ik_\rho z^\rho}. \tag{2.9}$$

By inserting this wave-like solution into Eq.2.6 and Eq.2.8, two constraints on the $\bar{h}_{\mu\nu}$ tensor are obtained:

$$A^{\mu\nu}k_\mu = 0 \tag{2.10a}$$

$$k_\sigma k^\sigma = 0 \tag{2.10b}$$

wich lower its degrees of freedom from 10 to 6. In particular the first condition implies that the $\bar{h}_{\mu\nu}$ tensor will be transverse in this specific gauge, the second one that the wave-like perturbation will travel at the speed of light.

Starting from the current frame of reference it can be performed a further transformation that simplify the form of the $\bar{h}_{\mu\nu}$ tensor, without spoiling the Lorenz Gauge[2]. Then the 4 components of the new

---

[2]It is trivial to show that a coordinate trasformation $x^\mu \to x^\mu + \zeta^\mu$ with $\Box\zeta_\mu = 0$, where ζ^μ is an infinitesimal quantity, is compatible with the Lorenz Gauge $\partial^\nu\bar{h}_{\mu\nu}$. This condition further implies $\Box\zeta_{\mu\nu} = 0$, where $\zeta_{\mu\nu} \equiv \partial_\mu\zeta_\nu + \partial_\nu\zeta_\mu - \eta_{\mu\nu}\partial_\sigma\zeta^\sigma$.

gauge transformation can be used to set 4 more constraints on $\bar{h}_{\mu\nu}$, reducing the number of its degrees of freedom from 6 to 2. This gauge freedom was used to find a solution that satisfies the equations:

$$\bar{h}_{TT}^{0i} = 0; \qquad\qquad \bar{h}_{TT} = 0. \tag{2.11}$$

The frame of reference in which this conditions are valid is named Transverse Traceless Gauge (TT). The last two remaining degrees of freedom of the gravitational wave solution in the TT Gauge can be manifestly shown for a plane wave propagating along the z axis $\vec{k} = (1, 0, 0, 1)$:

$$\bar{h}_{\mu\nu}^{TT} = \begin{pmatrix} 0 & 0 & 0 & 0 \\ 0 & h_+ & h_\times & 0 \\ 0 & h_\times & -h_+ & 0 \\ 0 & 0 & 0 & 0 \end{pmatrix} e^{i\omega(t-z/c)}. \tag{2.12}$$

The above equation is expressed in terms of the retarded time $t - z/c$ as the gravitational information is constrained to propagate at speed of light. The two Gravitational Wave Polarizations are named respectively Plus ($+$) and Cross ($\times$) Polarization. Then it can be immediately seen that, due to the passage of a Gravitational Wave, the invariant infinitesiaml space-time interval is periodically modulated:

$$\begin{aligned} ds^2 =& g_{\mu\nu} \, dx^\mu \, dx^\nu = \\ =& - c \, dt^2 + dz^2 + \{1 + h_+ \cos[\omega(t - z/c)]\} \, dx^2 \\ & + \{1 - h_+ \cos[\omega(t - z/c)]\} \, dy^2 + 2h_\times \cos[\omega(t - z/c)] \, dx \, dy \end{aligned} \tag{2.13}$$

As the ds^2 is invariant, that is it's independent of the refence frame choice, the above equation manifestly shows that the Gravitational Wave solution has 'physical' effects and it's not an artifact of the specific Gauge choices that has been made to obtain Eq.2.12.

2.2 Geodesics and Newtonian Forces

Despite the general result obtained in Eq.2.13, if one is intrested at analyzing the effects of a Gravitational Wave on an array of test masses, the system should be studied in a (Local) Free Falling Reference Frame[3], as this reference frame is ideally inertial with the test masses of the interferometer, which are isolated from external non-gravitational forces. Moreover the oscillating coordinates of the TT Gauge does not reflect the experimental situation in which scientists hope to detect a displacement of the free falling test masses respect to a rigid ruler, that is a measurment apparatus so small that the modification induced on it by the passage of a Gravitational wave can be neglected[4]. The Free Falling Reference Frame of the experimental test masses is often referred as the Proper Detector Frame.
The equation of motion for a point mass in a background described by the metric $g_{\mu\nu}$ in absence of external forces is described by the Geodesic Equation[5]:

$$\frac{d^2 x^\mu}{d^2\tau} + \Gamma_{\rho\sigma}^\mu(x)\frac{dx^\rho}{d\tau}\frac{dx^\sigma}{d\tau} = 0. \tag{2.14}$$

The above equation was parametrized in terms of the Proper Time τ, that is the time measured by a free falling clock following the given geodesic:

$$c^2 \, d\tau^2 = -ds^2 = -g_{\mu\nu} \, dx^\mu \, dx^\nu. \tag{2.15}$$

---

[3]In theory, a Local Free Falling Reference Frame is defined by requiring that, in the neighborhood of the origin, the Christoffel Symbols vanish: $\Gamma_{\nu\rho}^\mu(x) = 0$.

[4]More precisely, when taking a resonant bar as a ruler, it can be considered rigid respect to the passage of a GW of frequency ω if its resonance frequency $\omega_0 \gg \omega$.

[5]For a complete derivation of the Geodesic Equation, see for instance [14].

As the aim of the analysis is to compare the geodesics of different free falling masses, the first thing to do is to fix a free falling reference frame that is inertial with a specific particle. In this reference frame, that is usually called Fermi Local Coordinate System, the metric is flat at first order even in the presence of Gravitational Waves:

$$ds^2 \approx c^2 \, dt^2 - \delta_{ij} \, dx^i \, dx^j. \tag{2.16}$$

Then, expanding the metric at second order around the origin of the free falling frame and expressing the second derivatives of $g_{\mu\nu}$ in terms of the Riemann Tensor, the following result is obtained[6]:

$$
\begin{aligned}
ds^2 \approx - \, & c^2 \, dt^2[1 + R_{0i0j}x^i x^j] \\
& - 2c \, dt \, dx^i \Big(\frac{2}{3} R_{0ijk} x^j x^k \Big) + dx^i \, dx^j \Big[\delta_{ij} - \frac{1}{3} R_{ikjl} x^k x^l \Big].
\end{aligned}
\tag{2.17}
$$

Then we can consider two nearby geodesics each parametrized by its own proper time, the coordinate distance that separates the two free falling particles on the geodesics is the space-time vector $\mathcal{E}^\mu(\tau)$ that connect points with the same value of τ on the two geodesics. The Geodesic Equation 2.14 will be valid along the first geodesic $x^\mu(\tau)$, while on the second goedesic $x^\mu(\tau) + \mathcal{E}^\mu(\tau)$ it will take the form:

$$\frac{d^2(x^\mu + \mathcal{E}^\mu)}{d^2\tau} + \Gamma^\mu_{\rho\sigma}(x + \mathcal{E}) \frac{d(x^\rho + \mathcal{E}^\rho)}{d\tau} \frac{d(x^\sigma + \mathcal{E}^\sigma)}{d\tau} = 0. \tag{2.18}$$

Assuming $|\mathcal{E}(\tau)|$ is much smaller than the typical scale of variation of the gravitational field, its evolution can be studied by taking the first order difference between Eq.2.14 and Eq.2.18, obtaining the Geodesic Deviation Equation:

$$\frac{d^2\mathcal{E}^\mu}{d^2\tau} + 2\Gamma^\mu_{\rho\sigma}(x) \frac{dx^\rho}{d\tau} \frac{d\mathcal{E}^\sigma}{d\tau} + \mathcal{E}^\nu \partial_\nu \Gamma^\mu_{\rho\sigma}(x) \frac{dx^\rho}{d\tau} \frac{dx^\sigma}{d\tau} = 0. \tag{2.19}$$

Near the Proper Detector Frame (PDF) origin $\Gamma^\mu_{\rho\sigma}(x)$ vanishes and $dx^i/d\tau$ can be neglected respect to $dx^0/d\tau$ as the detector is moving non-relativistically:

$$\frac{d^2\mathcal{E}^i}{d^2\tau} + \mathcal{E}^\sigma \partial_\sigma \Gamma^i_{00}(x) \Big(\frac{dx^0}{d\tau} \Big)^2 = 0. \tag{2.20}$$

The Geodesic Deviation Equation in the Proper Detector Frame can be further rewritten by noting that near the origin only the both-spatial double derivatives of the metric are non vanishing, thus $\mathcal{E}^\sigma \partial_\sigma \Gamma^i_{00} = \mathcal{E}^j \partial_j \Gamma^i_{00}$. Moreover, in the PDF we have by definition $\partial_0 \Gamma^i_{0j} = 0$, then it is also valid $R^i_{0j0} = \partial_j \Gamma^i_{00} - \partial_0 \Gamma^i_{0j} = \partial_j \Gamma^i_{00}$. Therefore Eq.2.20 becomes[7]:

$$\frac{d^2\mathcal{E}^i}{d^2\tau} = -R^i_{0j0} \mathcal{E}^j \Big(\frac{dx^0}{d\tau} \Big)^2. \qquad \Rightarrow \qquad \ddot{\mathcal{E}}^i = -c^2 R^i_{0j0} \mathcal{E}^j. \tag{2.21}$$

In order to compute R^i_{0j0}, one can take advantage of the fact that in the linearized theory the Riemann Tensor is invariant rather than covariant, so that it can be equivalently computed in TT Gauge, where its derivation is easier due to the simpler form of Gravitational Waves in this reference frame. From the Riemann Tensor definition it follows immediately $R^i_{0j0} = R_{i0j0} = -\frac{1}{2c^2} \ddot{h}^{TT}_{ij}$, and the Geodesic Deviation Equation in the Proper Detector Frame eventually becomes:

$$\ddot{\mathcal{E}}^i = \frac{1}{2} \ddot{h}^{TT}_{ij} \mathcal{E}^j. \tag{2.22}$$

---

[6]For an Earthbound detector one should also account for the fact that the laboratory frame is accelerated and rotating. This would yeld various additional terms to the ds^2 expression (Centrifugal acceleration, Coriolis Effect, ecc.). This terms actually have much bigger amplitudes respect to the Riemann Tensor terms that are explicited in Eq.2.17 at low frequencies, but at sufficiently high frequencies this contributions are highly suppressed and we can neglect them.

[7]At first order in h we have $t = \tau$ and $dx^0/d\tau = c$. We also denote with $\dot{\mathcal{E}}$ the derivative with respect to the coordinate time t of the Proper Detector Frame.

The physical meaning of this simple equation is that, in the Proper Detector Frame, the effect of a Gravitational Wave on an array of point particles can be described in terms of a Newtonian Force. It's important to underline that in the Proper Detector Frame at first order coordinate distances $\mathcal{E}^i$ are equal to proper distances s^i. Then, upon verification that the first order approximation is satisfied in the experimental set-up, the result 2.22 has general validity and it describes the physical response of the system to a GW passage in every possible non-relativistic frame, included the TT Gauge.

2.3 GW's Effect on an Array of Test Masses

As an example it can be studied the effect of a Gravitational Wave propagating along the z-axis on a ring of test masses laying on the xy-plane[8]. The two GW polarizations can be studied separately. Starting from the Plus polarization ($h_\times = 0$) and remembering the $\bar{h}_{ab}^{TT}$ expression from Eq.2.12, the proper distance variation between the ring particles and the origin of the plane can be studied upon defining $\mathcal{E}_a(t) = (x_0 + \delta x(t), y_0 + \delta y(t))$. Then Eq.2.22 becomes:

$$
\begin{aligned}
\ddot{\mathcal{E}}_a^1 = \delta\ddot{x} &= -\frac{h_+}{2}(x_0 + \delta x)\omega^2 \sin(\omega t) \\
\ddot{\mathcal{E}}_a^2 = \delta\ddot{y} &= +\frac{h_+}{2}(y_0 + \delta y)\omega^2 \sin(\omega t).
\end{aligned}
\tag{2.23}
$$

The δx and δy terms on the right side of the above equations can be neglected to the first order in h as they have dimension $O(h_+)$, so that the differential equation can be directly integrated:

$$
\begin{aligned}
\delta x(t) &= +\frac{h_+}{2}x_0 \sin(\omega t) \\
\delta y(t) &= -\frac{h_+}{2}y_0 \sin(\omega t).
\end{aligned}
\tag{2.24}
$$

Proceeding analogously for the Cross polarization case ($h_+ = 0$), the resulting evolution of the test mass displacement is:

$$
\begin{aligned}
\delta x(t) &= +\frac{h_\times}{2}y_0 \sin(\omega t) \\
\delta y(t) &= +\frac{h_\times}{2}x_0 \sin(\omega t).
\end{aligned}
\tag{2.25}
$$

The periodical modulation effect of each GW poarization on a ring of test masses is shown in Fig.2.1. In the general case where both polarizations are present the resulting effect is a superposition of the two single-polarization modulations. It's important to note few aspects of the results obtained in Eq.2.24 and Eq.2.25. The test mass displacements are proportional to the distance between the particle and the origin of the frame of reference. This means that the effect of GW passage is a constant relative deformation of the detector along the perpendicular direction to the the wave-vector:

$$
\frac{\delta l}{l} = \pm\frac{h_{+/\times}}{2}\sin(\omega t).
\tag{2.26}
$$

It can be seen that the only free parameters that govern the relative detector deformation are the polarization amplitude $h_{+/x}$ and the GW frequency ω. The parameters are dictated both by the source properties and its distance and orientation respect to the detector. Then, if one is intrested in studying

---

[8]As GWs are transverse waves, there are no effects of their passage manifesting along the parallel direction to the wave vector. Then we can fix the test mass array on the perpendicular plane to the direction of propagation and their effect will be maximized.
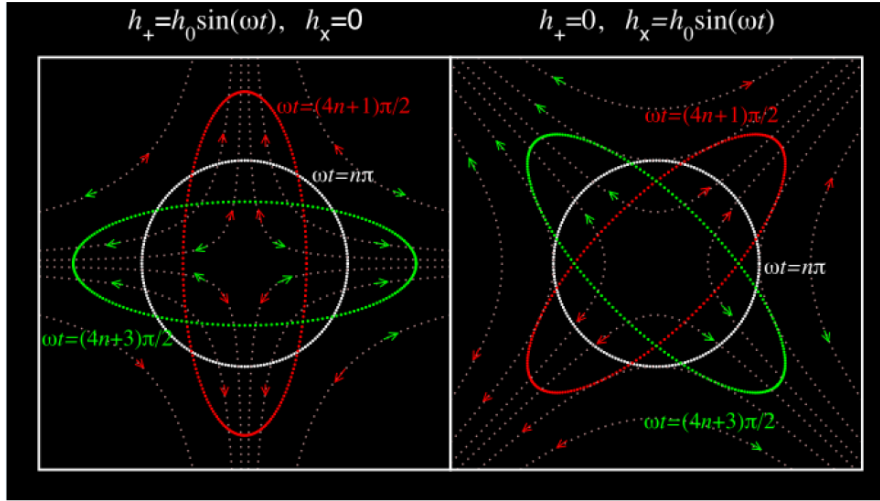
Figure 2.1: Effects of Plus (left) and Cross (right) polarization on a ring of test masses (white). The tidal field of the waves on the ring is indicated by light dotted lines. The direction of the force reverses sign each half-period of the wave as indicated by the red and green arrows.

the feasibility of Gravitational Wave detection it is necessary to estimate the magnitude of this quantities at source and after propagation. Nowadays, in order to extract the waveform and sky location parameters from the interferometer mirror displacement, the acquired signal is compared with a detailed catalogue of waveform templates obtained via Numerical Relativity to find the set of parameters that best match the observation. Nevertheless it is still possible to gain an useful insight on Gravitational Wave generation and propagation by trying to solve analitically GR's linearized field equations under certain approximations and simmetry assumptions. In particular, for a system of two point-like masses in circular orbit around the center of mass of the system with non-relativistic velocities, expanding to the leading quadrupole radiation term at large distances from the source, the following result for the Gravitational Wave Amplitude can be obtained[9]:

$$h \approx \frac{1}{r} \frac{G \, \mu \, \omega_S^2 \, R^2}{c^4} \tag{2.27}$$

where $\mu = m_1 m_2/(m_1 + m_2)$ is the reduced mass of the system, ω_S is the orbital frequency and R the orbital radius. The most important aspect of this equation is the $1/r$ GW Strain dependence upon propagation, that is analogous to multipole radiation instead of an usual spherical wave, which amplitude decreases as $1/r^2$. This desirable amplitude proportionality has a remarkable consequence for the detector upgrade design; in fact, an order 10 improvement in the detector sensibility translates in a 10^3 increase of the space-time volume that could be explored with the instrument. Then, as the LIGO and VIRGO detectors are close to achieving their maximal design sensitivity, it is advantageous to start researching and designing a new generation of Earthbound interferometrical detectors that will be capable of exceeding at least of an order of magnitude the sensitivity of the current detectors.

---

[9]See [13] for a detailed derivation.

Chapter 3

The Interferometric Method for GW Detection

3.1 Michelson Interferometers

The basic concept at the core of the modern antennae that succeded in the first gravitational wave detections in the last few years is the simple one of the Michelson Interferometer. A Michelson Interferometer is, in its simplest configuration, an array of two mirrors and one beam splitter together with a monocromatic light source that allows to sense a variation in the differential length between the two interferometer arms exploiting the phenomenon of interference of Electro-Magnetical Waves. The operating principle of a Michelson interferometer and its interactions with a Gravitational Wave are summarized in the following section.
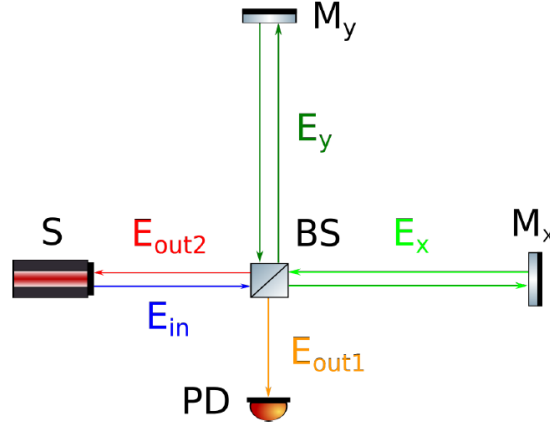

Figure 3.1: Basic Michelson interferometer scheme. Monocromatic Source (S), Beam Splitter (BS), Mirrors (M_x, M_y), Photodiode (PD).

The scheme of a basic Michelson Interferometer configuration can be seen in Fig.3.1. The monochromatic light source is nowadays always provided by a laser device. The beam is splitted in two orthogonal arms and after having travelled twice along each arm it recombines at the beam splitter, partly heading toward the output port and partly directed back to the input source.

The input beam can be represented with the complex notation for electromagnetical fields:

$$E_{in} = E_0 e^{-i(\omega_l t - \vec{k}_l \cdot \vec{x})} \tag{3.1}$$

where ω_l is the laser frequency and $\vec{k}_l$ the laser beam wave vector ($|\vec{k}_l| = 2\pi/\lambda_l = \omega_l/c$). After being divided and recombined, the output beam amplitude can be obtained by the superposition of the two

x/y-arm beams, properly accounting for the $\phi_{x/y}$ phase picked up upon reflection:

$$E_x = \frac{E_0}{\sqrt{2}} e^{i(k_l L_x - \omega_l t + \phi_x)}, \qquad\qquad E_y = \frac{E_0}{\sqrt{2}} e^{i(k_l L_y - \omega_l t + \phi_y)} \qquad (3.2)$$

where the factor 2 at denominator is due to the double transmission through the beam splitter. Then the output intensity is immediately obtained from the output amplitude expression:

$$I_{Out} = |E_{Out}|^2 = |E_x + E_y|^2 = \frac{E_0^2}{2}\Big(1 + \cos\big(k(L_x - L_y) + (\phi_x - \phi_y)\big)\Big). \qquad (3.3)$$

The electromagnetical wave acquires a $\phi = \pi$ extra-phase at each reflection. Then the acquired phases for the two input and output directed recombined beams can be explicitly computed: the output directed beam ($Out1$) acquires a total phase $\phi_1 = \phi_x - \phi_y = (\pi + \pi) - (\pi + \pi) = 0$; the input directed beam ($Out2$) acquires a total phase $\phi_2 = \phi_x - \phi_y = \pi - (\pi + \pi + \pi) = -2\pi$. Then the intensities of the two recombining beams become:

$$
\begin{aligned}
I_{Out1} &= \frac{E_0^2}{2}\Big(1 - \cos\big(k(L_x - L_y)\big)\Big) = E_0^2 \sin^2\Big(\frac{k}{2}(L_x - L_y)\Big); \\
I_{Out2} &= \frac{E_0^2}{2}\Big(1 + \cos\big(k(L_x - L_y)\big)\Big) = E_0^2 \sin^2\Big(\frac{k}{2}(L_x - L_y) + \pi\Big).
\end{aligned}
\qquad (3.4)
$$

Therefore a variation in the differential length of the two interferometer arms results in a power variation at the output port that could be properly detected with a photodiode, while the remaining power is sent back to the input port, consistently with energy conservation principle.

If one then desires to analyze the response of a Michelson Interferometer to a Gravitational Wave passage, the TT Gauge is the most convenient frame in which conducting the analysis, as the coordinate of the free falling interferometrical test masses are fixed by definition in this reference frame. Instead it is the light beam propagation time across the interferometer arms that is affected from the Gravitational Wave passage in TT Gauge.
Assuming for simplicity that the Gravitational Wave is composed only of Plus polarization ($h_\times = 0$) and that it is traveling along the z direction, for an interferometer laying in the $z = 0$ plane the metric gravitational wave amplitude becomes:

$$h_+(t) = h_0 \cos(\omega_{gw} t) \qquad (3.5)$$

where ω_{gw} is the frequency of the incoming Gravitational Wave. Then, for a photon travelling along a null geodesic, the invariant space-time interval results:

$$ds^2 = -c^2\, dt^2 + \big(1 + h_+(t)\big)dx^2 + \big(1 - h_+(t)\big)dy^2 + dz^2 = 0. \qquad (3.6)$$

The above equation can be projected to a single coordinate to calculate the total photon travel time along each arm. Starting from the x arm, at first order in h_0:

$$dx = \pm\sqrt{\frac{c^2\, dt^2}{1 + h_+(t)}} \approx \pm c\, dt\Big(1 - \frac{1}{2}h_+(t)\Big) \qquad (3.7)$$

where the $+$ sign distinguish the back and forth trips. Starting from the beam splitter at instant t_0, the time t_1 at which the photon reaches the x arm mirror is obtained by integrating Eq.3.7 with the plus sign the two endpoints $x = 0$ and $x = L_x$:

$$\int_0^{L_x} dx = +c \int_{t_0}^{t_1} dt\Big(1 - \frac{1}{2}h_+(t)\Big) \qquad \Rightarrow \qquad L_x = c(t_1 - t_0) - \frac{c}{2}\int_{t_0}^{t_1} dt\, h_+(t). \qquad (3.8)$$

An analogous integration with the minus sign for the return trip from the mirror $x = L_x$ to the beam splitter $x = 0$, gives:

$$\int_{L_x}^{0} dx = -c \int_{t_1}^{t_2} dt \left(1 - \frac{1}{2} h_+(t)\right) \quad \Rightarrow \quad L_x = c(t_2 - t_1) - \frac{c}{2} \int_{t_1}^{t_2} dt h_+(t). \tag{3.9}$$

The sum of Eq.3.8 and Eq.3.9 gives the total travel time for the photon that is moving along the x arm:

$$t_2 - t_0 = \frac{2L_x}{c} + \frac{1}{2} \int_{t_0}^{t_2} dt h_+(t). \tag{3.10}$$

As the integrand in Eq.3.10 is already of order $O(h_0)$, the upper limit of the integral can be approximated with the flat metric roundtrip time $t_2 = t_0 + 2L_x/c$. Exploiting the trigonometric expression $\sin(\alpha + 2\beta) - \sin(\alpha) = 2\sin(\beta)\cos(\alpha + \beta)$, the following expression is obtained:

$$\begin{aligned} t_2 - t_0 &= \frac{2L_x}{c} + \frac{1}{2} \int_{t_0}^{t_0 + 2L_x/c} dt h_0 \cos(\omega_{gw} t) = \\ &= \frac{2L_x}{c} + \frac{h_0 L_x}{c} \frac{\sin(\omega_{gw} L_x/c)}{\omega_{gw} L_x/c} \cos\left(\omega_{gw}(t_0 + L_x/c)\right) = \\ &= \frac{2L_x}{c} + \frac{L_x}{c} h_+\left(t_0 + \frac{L_x}{c}\right) \frac{\sin(\omega_{gw} L_x/c)}{\omega_{gw} L_x/c} \end{aligned} \tag{3.11}$$

where, in the last identity, Eq.3.5 was used to simplify the expression. The above equation shows that the flat-metric photon roundtrip travel time along an arm ($2L_x/c$) is modified by the passage of a Gravitational Wave with a term that is proportional to the value of the GW amplitude at the instant when the photon reaches the arm mirror ($t_0 + L_x/c$) and to the arm length L_x. Moreover, the roundtrip travel time modification is proportional to the function:

$$\text{sinc}\left(\frac{\omega_{gw} L_x}{c}\right) \equiv \frac{\sin(\omega_{gw} L_x/c)}{\omega_{gw} L_x/c} \tag{3.12}$$

the behaviour of which is shown in Fig.3.2. The sinc function approaches 1 for $\omega_{gw} L_x/c \ll 1$ and the travel time modification simplifies to $h_+(t_1) L_x/c$, while it get suppressed for $\omega_{gw} L_x/c \gg 1$. This behaviour has a simple physical interpretation: if the detector arm is made too long, then $\omega_{gw} L_x/c \gg 1$ and the GW metric perturbation changes sign many times along the roundtrip, so that its overall effect gets averaged out; on the contrary, if the interferometer arm is made too short, then it is the L_x factor that inhibits the dector sensibility to detect variations in the metric, as there is not enough time for the photon that is travelling along the arm to integrate the Gravitational Wave effect. Then the interferometer lenght must be ideally optimized to maximize the signal in the possible frequency range of the target source.

An analogous computation can be performed for the y-arm case. Comparing the roundtrip travel time in the two orthogonal arms the total phase difference introduced by a Gravitational Wave in the Michelson interferometer output beam is obtained:

$$\Delta\phi_{Mich} \approx \omega_l \left(2\frac{L_x - L_y}{c} + \frac{2L}{c} h_0 \cos(\omega_{gw} t + \alpha) \, \text{sinc}\left(\frac{\omega_{gw} L}{c}\right)\right) = \Delta\phi_0 + \Delta\phi_{gw} \tag{3.13}$$

where the first order in h_0 approximation $L_x \approx L_y \approx L$ was performed, as the usual experimental configuration for a Michelson Interferometer is nearly symmetrical[1]. Substituting back this result

---

[1]More specifically, the $\Delta\phi_0$ term contains two contributions that are properly tuned by experimentalist to build the optimal conditions for GW detection in the interferometer. In particular, the first one is a microscopical asymmetry term to control the interferometer working point, that is the intensity of the recombined beam directed to the output port that, for various reasons, it is not null; the second one is a macroscopic term, named Schnupp Asymmetry, that is needed for allowing the GW frequency sidebands (see Eq.3.16) to leak out at the output port.
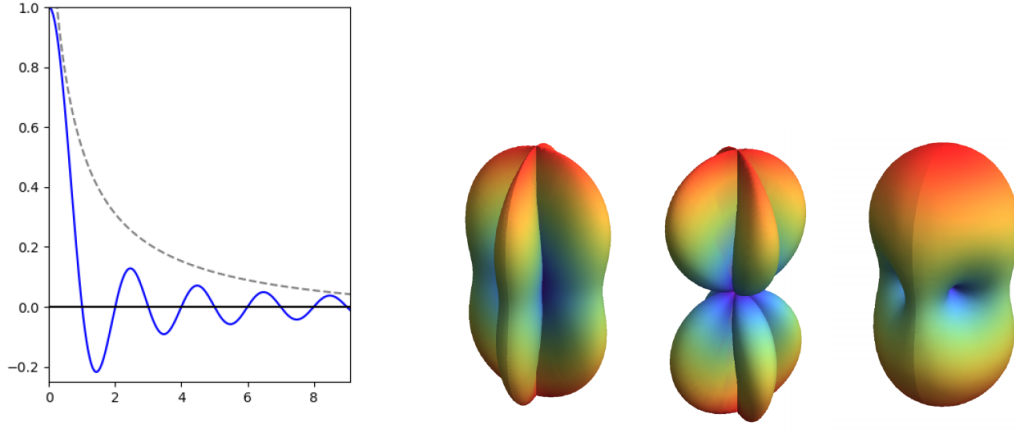
Figure 3.2: Left: Sinc function (blue) compared to $1/x$ (dashed) in the positive domain. Right: (From left to right) Antenna Pattern of a Michelson Interferometer in the $+$, $\times$, and generic polarization cases [15].

in Eq.3.4, it is shown how the intensity of the recombined beam in a Michelson Interferometer is modulated by the passage of a Gravitational Wave:

$$I_{Out} = E_0^2 \sin^2(\Delta\phi_0 + \Delta\phi_{gw}). \tag{3.14}$$

Specifically, the ideal interferometer arm length for detecting a Gravitational Wave of given frequency can be explicitly computed by maximising the GW induced phase in the recombined beam $\Delta\phi_{gw}$, giving the following result result ($f_{gw} = \omega_{gw}/2\pi$):

$$L \approx 750\,\mathrm{km}\Big(\frac{100\,\mathrm{Hz}}{f_{gw}}\Big) \tag{3.15}$$

It can also be noted that, extending the computation to a generic arm and analyzing the result with the complex field notation, the following expression at first order in h_0 for the amplitude of the recombined beam that is directed toward the output port is obtained:

$$
\begin{aligned}
E_{Out1} &= \frac{E_0}{2} e^{-i\omega_l\left(t-\frac{2L}{c}\right)} e^{+i\omega_l\frac{L}{c}h_+\left(t-\frac{L}{c}\right)} \operatorname{sinc}\left(\frac{\omega_{gw}L}{c}\right) \approx \\
&\approx \frac{E_0}{2} e^{-i\omega_l\left(t-\frac{2L}{c}\right)} \left(1 + i\omega_l\frac{L}{c}\operatorname{sinc}\left(\frac{\omega_{gw}L}{c}\right)\frac{e^{i(\omega_{gw}t+\alpha)} + e^{-i(\omega_{gw}t+\alpha)}}{2}\right) = \\
&= \frac{E_0}{2} e^{2i\alpha}\left(e^{-i\omega_l t} + \beta e^{-i\alpha}e^{-i(\omega_l-\omega_{gw})t} + \beta e^{-i\alpha}e^{-i(\omega_l+\omega_{gw})t}\right)
\end{aligned} \tag{3.16}
$$

where $\alpha = -\omega_{gw}L/c$ is the generic flat-metric halftrip phase and β which contains the gravitational wave amplitude. Then, Eq.3.16 shows that the passage of a Gravitational Wave has the effect of generating two symmetrical frequency sidebands in the output beam that are spaced by a frequency ω_{gw} from the carrier laser frequency ω_l.

By instead considering the general case of a Gravitational Wave that is generated by a source located at a θ zenith angle and ϕ azimuthal angle respect to the detector plane:

$$h(t) = \frac{1}{2}\big(1 + \cos^2(\theta)\big)\cos(2\phi)h_+(t) + \cos(\theta)\sin(2\phi)h_\times(t), \tag{3.17}$$

the complete antenna pattern of a Michelson Interferometer is obtained. An illustration of the antenna pattern of a Michelson Interferometer in the case of a $+$-polarized and $\times$-polarized Gravitational Wave, along with a generically polarized GW, is shown in Fig.3.2, where color indicates increasing sensitivity from indigo to red.

3.2 Real Gravitational Wave Interferometers

In Sec.3.1 it was carried out a discussion on the effect of a Gravitational Wave on a basic Michelson Interferometer and in Eq.3.15 the optimal arm length for detecting a Gravitational Wave of given frequency has been computed. A plot representing the frequency ranges in wich various GW source types are expected to be emitting and the correspondent ranges in wich various detecting methods peak their sensitivity[2] is shown in Fig.3.3. The current generation of ground-based interferometers are sensible to Gravitational Waves in the acoustic band, generated by Black Holes Binaries, Neutron Star Binaries Mergers and by Stellar Supernovae.
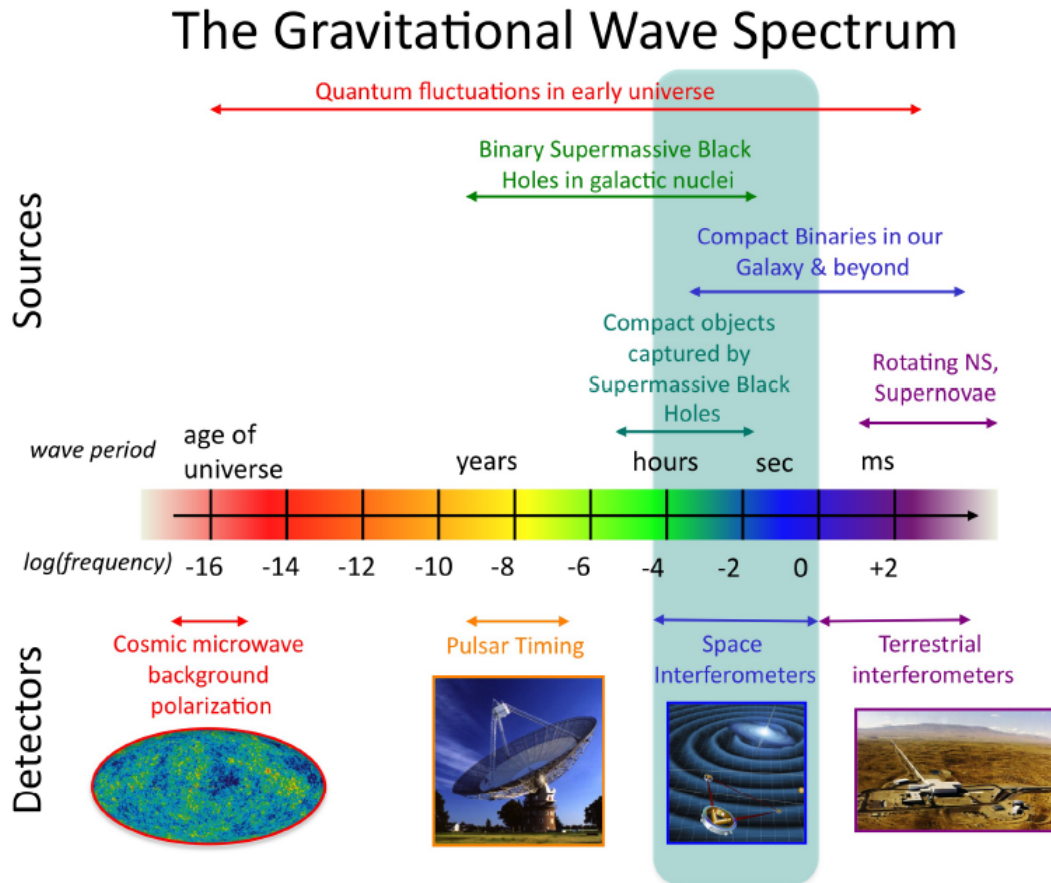

Figure 3.3: Expected Gravitational Wave Spectrum of main sources and detection methods [16].

The required arm length to optimize the detection of $[10 - 100]\,\mathrm{Hz}$ Gravitational Waves obtained from Eq.3.15 is $L \approx 10^3\,\mathrm{km}$. This is in apparent contradiction with the fact presented in Sec.1 that the LIGO and VIRGO interferometers have an arm length of $4\,\mathrm{km}$ and $3\,\mathrm{km}$ respectively. In fact the current generation of interferometers has already approached the limit length for a ground-based interferometer and even with the technological advancements that will be implemented in the next

---

[2]The only method that, at the time of writing, has been succesful in detecting Gravitational Waves is the one of ground-based Interferometers. The LISA mission is a (proposed) 2.5 million km arm triangular space interferometer that aims at detecting GW emitted in the processes related to Supermassive Black Holes in the sub-Hz band and its launch is planned for 2034 [17]. In order to detect sub-μHz GWs associated with Supermassive Black Holes it is instead proposed the Pulsar timing method, that attemps to detect anomalies in the extremely stable pulsar spinning periods as a consequence of the passage of a GW between Earth and the neutron star [18]. GWs are expected to be produced also by Quantum Fluctuations during the Cosmic Inflation period and their effect should be detectable analyzing the polarization of the Cosmic Microwave Background radiation [19].

generation of Earth-bound detectors, the arm lengths of the instrument will not exceed the $10\,km$ order of magnitude.

The conflict is resolved if one analyzes a realistic model for a ground-based GW interferometer, that makes use of several optical cavities to effectively increase the storage time of a photon inside the arms, while the initial estimate presented in Sec.3.1 refers to the simple Michelson Interferometer case.

An optical cavity is an arrangment of mirrors that allows for a closed path for a light beam. The photon is trapped between two or more mirrors for a certain amount of time of reflections (on average) before being eventually transmitted through one of the mirrors, thus increasing the beam optical path inside the interferometer arm.

As said, several types of cavities are implemented in a single ground-based interferometer, each one of which has its own peculiarities and specific aims. The most important cavities that are present in the current generation of GW interferometers are Fabry-Perot Cavities, that fold the beam path multiple times inside the interferometer arms, the Power Recycling Cavity, that reconveys the light that is leaking toward the input port back into the interferometer arms, the Input and Output Mode Cleaner Cavities, that exploit the narrow bandpass filtering property of resonant cavities to reject the unwanted normal modes that are present in the beam, and the Signal Extraction Cavity, that is tuned to enhance GW sidebands to improve the instrument sensitivity in a desired frequency range. A scheme showing the arrangement of the various cavities inside a GW interferometer can be seen in Fig.3.4.
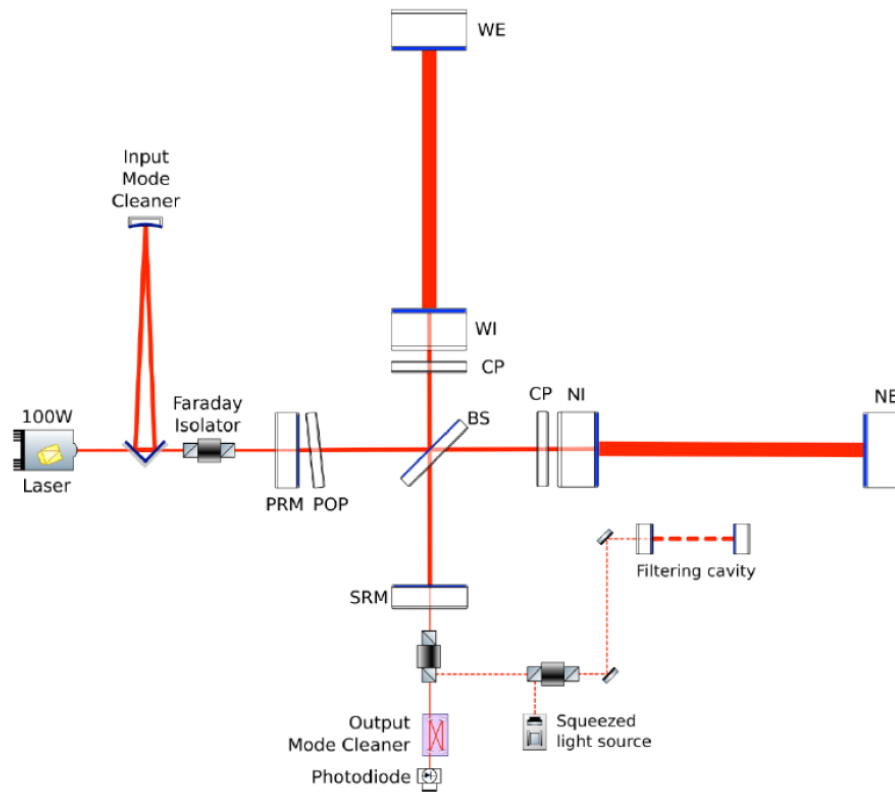

Figure 3.4: Advanced VIRGO optical configuration. BS: beam splitter; NI,WI: input test masses; NE,WE: end test masses; SRM: signal reciclying mirror. PRM: power reciclying mirror; POP: pick-off plate; CP: compensation plate.

A complete discussion of optical cavities requires the modelization of a laser beam with the paraxial approximation, that allows to decompose it in a superposition of ortho-normal modes, and performing computations of the cavity electrical field using the Circulating Field Approach [22], and it is not the scope of this work to present it in detail. As a general result it could be noted here that the effective increase of the optical path length thanks to the implementation of an optical cavity is quantified by

the average number of reflections to which the photon is subject before being transmitted out of the cavity N. The average number of reflections is in turn proportional to the cavity Finesse $\mathcal{F}$, defined by the following equation:

$$\mathcal{F} \equiv \frac{\pi\sqrt{r_1 r_2}}{1 - r_1 r_2} \qquad (3.18)$$

where r_1 and r_2 are the reflection coefficients of the two mirrors of a Fabry-Perot cavity. The two quantities are related by the proportionality $N \sim 2\mathcal{F}/\pi$, so that for a Michelson interferometer with Fabry-Perot cavities there is an increase in the phase shift induced by the passage of a Gravitational Wave:

$$\Delta\phi_{FP} \approx \frac{2\mathcal{F}}{\pi}\Delta\phi_{Mich} \approx \frac{4\mathcal{F}}{\pi}h_0 k_l L. \qquad (3.19)$$

Anyway the choice of the Fabry-Perot cavities Finesse in a GW interferometer is not solely dictated by detection frequency optimization based on source predicted properties but several other technical aspects must be considered in the design.

When developing in full detail the computations of the interaction between the cavities and the Gravitational Wave, the transfer function of a Fabry-Perot Interferometer is obtained [13]:

$$T_{FP}(f_{gw}) = \frac{8\mathcal{F}L}{\lambda_l}\frac{1}{\sqrt{1 + (f_{gw}/f_p)^2}} \qquad (3.20)$$

where $f_p \equiv \frac{1}{4\pi\tau_s}$ is the Cavity Pole Frequency with $\tau_s = \frac{2L}{c}\frac{1}{1-r_1^2}$ is the Cavity Storage Time.

3.3   Limits to the sensitivity of gravitational wave detectors

Since the deformation induced by a gravitational wave on an interferometer is very small, in the inter-
ferometric detection it is of vital importance to minimize all the noises that can pollute the signal to
analyze. Some are due to the environment (seismic noise, gusts of wind, temperature of the mirrors),
others to the design of the interferometer and others are related to fundamental physics. Each noise
source is peaked in a specific frequency range. The sum of all the input-refered noise contribution pro-
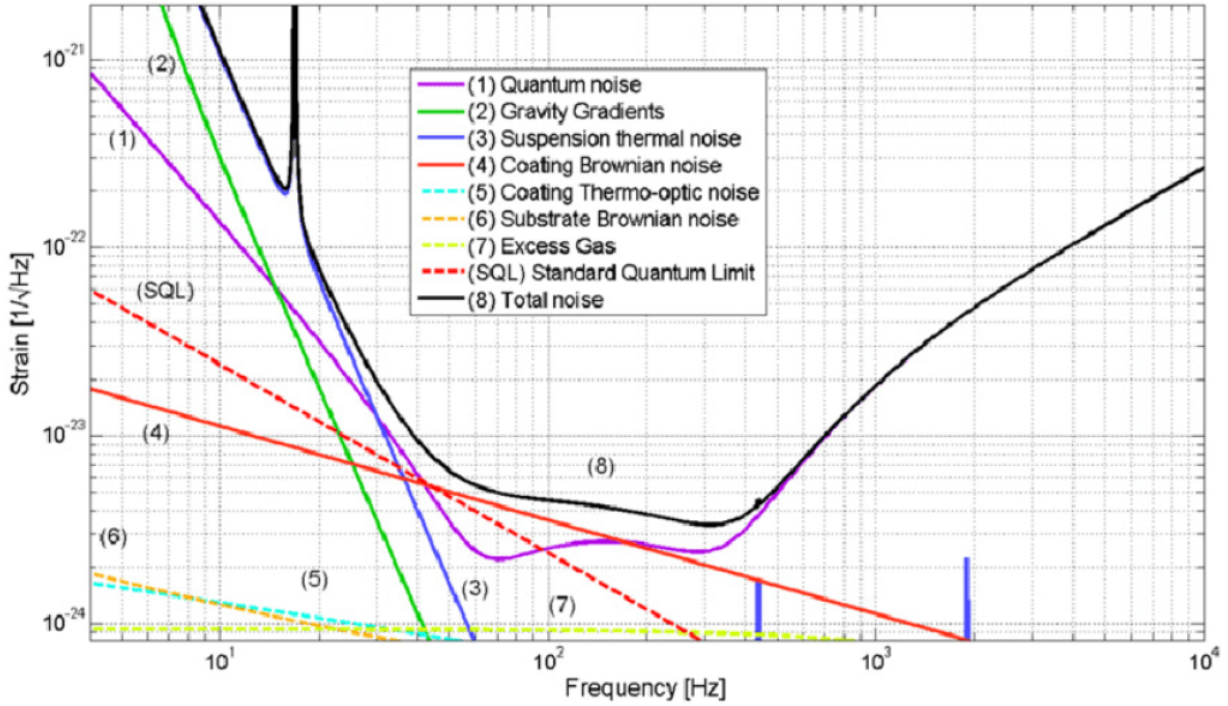vide the complete Noise Power Spectrum of the detector (Fig.3.5).

Figure 3.5: Design Sensitivity of the AdV detector [21].

3.3.1   Quantum Noise

The limit to the sensitivity of the interferometer deriving from the quantum nature of light is manifested
through two mechanisms: photon quantization noise and quantum radiation pressure noise. Both are
attributable to the quantum fluctuations of the vacuum electromagnetic field that enter the interferom-
eter from the so-called dark port of the beam splitter, the point at which destructive interference from
recombined beams is observed.

3.3.2   Shot noise

Laser light is composed of discrete quanta, photons, that indipentently interact with the readout pho-
todetector after having travelled in the interferometer. The photodetector acts as an integrator of the
energy $E = \hbar \omega_l / c$ that each photon deposit on it in a certain time period T, so that the average output
power measured at the photodetector is:

$$P_0 = \frac{N_\gamma \hbar \omega_l}{T} \tag{3.21}$$

where N_γ is the number of photons that interacted with the photodetector in the time interval T. The probability distribution of the process of counting discrete indepedent events, such as photon arrivals at the output port, is known to be the Poisson Distribution:

$$p(N_\gamma, \bar{N}_\gamma) = \frac{1}{N_\gamma!} \bar{N}_\gamma{}^{N_\gamma} e^{-\bar{N}_\gamma} \tag{3.22}$$

where $\bar{N}_\gamma$ is the average number of photons that are expected to reach the photodiode during T. For large $\bar{N}_\gamma$ the Poisson Distribution becomes a Gaussian Distribution with $\sigma = \sqrt{\bar{N}_\gamma}$. Therefore the photon arrival process in a given time interval has a fluctuation $\Delta N_\gamma = \sqrt{N_\gamma}$ that eventually translates in a power fluctuation at the photodiode:

$$(\Delta P)_{shot} = \frac{N_\gamma^{1/2} \hbar \omega_l}{T} = \left(\frac{\hbar \omega_l}{T} P_0 \right)^{1/2}. \tag{3.23}$$

What was found in the above equation is just the standard deviation of output power fluctuations $(\Delta P)_{shot} = \sigma_{P, shot}$, wich can be expressed by definition with the integral of the Spectral Density of power fluctuations over all the frequency domain delimited by the time interval T:

$$(\Delta P)_{shot} = \sigma_{P, shot} = \int_0^{\frac{1}{T}} d\omega \, S_{P, shot}(\omega). \tag{3.24}$$

Putting together Eq.3.23 and Eq.3.24 the Spectral Density of Output Power Fluctuation caused by Shot Noise $S_{P, shot}(\omega) = P_0 \hbar \omega_l$ is obtained, so that, as the detector output is proportional to P_0, the Relative Output Noise due to Shot Noise becomes:

$$S_{\Delta\phi, shot}^{1/2}(\omega) = \frac{S_{P, shot}(\omega)}{P_0} = \sqrt{\frac{\hbar \omega_l}{P_0}}. \tag{3.25}$$

In order to compare this output noise with the Strain h of a Gravitational Wave of frequency f_{gw} that is interacting with the interferometer, it is necessary to refer it to the detector input. That is, the Spectral Density of the Output Noise $S_{\Delta\phi, shot}^{1/2}(\omega)$ must be multiplied by the inverse of the transfer function of a Fabry-Perot Interferometer T_{FP} that was obtained in Eq.3.20. By accounting also for the fact that in a real GW interferometer Power Recycling Cavities are implemented to increase the circulating power inside Fabry-Perot Cavities and the not ideal efficiency of the photodiode, the interferometrical Strain Sensitivity due to Shot Noise can be expressed as:

$$S_{h, shot}^{1/2}(f) = \frac{S_{\Delta\phi, shot}^{1/2}(f)}{T_{FP}(f)} = \frac{1}{8 \mathscr{F} L} \sqrt{\frac{4\pi \hbar \lambda_l c}{\eta P_{bs}}} \sqrt{1 + \left(\frac{f}{f_p} \right)^2} \tag{3.26}$$

where $P_{bs} \equiv C P_0$ accounts for the power enahancement at the beam splitter due to the Power Recycling Cavity ($C = O(50 - 100)$) and η is the photodiode efficiency ($\eta \approx 0.9 - 0.95$).

3.3.3 Radiation pressure

Photons posses a momentum that is proportional to their frequency: $p = \hbar \omega_l / c$. This implies that for each laser beam photon that collides with a test mass surface the exchange of momentum can be modeled as an inelastic scattering, so that for a laser beam of power P_0 the average force that is acting on the test mass surface is:

$$F_0 = \frac{2P_0}{c} = \frac{2N_\gamma \hbar \omega_l}{T c^2}. \tag{3.27}$$

Following an analogous reasoning to the Shot Noise paragraph, this force on the mirror surface exhibits Poissonian fluctuations around its average value due to the quantized nature of the light beam, the Spectral Density of which can be estimated as:

$$S_{F,rad}^{1/2} = 2\sqrt{\frac{2\hbar\omega_l P_0}{c^2}}. \qquad (3.28)$$

The mirror that acts as a target for the beam is actually free to move in the horizontal plane, so that the the fluctuating force result in a mirror displacement $F = M\ddot{x}$, where M is the mirror mass. Taking the Fourier Transform of the force $\tilde{F}(f) = -M(2\pi f)^2\tilde{x}$, the Spectral Density of the mirror displacement immediately follows:

$$S_{x,rad}^{1/2}(f) = \frac{2}{M(2\pi f)^2}\sqrt{\frac{2\hbar\omega_l P_0}{c^2}}. \qquad (3.29)$$

This fluctuating mirror displacement results in a fluctuation of the output signal that must adequately referred to the input in order to be compared with the Gravitational Wave Strain. To transform the mirror displacement into a phase shift fluctuation at the output port one must use the Fabry Perot Interferometer Transfer Function T_{FP} of Eq.3.20, but the following input referencing operation that must be performed on the output phase shift eliminates the T_{FP} dependency from the final Radiation Pressure Strain Sensitivity. However, as each photon performs $O(N \approx \frac{2\mathcal{F}}{\pi})$ bounces between the cavity mirror, it results that the power inside the cavity is larger by a factor $O(N)$ than the power P_{bs} at the beam-splitter. In fact it can be more rigorously shown that [13]:

$$P_{cav} \approx \frac{2\mathcal{F}}{\pi}P_{bs}. \qquad (3.30)$$

Therefore a power fluctuation ΔP_{bs} at the input mirror gets amplified by the same factor inside the cavity $\Delta P_{cav} = \Delta P_{bs}(2\mathcal{F}/\pi)$.

Nevertheless there are a few more caveats that must be considered in order to correctly refer the mirror displacement to the input. The photons that arrive at the beam-splitter are randomly scattered into one of the two arms. As a consequence, the photon distributions in the two arms are two anti-correlated Poissonian distributions. As the interferometer is sensitive to changes in the differential length of the two arms, the contributions due to Radiation Pressure in the two arms adds up, so that the final Strain Sensitivity due to Radiation Pressure must be multiplied by a factor of 2. It can also be shown [13] that, if the mirror vibrates at a frequency f, the cavity is displaced off resonance, and the power inside the cavity is reduced by a factor $[1 + (f/f_p)^2]$. Then, the Strain Sensitivity due to Radiation Pressure results:

$$S_{h,rad}^{1/2}(f) = \frac{16\sqrt{2}\mathcal{F}}{ML(2\pi f)^2}\sqrt{\frac{\hbar P_{bs}}{2\pi\lambda_l c}}\frac{1}{\sqrt{1 + (f/f_p)^2}}. \qquad (3.31)$$

The two Shot Noise and Radiation Pressure contribution quadratically add up to give the total Quantum Noise, also called Optical Readout Noise (Fig.3.6). Shot Noise is the main limiting factor for the interferometer sensitivity at high frequencies while Radiation Pressure Noise becomes relevant at lower frequencies. Moreover, it can be noted that the two noise contibutions have different dependencies on the circulating power inside the interferometer arms:

$$S_{h,shot}^{1/2} \propto \frac{1}{\sqrt{P_{bs}}}; \qquad\qquad S_{h,rad}^{1/2} \propto \sqrt{P_{bs}}. \qquad (3.32)$$

What this relations are saying is that, when choosing the circulating power in the design phase of the interferometer, one cannot reduce an Optical Readout Noise contribution without increasing the
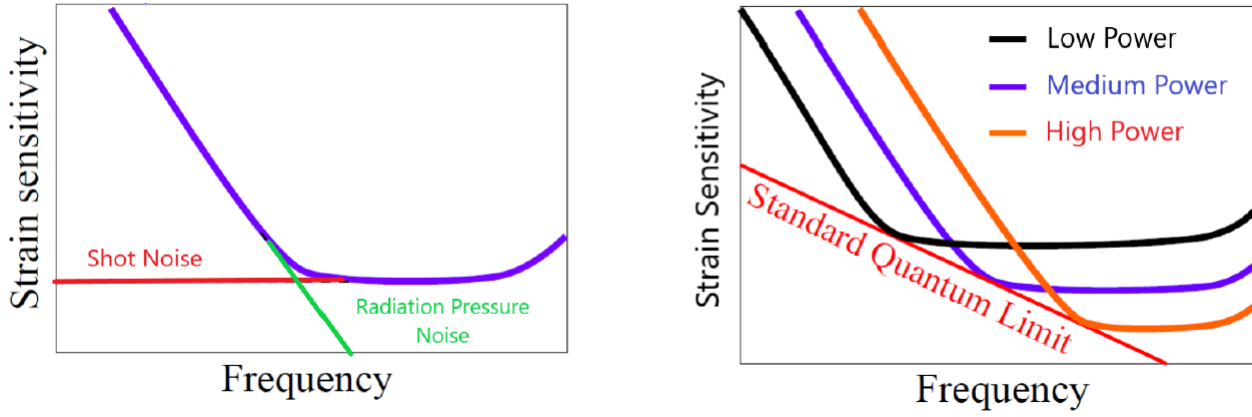
Figure 3.6: Left: Shot Noise (Red) and Radiation Pressure Noise (Green) contributions to Optical Readout Noise (Blue); Right: Standard Quantum Limit and power optimization.

other, so that a circulating power optimization process is needed to find the value that minimizes the sum of the two contributions in the frequency region of intrest. This in fact shows the remarkable fact that a (macroscopic) Gravitational Wave Interferometer aims at such an extreme accuracy in the determination of its mirror positions that its sensitivity is limited by Heisemberg Uncertainty Principle. The GW interferometer is a quantum system in which the test mass position is measured with the use of quantum particles, photons, which cause a recoil on the test mass that disturbs the measure itself. Then, upon defining:

$$f_0 = \frac{8\mathscr{F}}{2\pi} \sqrt{\frac{P_{bs}}{\pi \lambda_l c M}} \tag{3.33}$$

the Spectral Density of the Optical Readout Noise can be written as:

$$S_{h,opt}^{1/2}(f) = \left(S_{h,shot}(f) + S_{h,rad}(f)\right)^{1/2} = \frac{1}{L\pi f_0} \sqrt{\frac{\hbar}{M}} \left[\left(1 + \frac{f^2}{f_p^2}\right) + \frac{f_0^4}{f^4} \frac{1}{1 + f^2/f_p^2}\right]^{1/2}. \tag{3.34}$$

For a given value of f, the Optical Readout Noise Spectral Density $S_{h,opt}^{1/2}$ can be minimized with respect to $f_0{}^3$. The optimal value of f_0 is the one that makes equal the Shot Noise and Radiation Pressure Noise contributions, and is given by:

$$\bar{f}_0 = f\left(1 + \frac{f^2}{f_p^2}\right)^{1/2}. \tag{3.35}$$

The corresponding set of optimal $S_{h,opt}^{1/2}(f)$ values defines the Standard Quantum Limit (SQL):

$$S_{h,SQL}^{1/2}(f) = \frac{1}{2\pi f L} \sqrt{\frac{8\hbar}{M}}. \tag{3.36}$$

The Standard Quantum Limit $S_{h,SQL}^{1/2}(f)$ (Fig.3.6) represents the minimum noise spectral density which can be obtained, as long as only Optical Readout Noise is concerned, at a given value of f in a Gravitational Wave Interferometer. Hence, as it is the value of f_0 that gets experimentally optimized by a change of the circulating power keeping fixed the value of f, in a GW Interferometer the Standard Quantum Limit Sensitivity can be reached at best only at a specific frequency.

---

[3]That is, it can be minimized with respect to the circulating power inside the interferometer arms, as $f_0 \propto \mathscr{F}$, $\sqrt{P_{bs}}$.

3.3.4 Thermal Noise

Thermal noise in test masses and suspension systems is the current limiting factor for the sensitivity of second generation ground-based interferometer at frequencies below $200\,\text{Hz}$[4]. Thermal noise in the suspension systems primarily arises from losses in the fused silica fibers that hang the test mass to the attenuator structure. This contribution needs to be numerically computed with finite-elements models that include bulk, surface and thermoelastic components of the fibre material and that account for the specific noise-reducing fibre shape. Thermal noise in test masses on the other hand can be adequately studied using analytical models.

There are two fundamental origins of thermal noise in optical components. The first is the standard Brownian Noise, due to the thermal energy of the jittering atoms of the test mass that causes a thermally driven fluctuation of the reflective surface of the element. Thermal energy $k_b T$ is present as the component is operated finite temperature T.

The second component is a less intuitive form of thermal noise that arises from temperature fluctuations. The local microscopic temperature of a component is not a constant value but fluctuates around an average temperature T. Due to the fact that many material properties, like the coefficient of thermal expansion α or the refractive index n, are temperature dependent, temperature fluctuations induces phase and position fluctuations. The process that is associated with α is called Thermo-Elastic Noise whereas other processes are referred to as Thermo-Refractive Noise or Thermo-Optic Noise.

Brownian Thermal Noise   Brownian Noise of the Bulk Material of the interferometer mirrors can be calculated by direct application of the Fluctuation-Dissipation (FD) Theorem. In a Gravitational Wave Interferometer a laser beam is shining on the surface of the cylindrical test masses. The light reflected by the mirrors acquires a phase shift that contains information about the displacement of the test mass surface. Brownian Thermal Noise induces vibrations in the test mass rest position $x(t)$ in the horizontal plane that gets eventually converted in a phase shift at the output port. Then the first thing to be done in order to analyze Brownian Thermal Noise in bulk material is to find the Spectral Density $S_{x,\,Bulk}^{1/2}(f)$ of its induced fluctuations in $x(t)$. Throughout the derivation is assumed that the mirror surface is infinite in size, so that the boundary effects of the beam-test mass interaction are negligible, and that the test mass is in thermal equilibrium at temperature T.

In its most general form the Fluctuation-Dissipation Theorem states that the Thermal Noise Spectral Density of a generic readout variable is given by [23]:

$$S_x^{1/2}(f) = \frac{k_b T}{\pi^2 f^2} \big| \operatorname{Re}[Z(f)] \big| \tag{3.37}$$

where k_b is Boltzman's constant. The complex impedance $Z(t)$ can be computed by applying a generalized force $F(t)$ to the test mass that will generate a consequent time evolution of the observable variable $x(t)$. By denoting with $F(f)$ and $x(f)$ the Fourier Transforms of the driving force and the readout variable respectively, the Fourier Transform of the complex impedance $Z(f)$ is expressed as:

$$Z(f) = 2\pi i f \frac{x(f)}{F(f)}. \tag{3.38}$$

In the case of thermal noise in the Gaussian Beam-Test Mass system, the arbitrary driving force can be modelled with an oscillating force which intensity is gaussianly distributed across the mirror surface. This will result in an oscillating pressure acting on the mirror surface:

$$P(\bar{r}, t) = F_0 \cos(2\pi f\, t) f(\bar{r}) \tag{3.39}$$

---

[4]There are also other technical noises sources, such as seismic noise, that significantly contribute to the overall noise in the sub-200 Hz region, but they will not be examined in detail in this work.

where $f(\bar{r}) = \frac{1}{\pi r_0^2} e^{-r^2/r_0^2}$ is the gaussian intensity profile. This oscillating driving force will consequently feed a dissipated power W_{diss} in the test mass due to internal frictions. Then it can be shown [24] that for the above configuration the real part of the Fourier Transform of the system complex impedance is given by:

$$\big| \text{Re}[Z(f)] \big| = \frac{2W_{diss}}{F_0^2}. \tag{3.40}$$

Inserting Eq.3.40 in the FD Theorem 3.37, the following relation is obtained:

$$S_x^{1/2}(f) = \frac{2k_b T}{\pi^2 f^2} \frac{W_{diss}}{F_0^2}. \tag{3.41}$$

Then, assuming homogeneous dissipation, the W_{diss} power that is absorbed by the mirror can be expressed as:

$$W_{diss} = 2\pi f U_{max} \phi^{Bulk}(f). \tag{3.42}$$

In the above equation $\phi^{Bulk}(f)$ is the Mechanical Loss Angle of the mirror material, while U_{max} is the elastic deformation energy in the instant when the test mass is maximally contracted or extended under the action of the oscillatory pressure 3.39. Then, under the above assumptions, an explicit expression for U_{max} can be derived for the Gaussian Beam-Test Mass system ([24], [25]):

$$U_{max} \approx \frac{F_0^2(1-\nu)}{2\pi^{1/2} Y_s r_0} \tag{3.43}$$

where ν and Y_s are the Poisson's Ratio and the Young's Modulus of the material respectively. Eq.3.43 is valid up to first order corrections $O(r_0/R)$, where r_0 is the Gaussian Beam Radius and R the Characteristic Size of the cylindrical Test Mass. Substituting Eq.3.42 and Eq.3.43 back into Eq.3.41, it is finally obtained an expression for the Mirror Displacement Spectrum of Brownian Thermal Noise in the Test Mass Bulk Material:

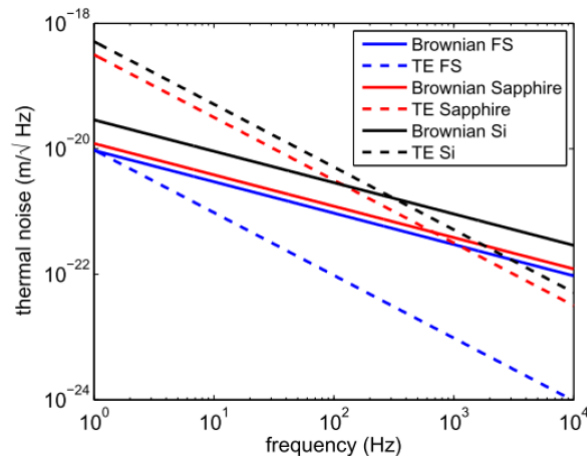$$S_{x,\,Bulk}^{1/2}(f, T) = 2k_b T \frac{1-\nu}{\pi^{3/2} f Y_s r_0} \phi^{Bulk}. \tag{3.44}$$

Figure 3.7: Comparison of the Brownian and Thermo-Elastic noise at room temperature (300K) for various Advanced Detectors Test Masses candidate materials (Fused Silica, Sapphire, Silicon).

Similar to Brownian Thermal Noise in the bulk materials of the test mass, the coatings also show

Brownian thermal noise. An analogous computation can be perform to extract the Mirror Displacement Spectrum of Brownian Thermal Noise in Coatings [25]:

$$S_{x, Coat}^{1/2}(f, T) = 2k_b T \frac{1 - \nu}{\pi^{3/2} f Y_s r_0} \phi_{eff}^{Coat}. \tag{3.45}$$

In the above equation ν and Y_s still refer to Poisson's Ratio and Young's Modulus of the bulk material, while ϕ_{eff}^{Coat} is an effective Loss Angle for the Coating Stack of Dielectric Materials, the final form of which has a detailed expression that needs further assumptions and computations to be obtained[5] [26].

In order to properly compare the Brownian Thermal Noise displacement spectra obtained in Eq.3.44 and Eq.3.45 with Gravitational Wave Strain h, they must be refered to the input. This can be easily made by remembering that the effect of a Gravitational Wave on the length L of a Fabry-Perot Cavity is to change it by the amount $\Delta L = hL$. This implies that, in order to input refer the mirror displacement induced by Thermal Noise, it must be divided by the cavity length L so that the effect is equivalent to a Gravitational Wave of strain h. As opposed to Quantum Noise, the Finesse of the cavity does not enter here in the input referring operation, as both GW and Thermal Noise effects get amplified by the same factor $O(N)$ inside the cavity.

Then, the Strain Spectral Density of Brownian Noise in Bulk Materials and Coatings, is simply given by:

$$S_{h, Bulk}^{1/2}(f, T) = \frac{2k_b T}{L} \frac{1 - \nu}{\pi^{3/2} f Y_s r_0} \phi^{Bulk}; \tag{3.46}$$

$$S_{h, Coat}^{1/2}(f, T) = \frac{2k_b T}{L} \frac{1 - \nu}{\pi^{3/2} f Y_s r_0} \phi_{eff}^{Coat}. \tag{3.47}$$

Thermo-Elastic Noise   Thermo-Elastic Noise of the Bulk Material arises from stochastic temperature fluctuations that are translated into displacement noise by means of the coefficient of thermal expansion α. Its contribution to the total Thermal Noise can be computed by applying the Fluctuation-Dissipation Theorem, in analogy to the Brownian Thermal Noise estimate in the previous paragraph. The estimate of the complex impeadance requires lengthier computations in this case, as it must be derived by solving the system of the thermal conductivity and strain-displacement equations for the mirror [27], assuming that the only dissipation mechanism in the mirror is thermo-elastic damping

---

[5]For completeness, it can be shown the result obtained in [26] for the effective Coating Loss Angle, which is valid for small Poisson's Ratio of the coating materials:

$$\phi_{eff}^{Coat} = \frac{t}{\sqrt{\pi} r_0} \left(\frac{Y_s}{Y_\perp} \phi_\perp + \frac{Y_\parallel}{Y_s} \phi_\parallel \right)$$

where t is the total thickness of the coating layer. The effective Young's Moduli $Y_\perp$, $Y_\parallel$ and Loss Angles $\phi_\perp$, $\phi_\parallel$ in the above expression are defined in terms of the coating materials Young Moduli Y_i, Loss Angles ϕ_i and thicknesses t_i ($i = 1, 2$ indicates the different coating layer materials) as:

$$Y_\perp = \frac{t_1 + t_2}{\frac{t_1}{Y_1} + \frac{t_2}{Y_2}},$$

$$Y_\parallel = \frac{Y_1 t_1 + Y_2 t_2}{t_1 + t_2},$$

$$\phi_\perp = \frac{Y_\perp}{t_1 + t_2} \left(\frac{t_1}{Y_1} \phi_1 + \frac{t_2}{Y_2} \phi_2 \right),$$

$$\phi_\parallel = \frac{Y_1 t_1 \phi_1 + Y_2 t_2 \phi_2}{Y_\parallel (t_1 + t_2)}.$$

and approximating the mirror as an half space. Refering to [28] for detailed computations, the displacement spectrum of Thermo-Elastic Noise in Bulk Materials is given by:

$$S_{TE,bulk}^{1/2}(f,T) = \frac{8}{\sqrt{2\pi}}\alpha^2(1+\nu)^2\frac{k_bT^2\kappa}{\rho^2c_p^2f^2r_0^2} \tag{3.48}$$

where ρ,κ and c_p are the density, thermal conductivity and specific heat capacity of the material respectively. The above equation is valid in the 'adiabatic' regime, that is if the thermal diffusion lenght of the material l_{th} is smaller than the beam diameter r_0. The thermal diffusion length of is defined as:

$$l_{th} = \sqrt{\frac{a^2}{f}} = \sqrt{\frac{\kappa}{\rho c_p f}} < r_0. \tag{3.49}$$

Outside of the adiabatic regime the thermo-elastic effect gets weaker. This is because the adiabatic condition 3.49 corresponds to the requirement that, during one period of oscillation, all temperature fluctuations that are present at the observation volume stay inside this volume. Then, if thermal conductivity is increased or lower frequencies are considered, l_{th} gets larger and the temperature fluctuations are averaged out faster.

The non-adiabatic regime correction becomes important for low temperature applications, as most optical materials exhibit a peak in the thermal conductivity at cryogenic temperatures. A detailed calculation can be performed to estimate the displacement noise for Thermo-Elastic Noise incorporating the non-adiabatic case [29], that can be expressed as:

$$S_{TE,bulk}^{1/2}(f,T) = \frac{8}{\sqrt{2\pi}}\alpha^2(1+\nu)^2\frac{k_bT^2r_0}{\kappa}J[\Omega] \tag{3.50}$$

where $J[\Omega]$ is a function of the dimensionless variable $\Omega = \omega/\omega_c$ that quantifies the relative frequency compared to the adiabatic limit frequency $\omega_c = a^2/r_0^2$:

$$J[\Omega] = \sqrt{\frac{2}{\pi^3}}\int_0^\infty du \int_{-\infty}^\infty dv \frac{u^3e^{-u^2/2}}{(u^2+v^2)\big((u^2+v^2)^2+\Omega^2\big)} \tag{3.51}$$

3.3.5 Other Noises

Despite the fact that the noise sources that were analyzed in the previous sections are the dominant contribution across all the operating frequency range of currently operating interferometers, there are other noise sources that contribute to the general noise budget of the detector. In fact these alternative noise contribution are not secondary as they have a significant indirect effect on the overall noise budget, as the effort to minimize them eventually reflects in a Thermal Noise increase or in a financial cost increase that subtracts precious resources to major noise contributions suppression. Detailed evaluation of all noise sources is crucial during the design phase of an interferometer and in the case of new generation detectors it will be even more important to extensively account for all possible contributions.

Seismic Noise   Earth's ground is in perpetual motion, with an average vibration amplitude of $O(10^{-6}\,\text{m})$. There are different causes of different nature that contribute to this continual vibration. In the $1-10\,\text{Hz}$ region Cultural Noise, that is ground vibration caused by human activities and infrastructures such as road and train traffic, and wind noise are the main contibutions. This adds up to the micro-seismic background that affect GW Interferometers in the form of surface waves that ultimately shake test masses.

The amplitude of the Seismic Noise vibration are more than ten orders of magnitude larger than the

mirror displacemnt values that a GW interferometer aims to detect, so that there is need for a dedicate suspension system that is able to decouple the test masses from surrounding oscillations. A typical suspension chain is obtained cascading a set of passive mechanical filters providing a suited attenuation from seismic and acoustic noise above a certain cut-off frequency. Below this frequency value an active feed-back control strategy is developed by using sensors and actuators disseminated along the suspension chain and keeping the interferometer at its working point via feedback systems.

In the VIRGO interferometer, the upper part of the suspension chain is called SuperAttenuator
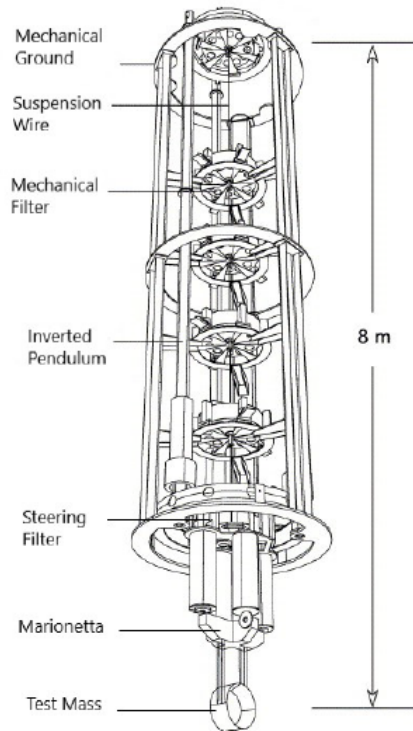

Figure 3.8: Scheme of VIRGO's SuperAttenuator.

(Fig.3.8) and it is essentially a N-stage pendulum supported by a three-leg elastic structure, called Inverted Pendulum. In an N-stage pendulum, at much higher frequencies than its normal modes, the horizontal displacement of the suspension point is transmitted to the last stage with an attenuation proportional to f^{-2N}. This exponential attenuation factor allows to reach the desired seismic noise suppression level in second generation interferometers with a 5-stage pendulum.

The Optical Payload is intead the last suspension stage and it is designed to couple the test mass to the SA chain, as well as steering the mirror through internal forces exerted from the last Superattenuator element to compensate the residual Seismic Noise at lower frequencies. This end structure is formed by two active components, the Marionette that is used to control the mirror position by means of coil-magnet actuators acting between the last stage upper part suspension and the marionette arms itself, and the Recoil Mass that is used to protect and steer the mirror. Particular attention has to be focused on the mechanical elements which connect the mirror to the last suspension stage as they can easily degrade the intrinsic mechanical losses of the system. In order to suppress mechanical losses that happen at interfaces of different materials, the test mass-suspension wire system in the advanced second generation detector is made from a monolithic element of fused silica.

Newtonian Noise   Stochastic fluctuations of the local gravitational field are usually referred to as Newtonian Noise or Gravity Gradient Noise. Local variations in the gravitational field result in a new-

tonian force acting on the test masses, in analogy to the ones exerted by Gravitational Wave perturbations. The most important Newtonian Noise contribution comes from micro-seismic noise, which produces mass density fluctuations, and consequently gravitational field fluctuations, in the Earth's ground that surround the detector. Modern GW interferometers are so sensitive that even the changing gravitational attraction of water clouds due to atmospheric turbulences gives a non negligible contribution to Newtonian Noise.

Gravity Gradient Noise is the most fundamental type of noise, in the sense that there is no way to shield it. There are different available strategies that can be employed to mitigate the impact of Gravity Gradient Noise. An active strategy consists in deploying a network of sensors to measure ground displacement and atmospheric pressure variations so that their effect on the mirrors can be modelled and subtracted from Gravitational Wave signals. A passive strategy for minimizing Newtonian Noise consists instead in building the interferometer in an underground site to reduce the impact of atmospheric perturbations and superficial seismic waves, as it was done for the Large Scale Cryogenic Gravitational Wave Telescope (LCGT) located in the Kamioka mine, Japan.

Scattering and n Noise   Ambient pressure air exhibits refraction index n fluctuations. Fluctuations in air density induce fluctuations of n which generate phase fluctuations as the speed of light is c/n. To minimize the n fluctuations induced noise the light beam in Advanced Gravitational Wave interferometers travels inside an ultra-high vacuum pipe, with pressure of $O(10^{-9}\,\mathrm{mbar})$[6]. Moreover, the residual gas must be free of condensable organic molecules, in order to keep the optical surfaces clean. Also scattered light inside the arms constitutes a relevant noise source in GW interferometers, as it can interact with the pipe walls, thereby getting modulated by its seismic noise, and then get rediffused back in the beam by reflection on a mirror. As a consequence, diffusion of circulating light inside the Fabry-Perot cavities must be kept below few parts per million. For this purpose, cavity mirrors are polished to a 0.5Å rms micro-roughness over a diameter of $O(20\,\mathrm{cm})$.

---

[6]The vacuum pipes enclose all the interferometer arm, so that they are $3-4\,\mathrm{km}$ in lenght and around $1.2\,\mathrm{m}$ in diameter in order to contain the diffraction-limited laser beam. This results in a total volume of about $9000\,\mathrm{m}^3$, that is larger than the LEP particle accelerator at CERN. Pumping such a huge volume to ultra-high vacuum pressure constitutes not only a technological challenge but also a source of issues and delays in case of incidents inside the arms.

Chapter 4

The Einstein Telescope

The second generation of Gravitational Wave Interferometers has succeded in the first detection of a Gravitational Wave Signal in 2015 and in the last few years, thanks to periodical improvements in the detector set-ups and readout systems, the frequency of the claims of new GW signals constantly increased, bringing the total number of confirmed event detections up to fifty. Despite the huge importance of this achievement, that ultimately led to the assignment of the 2017 Nobel Prize in Physics to three scientist that played a key role in the foundation of the LIGO/VIRGO Collaboration (K.Thorne, R.Weiss, B.C. Barish), the quantity and signal-to-noise ratio of the detections made in second generation detectors is still too low for precise astronomical studies of the GW sources and for consistently complementing optical and X–ray observations in the study of fundamental systems and processes in the Universe. An increase of the Signal-to-Noise Ratio in the detected signal could also be crucial to investigate over beyond General Relativity theories, as the relativistic description of compact object mergers breaks down in the last collision and ringdown instants of the event.

Due to these considerations, starting from the late '00s, the Gravitational Wave community started investigating a third generation of detectors with a considerably improved sensitivity that will open the era of routine GW astronomy. The Einstein gravitational wave Telescope (ET) is an European Collaboration project for a third generation GW Interferometer that will aim at a sensitivity about a factor 10 better than the current advanced detectors. Research and development on the innovative technologies that are needed to reach ET ambitious design sensitivity have slowly but steadily evolved in the last decade and the project is now mature to receive official approval from the institutions for the start of its construction phase. Moreover another third generation detector, the Cosmic Explorer funded by the United States of America, is planned to support Einstein Telescope observations.

Einstein Telescope Design encompasses most of the technological features that allowed second generation interferometers to achieve the first Gravitational Wave detections but will also implement new solutions to reduce the fundamental and technical noises that currently limit the sensitivity of advanced LIGO and VIRGO detectors. In these last years that precede construction, research on new candidate materials and technologies for the ET Interferometers are flourishing and this thesis work wishes to contribute to the developement by performing an innovative optical absorption measurment in silicon crystals at cryogenic temperatures. In order to understand why it is crucial for the next generation interferometers to characterize the properties of optical substrate materials at cryogenic temperatures, it is necessary to present a brief analysis of the main strategies and technological features that are included in the Einstein Telescope design to attempt at improving second generation sensitivity over a wide range of frequencies.
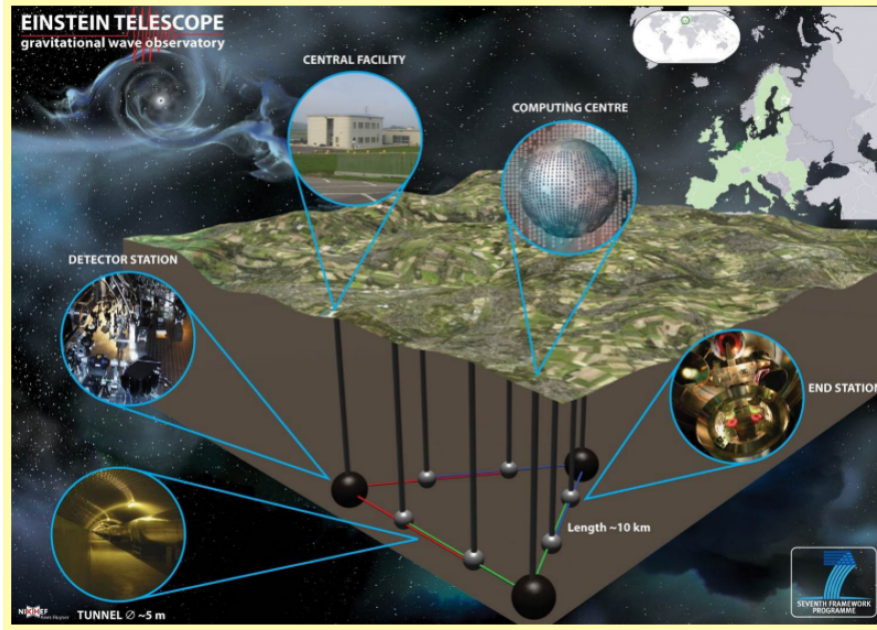
Figure 4.1: Artist's view of Einstein Telescope.

4.1 Detector Layout

In Sec.3.3 the main noise contribution that limits the sensitivities of the currently operating ground-based detectors were discussed and their spectral densities were derived. The main feature of a second generation dector noise budget were highlighted: thermal noise is the limiting factor for frequencies below $100 - 200\,\mathrm{Hz}$ while quantum noise becomes the dominant contribution at higher frequencies. Einstein Telescope aims at improving second generation performances over the entire detection frequency band from few Hz to $10\,\mathrm{kHz}$, so that it is needed to adress both the main limiting noise contributions in a single detector.

In order to find a strategy to achieve this wideband sensitivity improvement, it is useful to recall the Brownian Thermal Noise and Shot Noise spectral density that were derived in Eq.3.26 and Eq.3.46:

$$
\begin{aligned}
S_{h,\,brown}^{1/2}(f) &= \frac{2k_b T}{L}\frac{1-\nu}{\pi^{3/2}fY_s r_0}\phi; \\
S_{h,\,shot}^{1/2}(f) &= \frac{1}{8\mathcal{F}L}\sqrt{\frac{4\pi\hbar\lambda_l c}{\eta P_{bs}}}\sqrt{1+\left(\frac{f}{f_p}\right)^2}.
\end{aligned}
\tag{4.1}
$$

In the above expressions it is manifest that the most intuitive approach to reduce both noise contributions is to elongate the interferometer arms ($S_{h,\,brown}^{1/2}$, $S_{h,\,shot}^{1/2} \propto L^{-1}$). This strategy will be followed in Einstein Teslescope interferometers, as their arms are planned to be $10\,\mathrm{km}$ in length. This design arm length is in fact close to the maximum achievable arm length for a ground-based interferometer, considering in particular that the third generation of Gravitational Wave interferometers will be built in underground sites to reduce Newtonian Noise[1].

If one then desires to further reduce shot noise, the only viable strategy is to increase the circulating power inside the interferometer arms, either by increasing the input power at the beam splitter or the cavity Finesse ($S_{h,\,shot}^{1/2} \propto \mathcal{F}^{-1}$, $P_{bs}^{-1/2}$). This is however detrimental for the Brownian Thermal Noise

---

[1]The arm length limiting factor is not so much the technological aspect of managing a very long armed interferometer, but rather the economical cost that comes from building and operating an underground facility of such dimensions.

contribution because raising the circulating power inside the Fabry-Perot Cavities would increase the temperature of the mirrors ($S_{h,brown}^{1/2} \propto T$). One could think of preventing this problem by enlarging the section of the mirror suspensions so to have a better evacuation of the excess absorbed power, but this would in turn increase the Suspension Thermal Noise, that is the actual limiting factor for the detector sensitivity below 10 Hz, besides spoiling Seismic Isolation. Hence there are no other efficient strategies that allows to tackle both Thermal Noise and Shot Noise in a single interferometer than increasing the arm length. For this reason Einstein Telescope follows a different approach respect to second generation GW interferometers, that is to build a pair of parallel interferometers, one of which can be optimized for low frequency detection ($2 - 40$ Hz) while the second can be independently tuned for higher frequencies observation.
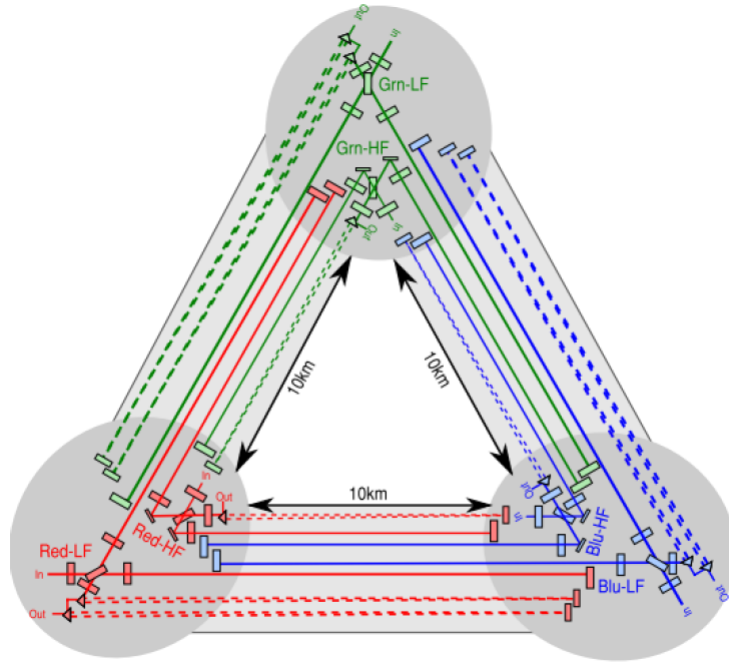

Figure 4.2: The final Xylophone Configuration for Einstein Telescope.

The final construction stage of the Einstein Telescope will consist of three nested detectors, each one formed by an aligned pair of dual-recycled Michelson Interferometers with Fabry-Perot Cavities, arranged in a triangular configuration (Xylophone Configuration), as shown in Fig.4.2. It can be shown that the sensitivity of a triangular configuration is comparable to the one of a right-angled interferometer with same construction parmeters, while offering a more isotropic antenna pattern [30].

The interferometers will be built in an underground location ($100 - 200$ m below surface) to minimize Seismic and Newtonian Noise contributions that would spoil detector sensitivity at frequencies below 10 Hz. Research is ongoing to find a site in Europe that offers an high level of geologic and seismologic stability, while possibly presenting an already existing infrastructure to cut costs and time on tunnel and shaft construction. In order to isolate test masses from ground seismic vibrations and local disturbances, each one of them will be hanged to a suspension system with similar structure to the ones employed in second generation interferometers.

4.2 Detector Noise Budget

The design sensitivity for a single pair of High Frequency and Low Frequency interferometers of the Einstein Telescope detector is shown in Fig.4.3, together with the detailed noise budget for both HF

and LF detectors. Different strategies are employed in the two HF and LF interferometers to adress the dominant noise contributions in each frequency range of intrest.
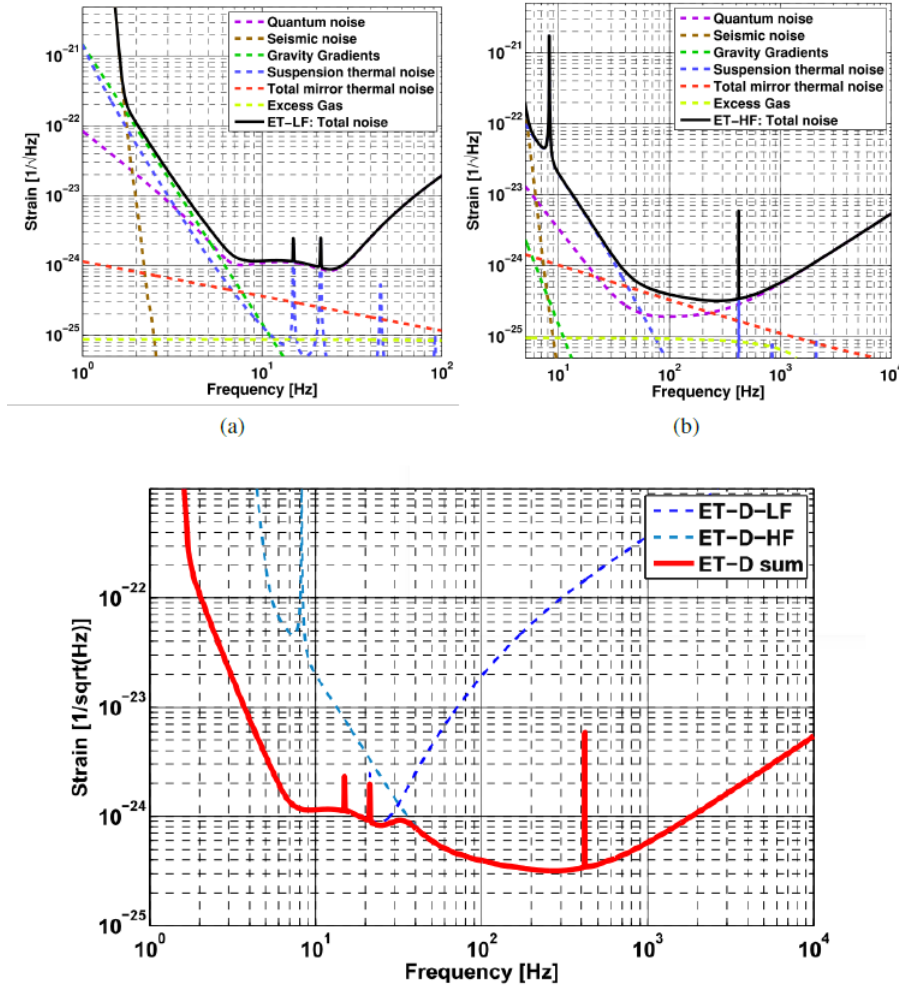

Figure 4.3: Design Sensitivity for the Low Frequency (a), High Frequency (b) and LF-HF sum (c) detectors of Einstein Telescope [31].

Quantum Shot Noise will be the main limiting factor for the High Frequency detector at frequencies above 200Hz. As shown in the expression for the Shot Noise Spectral Density that was obtained in the previous chapter (Eq.3.26), for minimizing it the circulating power in the interferometer arms needs to be increased as much as possible. Design specifications aim at operating the HF interferometer with a light power of $O(10^6$ W) inside the Fabry-Perot Cavities[2]. As a consequence the HF interferometer must be operated at room temperature, since material and coating technologies are not mature enough to handle a several MegaWatt power in input to the test masses. The massive circulating power that acts on the test masses and the high operating temperature cause the High Frequency Detector sensitivity between $40\,\mathrm{Hz}$ and $200\,\mathrm{Hz}$ to be limited by mirror thermal noise. Another important implication of the fact that the HF interferometer will be operated at room temperature is that all the succesful technological solutions developed for test mass coatings and suspension systems in second generation detectors can be directly implemented, as the input laser will be operated at usual $1064\,\mathrm{nm}$ wavelength and the mirrors will be built from fused silica.

The crossover frequency of the sensitivities of the LF and HF interferometers is at about $35\,\mathrm{Hz}$. For frequencies below $1.7\,\mathrm{Hz}$, the Low Frequency Detector sensitivity will be limited by seismic noise.

---

[2]For comparison, the maximum circulating power that is designed to be hold inside aLIGO arm cavities is $750\,\mathrm{kW}$, five times lower than the $3\,\mathrm{MW}$ design circulating power for the High Frequency ET detector.

In order to minimize the Seismic Noise contribution and to push its relevance at the lowest possible frequencies, a modified version of the VIRGO SuperAttenuatur will be developed to decouple the test masses from gruond vibration. The Modified SuperAttenuator will consist of 6 mechanical filters for a total chain height of $17\,\mathrm{m}$, compared to the $9\,\mathrm{m}$ with 5 filters configuration of the VIRGO suspension system. Newtonian Noise limits the LF detector sensitivity in the $[1.7 - 6]$ Hz frquency range. As already discussed in Sec.3.3, the only possible approach to Newtonian Noise mitigation is post-processing subtraction. To this purpose a set of displacement sensors will be placed all around the interferometers arms to monitor for ground mass displacement of seismic origin, in the hope that it will be possible to correlate the independently recorder ground displacement with mirror displacement detected by the interferometer. The Gravity Gradient Noise subtraction strategy for ET is still undeveloped at the time of writing, so that the curves shown in Fig.4.3 show a conservative estimate for the NN contribution. After the sensor array for Newtonian Noise subtractiobn will be completed, Suspension Thermal Noise will become the limiting factor in the $[1.7 - 6]$ Hz frequency band. Ultimately, Quantum Noise will be the limiting factor also in the Low Frequency Detector, at frequencies above $6\,\mathrm{Hz}$.

Quantum Noise will limit the sensitivities of both LF and HF detectors of Einstein Telescope, either in the form of Shot Noise or Radiation Pressure Noise. Apart from the conventional Quantum Noise minimization strategies such as the sharp circulating power increase inside the HF Fabry-Perot cavities, that are capable of decreasing a single QN contribution at the expense of an increase in the second contribution, a broadband Quantum Noise reduction can be obtained with the injection of squeezed states of light with a frequency-dependent squeezing angle into the output port of the interferometer [34]. An electro-magnetic field is in a squeezed state if the quantum uncertainty of one of its quadrature is smaller than the one of a coherent state, at the expense of a larger quantum uncertainty associated to its conjugated quadrature, to fulfill Heisenberg's uncertainty principle. Then the squeezing angle can be oriented in a frequency dependent way so that phase fluctuation noise is reduced in the frequency band where Shot Noise is more relevant, increasing the contribution of the irrelevant Radiation Pressure noise due to increased amplitude fluctuations, and viceversa, thus overcoming the Standard Quantum Limit in a wide frequency range. A frequency dependent squeezing source that is capable of reaching at least $4\,\mathrm{dB}$ of broadband quantum noise reduction has been realized both in KAGRA and MIT ([35],[36]). An implementation of the FDS technology in all advanced interferometers is planned for the start of the O4 acquisition run (2022/23).

4.3   Scientific Reach of the Einstein Telescope

A third generation Gravitational Wave Interferometer such as the Einstein Telescope will make it possible to observe a variety of the most extreme phenomena in the universe, providing a new tool for expanding our knowledge of fundamental physics, cosmology and relativistic astrophysics. First of all, Einstein Telescope pledge to detect the same type of events that were observed during the first data-taking runs of the aLIGO and AdV detectors, but at larger distances, hence dramatically increasing the detection frequency, allowing to build up a solid statistic in compact binary mergers analysis. The new generation detector is expected to observe BNS up to a redshift of $z \sim 2$, stellar-mass BBH population at the edge of the Universe ($z \sim 15$) and intermediate-mass BBH out to a typical redshift of $z \sim 5$[3]. Moreover ET is expected to be sensitive to Gravitational Wave signals of different nature respect to the ones already observed, such as supernovae collapse out to a distance of $1.5 \times 10^7\,\mathrm{ly}$, within which the expected event rate is $1/\,\mathrm{year}$. Other important classes of gravitational wave events that could be detected by an instrument with a sensitivity as the one that was presented in Fig.4.3 are, for instance, gravitational collapses associated with Gamma Ray Bursts, isolated Neutron Star GW

---

[3]For comparison, the most distant events that were identified with the aLIGO and AdV detectors are located at distances of $O(z = 0.1)$.

signals or even the Primordial Gravitational Wave Background.

The following section aims at presenting the main scientific objectives of the Einstein Telescope project and the open issues in physics that could be addressed by enhancing the range of Gravitational Wave observations.
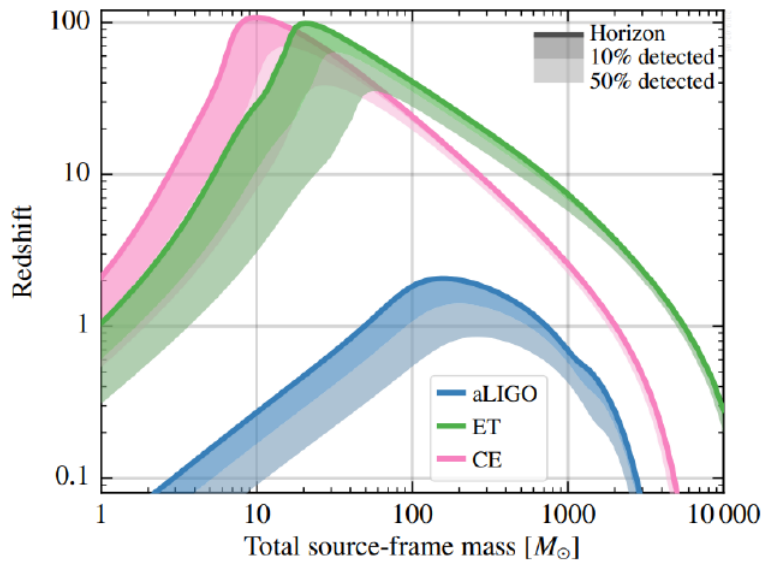

Figure 4.4: Astrophysical reach of the Einstein Telescope for equal-mass, nonspinning binaries isotropically distributed in sky location and inclination, compared to one of the aLIGO and Cosmic Explorer detectors [33].

4.3.1 Fundamental physics and strong field tests of General Relativity

Einstein Telescope will be capable of observing sources in dense enviroments of ultra-strong gravity and will therefore provide a cosmic laboratory for understanding phenomena and matter in extreme conditions of density, temperature, and magnetic fields. The detection of such events can potentially answer astonishing questions in fundamental physics. Moreover, an instrument with improved sensitivity respect to the currently operating advanced detectors will give a clearer picture of BBH interaction close to the merger phase, providing an insights into the nature of Black Holes spacetimes and of gravity in ultra-strong fields.

Polarization of gravitational waves According to the theory of General Relativity, Gravitational Waves have only two polarizations $(+, \times)$, as shown in Sec.2.1. However, in scalar-tensor theories of gravity, such as the Brans-Dicke theory, Gravitational Waves have six physical polarizations. These additional polarizations could cause motion of test masses longitudinal to the direction of propagation, conversely to the transverse nature of the Plus and Cross polarization effect, as well as different oscillation patterns in the transverse plane respect to the relativistic ones. High Signal-to-Noise Ratio events that are going to be provided by Einstein Telescope will be able to shed light on the presence of additional polarizations in Gravitational Wave signals, eventually confirming or ruling out a whole class of alternative theories to General Relativity.

Bounding graviton mass In Einstein's theory gravitons, the quanta of the gravitational field, are massless particles. As a consequence, gravitational information and radiation travel at the speed of

light. Massive graviton theories are natural extensions to General Relativity. In such theories Gravitational Waves would not travel at the speed of light and this could be tested throgh multimessenger observation of distant gravitational wave sources, by measuring the difference in the arrival times of gravitational and electro-magnetic radiation. The major source of uncertainty in such an estimate of the graviton mass relies in the complex nature of gravitational collapse in supernovae and coalescing binaries which makes it difficult to accurately compute the initial retard of EM emission respect to the GW signal.

There is indeed another method for the determination of the graviton mass that is capable of yelding more robust results. This alternative method exploits the fact that in massive graviton theories Gravitational Waves would suffer disperson. More specifically, the graviton speed of propagation v_g will depend on its wavelength λ as $v_g \approx \left(1 - (\lambda/\lambda_g)^2\right)$, where λ_g is the Compton wavelength of the graviton[4], so that the higher frequency band of the Gravitational Wave will arrive earlier than the lower frequency part of the signal. The resulting distortion of the signal respect to the relativistic prediction is proportional to the distance of the GW source respect to the observer. Then, the ability to detect BBH mergers at the edges of the universe may prove critical for estimates of the graviton mass and consequently for confirming or ruling out massive graviton extensions to General Relativity.

The first Gravitational Waves observations were already sufficient to put a constraint on the graviton mass of $m_g \leq 1.2 \times 10^{-22}$ eV [37]. This upper bound on the graviton mass will be considerably improved when multimessenger observations and detection of BBH mergers at cosmological distances will become a routine operation.

Measuring the dark energy equation of state and its variation with z Starting from the late '90s, evidence has emerged suggesting that the expansion of the Universe is accelerating. This evidence can be explained by considering modifications of General Relativity at large length scales or by introducing a new contributor to the mass/energy content of the Universe, the Dark Energy[5]. The time evolution of an homogeneous and isotropic universe is described by the combination of the Friedmann Equations and an additional Equation of State for the Dark Energy fluid that drives the accelerated expansion of the cosmic spacetime. The Equation of State links the pressure and density of the Dark Energy fluid and takes the general form:

$$p_{DE} = \omega(z)\rho_{DE}. \tag{4.2}$$

The traditional model for Dark Energy is the one of an exotic negative pressure fluid ($\omega = -1$). At present, the most accurate constraints on the Dark Energy Equation of State parameter ω are determined combining the Planck Mission data on Cosmic Microwave Background with galactic redshift catalogues built upon Type Ia Supernovae observations and Baryon Acoustic Oscillations measurements [38]: the obtained 1σ bound $\omega = -1.03 \pm 0.03$ is compatible with the standard model for the Dark Energy fluid.

The main source of uncertainty in the above constraint comes from the fact that galactic redshift determination currently rely on the Cosmic Distance Ladder (see Sec.4.3.3). This problem can be bypassed with the employment of routine multimessenger observation data, obtaining more reliable measurements of compact binary inspirals redshifts as a function of their luminosity distance and thus more accurate constraints on ΛCDM parameters such as ω.

---

[4]The result is valid at first order approximation in $x = (\lambda/\lambda_g)^2$.

[5]The most general form of Einstein's Field Equation 2.1 can be expressed as:

$$R_{\mu\nu} - \frac{1}{2}g_{\mu\nu}R + \Lambda g_{\mu\nu} = \frac{8\pi G}{c^4}T_{\mu\nu}$$

where Λ is the 'Cosmological Constant' coefficient. The Cosmological Constant has the same effect as an intrinsic energy density of the vacuum, to which is associated a vacuum pressure governed by the vacuum fluid Equation of State.

Testing Black Hole Theorems The physicality of Black Holes has been widely demonstrated thanks to a large number of experimental evidences that emerged in the last fifty years. Despite the evidence for their existence, most of the features of this extremely compact objects and of the nature of space-time that surrounds them remains unknown.

Due to the Uniqueness theorem, which states that the Kerr metric is the unique end state of gravitational collapse, it is generally accepted that rotating Black Holes are described by the Kerr Metric of General Relativity (see Sec.6.6 of [14] for more details). However, the theorem is based on several assumptions, namely that the system is stationary and axisymmetric, that there is a spacetime horizon and that there are no closed timelike curves. If one of these assumptions were violated, then objects that deviate from the Kerr metric could exist.

These assumptions on the nature of spacetime surrounding a Black Hole can be tested by monitoring the dynamics of an object that transit in proximity to a BH horizon. This could be enabled by Einstein Telescope with the detection of Intermediate-Mass-Ratio Inspirals (IMRIs), that are inspirals of a $m \sim 1 M_\odot$ object into a $M \sim 100 M_\odot$ Black Hole, thanks to its enhanced sensitivity in the $[1, 10]$ Hz frequency band. In such an asymmetric system, many Gravitational Wave cycles are emitted while the smaller object is in the strong field region close to the larger object, allowing to obtain information on the spacetime structure surrounding the more massive BH. Einstein Telescope is expected to detect IMRIs up to redshifts of $\sim 1 - 5$, depending on the mass and spin of the larger Black Hole [39], translating in an expected detection rate of tens or hundres IMRIs events per year [40].

Einstein Telescope could also allow to test the No-Hair theorem by looking at quasi-normal modes, the superposition of damped sinusoids that constitutes the Gravitational Wave signal of an asymmetric Black Hole evolving towards the spherical shape. Informations on quasi-normal modes are buried in the last instants of a Gravitational Wave signal, when the merger of two compact objects has happened and the resulting Black Hole rapidly radiates away the residual potential energy stored in its asymmetric mass distribution, in what is known as the ringdown phase. As a consequence of the No-Hair, which states that a Black Hole can be completely characterized by just three externally observable variables (mass, electric charge, angular momentum), the frequencies and time-constants of the quasi-normal modes depend only on same three observables. The No-Hair theorem could be tested by comparing the mass and spin parameters of the final Black Hole obtained from quasi-normal modes fitting with the same parameters inferred from the inspiral and merger dynamics, searching for eventual departurtures.
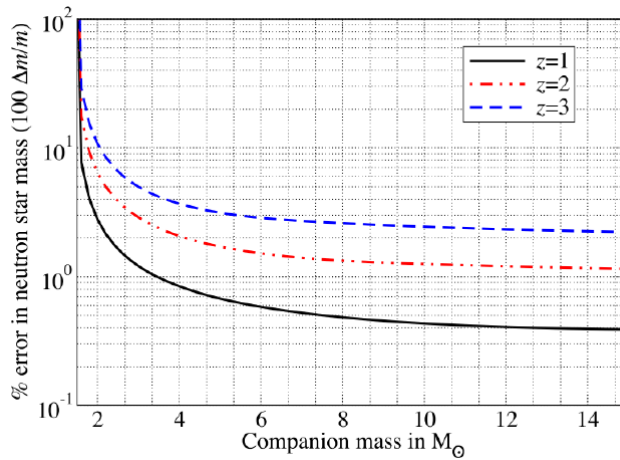

Figure 4.5: ET Accuracy of the NS mass determination in a NSBH merger as a function of the BH mass and for different redshifts. The Neutron Star mass is assumed to be $M_{NS} = 1.4 M_\odot$.

Limits on the maximum mass of a compact star   There exist several theoretical upper limits on the mass of a compact system before it encounters instability due to the fact that the gravitational pressure overcomes the degeneracy pressusure of stellar fluid. The most known examples are the Chandrasekar limit for White Dwarfs ($M_{Chand} \approx 1.4 M_\odot$) that are sustained by electron degeneracy pressure and the Tolman–Oppenheimer–Volkoff limit for Neutron Stars ($M_{TOV} \approx 2.2 - 2.9 M_\odot$) that are sustained by neutron degeneracy pressure. This limits this limits are also dependent on the stellar fluid Equation of State, the conditions of which cannot be reproduced and studied with current experimental techniques. The direct observation of BNS or NSBH mergers by the Einstein Telescope could provide a valuable insight on the properties of compact astrophysical objects.

Fig.4.4 shows the maximum distance to which compact binary inspirals are expected to be seen in Einstein Telescope for systems with two equal mass companions[6]. In particular Eintein Telescope is expected to observe NSBH merger events up to several units of redshift, translating in a $10^5 - 10^6 \, \mathrm{yr}^{-1}$ detection rate. In addition, the diagram in Fig.4.5 shows the accuracy with which the mass of a Neutron Star can be determined in an NSBH inspiral as a function of the companion mass and redshift, for an instrument with the sensitivity of Einstein Telescope. As the large majority if the confirmed mergers events in the advanced detectors host Black Holes with masses $M \geq 4 M_\odot$, it is expected that ET could determine Neutron Star masses with few percent accuracy up to $z = 3$ redshift.

4.3.2   Astrophysics

Einstein Telescope will be a unique observatory to study Neutron Stars and Black Holes dynamics, compositions and distribution as it will be sensitive to a large variety of relativistic phenomena in addition to the many compact binary mergers that are already revealed by the second generation detectors. Examples include quakes in Neutron Stars, Supernovae, Proto-Neutron Stars formation and Gamma-Ray Burst sources. In the following section it is presented what the Einstein Telescope can unveil about this compact objects and their enviroments.

Neutron Star Physics   The detection of Gravitational Waves from BNS mergers will provide a wide variety of physical information on the progenitor stars. It is particularly important to gain an insight on the Equation of State of bulk stellar matter in the extreme pressure and temperature conditions that are reached in the core of Neutron Stars and even more during the BNS merger phase. The behaviour of nuclear matter in this enviroments is currently not well understood and measurements of Gravitational Wave signals from NS sources can usefully constrain its Equation of State.

The Neutron Star Equation of State leaves its signature not only in BNS and BHNS merger signals but also in the peak frequencies of supernova waveforms, in the magnitude and damping time of NS crust mountains or in NS glitches and other oscillation mode excitations. Fig.4.6 illustrates the differences in the Power Spectral Density of a BNS merger signal in the case the two components have a cold (blue solid) or hot (red dashed) Equations of State, comparing them to sensitivities of different generation detectors. Despite the fact that this are the two extremal cases for the EoS of neutral matter, it is clear that the observation of several high-SNR BNS signals with the Einstein Telescope could provide decisive evidence to discriminate between different models.

Einstein Telescope data could also be crucial to shed light on the Neutron Star glitches enigma. Glitches are events in which a Neutron Star is seen to suddenly spin-up, followed by a relaxation period towards stable secular spin-down. Hundreds of single glitches have been observed in the radio emission of pulsar and magnetars, while some Neutron Stars, like the Vela pulsar, exhibit regular large glitches with a fractional frequency change amplitude of the order of $O(10^{-6})$. The mechanisms that

---

[6]For a binary system with symmetric mass ratio $\eta = \frac{m_1 m_2}{(m_1+m_2)^2}$, the maximum expected observable distance would be smaller by a factor $\sqrt{4\eta}$.
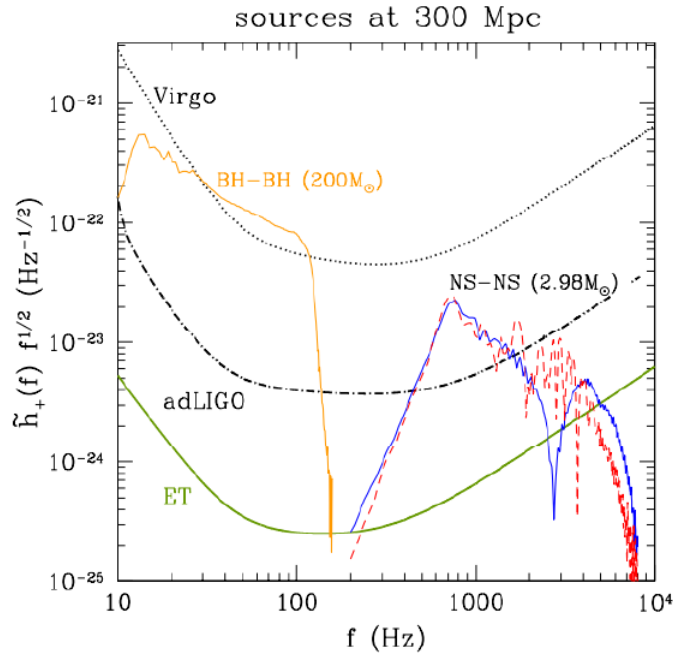
Figure 4.6: Gravitational wave spectra of BNS mergers compared to sensitivities of Virgo, aLIGO and ET, in the case the two components have a cold (blue solid) or hot (red dashed) Equations of State. Also shown for comparison is the corresponding spectrum of an equal-mass, non-spinning BBH (orange solid). Simulations from [41].

originate this phenomena remains a mistery to this day[7]. Einstein Telescope could provide an insight on the phenomena if Neutron Star sourced signals are detected in coincidence with an EM glitch, or it could set upper limits on the asymmetry of the process in alternative.

Rotating Neutron Stars may also suffer several instabilities that are associated with unstable modes of oscillations. Of special intrest are GW driven instabilities such as f-modes which deform the star into a bar-shape and r-modes which radiate predominantly through the current multipoles. Upon better understanding of the Neutron Star interior and consequent modelization, waveforms associated with glitches and instabilities can be obtained, enabling direct observation of the phenomena in the $[10 - 100]$ Hz frequency band of the Einstein Telescope.

Gamma-Ray Burst progenitors Gamma-Ray Bursts are the most energetic electromagnetic events that have been observed in the universe. They are classified either as short-hard or long-soft bursts depending on their duration and spectra. Long GRBs are associated with supernovae in late-type star-forming host galaxies while short GRBs are observed at lower redshifts inside a variety of galaxy types including early-type elliptical and lenticular galaxies without active star forming regions, so that it is thought that the progenitors of the latter type of events are BNS and BHNS mergers. A longer-lived optical afterglow is usually emitted at longer wavelengths, which allows to locate the host galaxy of the event.

Then the detection of BNS and BHNS mergers by the Einstein Telescope, in coincidence with electro-magnetical GRB events, could give a clearer picture of the mechanisms at the core of short Gamma-Ray Bursts. Predicting the Gravitational Wave emission of core-collapse supernovae associated with long GRBs is instead more difficult and involves modelling the complicated internal dynamics of the

---

[7]The favoured hypotesis is that glitches are associated to transfer of angular momentum between superfluid components of the star and/or the star crust and charged core [42]. Still the hydrodinamics and instabilities of this quantum superfluid system remain unmodelled.

collapsing star. In the absence of proper modeling of long GRB sourced Gravitational Wave signals, a less effective unmodelled source can be performed.

A significant fraction ($\sim 15\%$) of short GRBs may instead be associated with flaring activity in Soft Gamma-Repeaters. As the name suggests, these sources periodically emits long GRBs signals with luminosities of $L \sim 10^{41}\,\mathrm{erg\,s^{-1}}$ and photon energies in the range $[10-30]\,\mathrm{keV}$, accompanied by sporadic short GRBs with luminosities that can reach $L \sim 10^{47}\,\mathrm{erg\,s^{-1}}$. It is hypotized that SGRs are associated with sudden violent reconfigurations of complex magnetic field topologies inside magnetars, or alternatively to impacts of neutron stars with fossil disks around them.

Observations of quasi-periodic shear mode oscillations in Gravitational Wave signals in the $[10-40]\,\mathrm{Hz}$ frequency band, without an accompanying inspiral signal, could provide decisive evidence for the SGR model. Current models for SGRs indicate that they will emit less than $10^{46}\,\mathrm{erg}$ in Gravitational Waves [43]. Fig.4.7 shows the 90%-confidence level limits on the distances to which the ET detector will be sensitive to GW bursts with such energy. It can be noted as Einstein Telescope could enable the detection of extra-galactic SGR events.
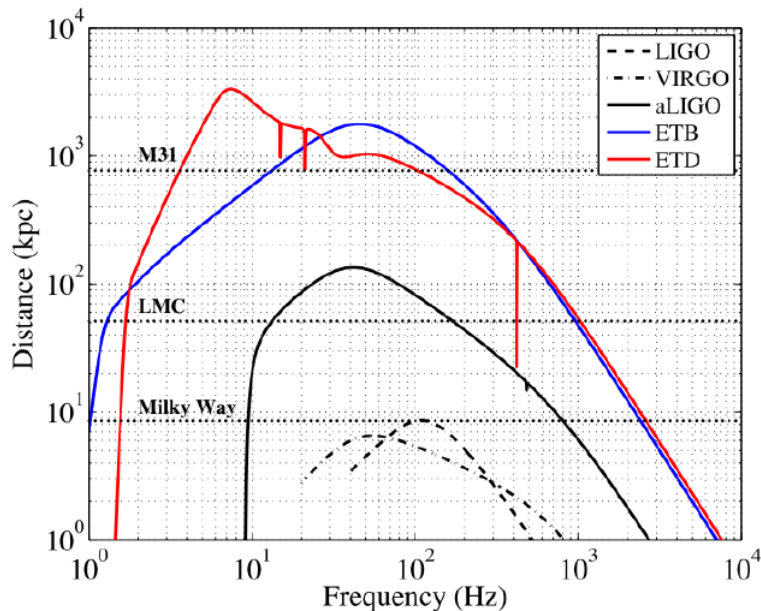

Figure 4.7: 90%-confidence lower limit on the observation range of various detectors for SGR sources with $10^{46}\,\mathrm{erg}$ enegry radiated as GWs. The solid horizontal black lines show the distances to various galactic locations (centre of Milky Way, Large Magellanic Cloud, M31 galaxy).

4.3.3   Cosmology and Cosmography

As stated in the introduction to Sec.4.3, Einstein Telescope could observe coalescence GW signals up to the edge of the Universe. By properly identifying the host galaxy of such events one can obtain reconstruct the evolution of the distributions of variuos GW emitting phenomena throughout the history of the universe. Einstein Telescope interferometers will also be sensitive to stochastic background radiation from primordial processes, thus providing an useful tool to investigate unanswered cosmological questions.

Compact Binary Coalescences as Standard Sirens   Estimates of astronomical distances are a non trivial task and rely on the elaborate Cosmic Distance Ladder system, which correlates short-range

methods, like parallax, with middle- and long-range methods that rely on various types of standard candles. There are several issues affecting these techniques, the most relevant of which regard standard candles, astronomical objects with known absolute magnitude: the theoretical debate on the 'standard-ness', that is the level of constancy of the absolute magnitude between different objects of the same type, is open for many candle candidates and beside this calibration and correct identification issues, especially in the case of object and galaxies at cosmological redshifts, add a significant contribution to the overall uncertainty of the estimate.

Accurate measurements of Gravitational Wave signals coming binary system inspirals could provide an independent method for estimating astronomical distances that does not suffer the main issues affecting the Cosmic Distance Ladder. Chirping signals from the coalescence of compact stars are then named Standard Sirens, as their amplitude depends only on a number of source parameters that can be directly inferred by looking at the waveform signature and on the luminosity distance. It is necessary to have system of at least three independent interferometers to fully disentangle the angular dependency of the Gravitational Wave signal, allowing for a correct sky location of the event and leaving the luminosity distance as the only free parameter left in the system.

The only contributions to the uncertainty of this kind of distance estimate come from detector calibration issues and SNR of the detected signal, plus systematic errors due to weak gravitational lensing. Moreover, there is no way to infer the redshift of the source from a Gravitational Wave signal.Then an accurate sky location of the signal is needed to identify the host galaxy of the event, the redshift of which can be extracted from electromagnetical observations.

Not only Standard Sirens would offer a powerful tool for cosmography, but they would also provide an independent technique to estimate the Hubble Constant H_0. This is because, at small redshifts ($z << 1$), the Hubble Law $D_L = c\,z/H_0$ that links the luminosity distance to the redshift of a specific source is valid, offering a new method to infer the Hubble constant by combining GW and EM observations of mergers event in our cosmic neighborhood. Other cosmological parameters, such as Ω_Λ, Ω_M and ω could be estimated starting from large catalogues of distant objects multimessenger observations, like GRBs progenitors discussed in Sec.4.3.2.

Cosmological evolution of compact object populations and coalescence rates Coalescence rate of compact objects is expected to be dependent on redshift. There are various features that contribute to the overall shape of the dependency and each one of them can be investigated with unprecedented depth with the Einstein Telescope. For instance the compact objects coalescence rate evolution throughout the history of the universe is affected by the following factors: the star formation rate history $SFR(z)$, the binary fraction $f_b(z)$, the formation efficiency of a given type of binary and their distribution of merger times. Einstein Telescope will be able to distinguish between coalescence rate predictions from different SFR models hence providing evidence for history of star formation, expecially at high redshifts where electromagnetical investigation becomes problematic.

Intermediate Mass Black Holes and Supermassive Blach Hole Seeds The Virgo and LIGO Scientific Collaboration have recently announced the first detection of a BBH merger that resulted in the formation of an Intermediate Mass Black Hole [44]. IMBHs are Black Holes with masses in the $[10^2 - 10^5]\,M_\odot$ range, that is significantly more than the few solar masses black holes directly formed in the star life-ending explosion and at the same time many orders of magnitude less than the Supermassive Black Holes at the center of the galaxies ($[10^2 - 10^5]\,M_\odot$). The GW190521 event observed in the aLIGO and AdV detectors is the first direct evidence for the existence of IMBHs. Still the mechanisms that lead to the formation of IMBHs remain debated. An in depth understanding of IMBHs abundancy and distribution throughout the history of the universe is also crucial to understand the mechanisms that lead to the formation of SMBHs.

Einstein Telescope will be the most efficient tool to investigate the nature of Intermediate Mass Black Holes. In particular, exploiting the cooperation of the Einstein Telescope with the LISA space-based

detector, an IMBH binary system coalescence event could be fully reconstructed from the inspiral phase, which Gravitational Wave emission is peaked in the sub-Hz band, to the final merger instants, which signal will instead enter the low-frequency detection band of the Einstein Telescope ($[1 - 10]$ Hz), as can be seen in fig.4.8.
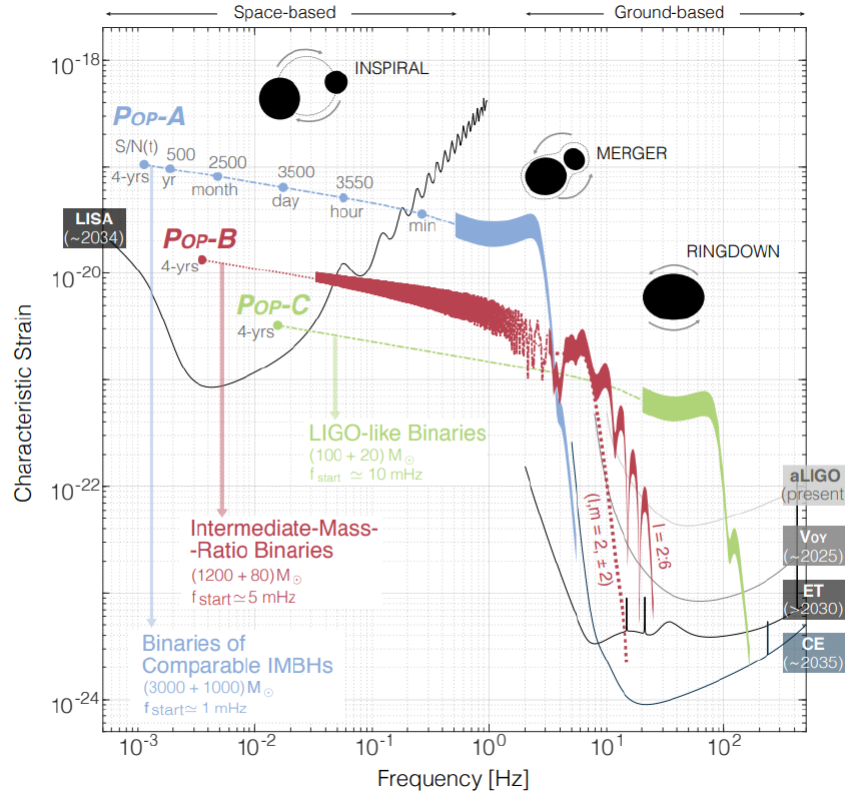

Figure 4.8: Power spectra of the inspiral, merger and ringdown signal from different types of binary IMBH at redshift $z = 0.5$, compared to the design sensitivity of the main space- and ground-based third generation detectors [45].

Primordial gravitational waves   Electromagnetical observations can directly probe the universe only up to to Recombination, as before this moment the primordial universe was populated by an hot ionized H-He plasma that was opaque to light. Gravitational radiation does not suffer screenings of any type so that it can freely propagate to us from the very first cosmic instants, potentially carrying direct informations on the early phases of the Big Bang up to the GUT scale of 10^{16} GeV. Various inflation models predict an almost scale-invariant Gravitational Wave spectrum, the amplitude of which is directly correlated to the scalar perturbation of the Cosmic Microwave Background via the Tensor-to-Scalar Ratio coefficient r. Combining the observed amplitude of the CMB electromagnetic spectrum and the more recent constraint on various inflation parameters that determine the final primordial GW spectrum [46], it is possible that a primordial GW background signal could overcome Einstein Telescope sensibility in the $f \leq 10$ Hz frequency band.

There are also other phenomena happening the very early universe that contributes to the generation of a primordial Gravitational Wave background, such as Cosmic String evolution or phase transition reheating and colliding bubbles. Einstein Telescope could also allow to empirically investigate for the first time all this new physics topics that are currently subject just to theoretical debate.

There is another important Gravitational Wave background that superimposes to the primordial one. That is a stochastic background originating from a large number of unresolved sources since the beginning of stellar activity. The main contributions to this astrophysical background come from BNS

coalescences, core collapse Supernovae, rotating Neutron Stars instabilities and triaxial emission. The detection of such a stochastic Gravitational Wave background with the Einstein Telescope would provide an unprecedented insight on the initial mass function and star formation history, along to cos-training physical properties of compact objects, but it could also constitute a noise source hiding the primordial GW background.

Part II

Chapter 5

The Thermal Noise Issue in a Cryogenic Interferometer

As seen in Ch.4, the Einstein Telescope will achieve a wider band sensitivity respect to second generation Gravitational Wave antennae by employing two interferometers for each one of its three planned detectors, separately optimizing each component of the pair for Low Frequancy or High Frequency detection (HF and LF, respectively). Different noise contributions affect the sensitivity of an interferometer across its frequency domain, so that different issues must be addressed to maximize the sensitivity in the two LF and HF interferometers.

The aim of this thesis work is to contribute to the research that is being carried out to improve the Low Frequency interferometer sensitivity in third generation Gravitational Wave detectors. The main noise contributions in the sub-10^1 Hz band comes from Seismic Noise, Thermal Noise and Newtonian Noise. While the latter is a fundamental noise that requires post-processing correlation of the interferometric signal with informations coming from arrays of independent detectors, the first two contributions are technical noises that can be lowered by means of better performing substrate materials, anti-reflection coatings and suspension systems for the test masses.

The Einstein Telescope design requires that, in order to tackle the Thermal Noise problem the Low Frequency detector will be operated at cryogenic temperatures. Considering the technological challenge related to cooling large volumes and masses to cryogenic temperatures, avoiding to inject back in the system mechanical noise due to cryocolers vibrations, the operating temperature designed for the LF detector is 10 K. This feature will drastically reduce Brownian Thermal Noise and Thermo-Elastic Noise in the test masses bulk and coatings, as manifestly shown in Eq.3.44 and Eq.3.48 where it was derived that the two contributions are respectively proportional to $S_x^{1/2} \propto T$ and $S_{TE}^{1/2} \propto T^2$. On the other hand this would have no direct effect on the Seismic Noise contribution.

The downside of operating an interferometer at cryogenic temperatures is instead indirect. In a low temperature detector, the last suspension stage is crucial in the determination of the total Thermal Noise not only for its mechanical losses but also because it needs to extract the thermal load that is put into the optical component by the laser beam. Unfortunately fused silica, the standard material employed in second generation GW detectors, has a very small thermal conductivity at low temperatures. It is also important to consider the temperature dependence of the Q factor of the canditate materials for a cryogenic operated detector. If the Q factor of a substrate or coating material lowers considerably for decreasing temperature, operating in a cryogenic environment will not result in thermal noise minimization, due to the fact that the thermal noise scales as T/Q.

On the contrary, crystalline materials have a very high thermal conductivity at low temperatures which makes them ideal substrate candidate for cryogenic detector suspension fibers. A comparison between the thermal conductivities of crystalline (Silicon, Sapphire) and amorphous (Fused Silica) materials can be seen in fig.5.1. A qualitative explanation for the low temperature thermal conductivity increase of crystalline materials can be given as follows. At high temperature the finite value of thermal con-
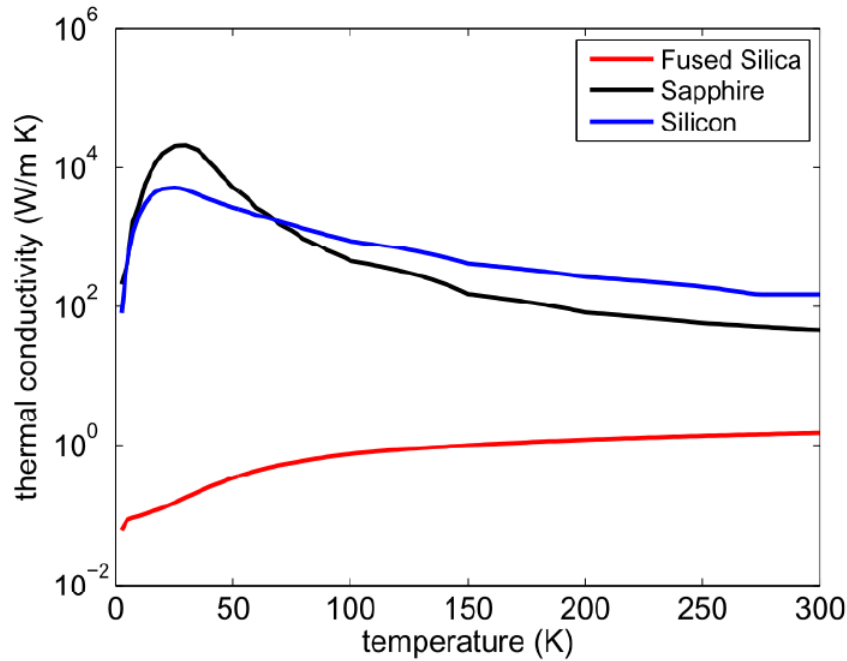
Figure 5.1: Thermal conductivities of various ET-LF detector test mass substrate candidates ([47], [48]).

ductivity is due to scattering of phonons amongst themselves via Umklapp processes. U-scattering cross section decreases exponentially with decreasing temperature. Then phonon mean free path increases and as a consequence thermal conductivity rises at low temperatures, reaching a maximum at around $0.05\theta_D$, where θ_D is the Debye temperature of the crystal. At lower temperatures the thermal conductivity falls as T^3, mirroring the temperature dependence of specific heat, due to the fact that the phonon mean free path becomes comparable to the crystal dimensions.

Crystalline materials thermal conductivity depends not only on the sample geometry and dimensions but also on the density of impurities and imperfections. Impurities and imperfections acts as scattering centers for the phonons, decreasing thermal conductivity. Their effect is most important where thermal conductivity peaks, as phonon-phonon U-processes and boundary scattering are relatively weaker in this temperature region (see Fig.5.2). Also the presence of different isotopes spoils the symmetry of the cristalline structure, affecting the final thermal conductivity of the sample.

There are also other parameters that must be considered in the choice for a ET-LF test masses and suspensions substrate besides thermal conductivity. Thermo-Elastic Noise is proportional to the square of the thermal expansion coefficient of the material $S_{TE}^{1/2} \propto \alpha^2$ (Eq.3.48) while mechanical losses of the substrate increase Brownian Thermal Noise in the suspensions. Another factor that plays a key role in the substrate material choice is the availability of large enough samples of the material to serve as interferometric mirror and recoil mass. Silicon is then the favored canditate for ET-LF test masses substrate as Sapphire is currently not available in large enough samples. Then Silicon should be preferred also as suspension substrate candidate, due to the fact that silicon-silicon bonds based on hydroxid-catalysis-bonding are stronger than sapphire-silicon bonds; furthermore a different thermal expansion coefficient between the two materials would cause further stress in the connection and bonding imperfections would contribute to increase the overall mechanical losses of the system.

Aside from the general motivations for substrate material choice in a cryogenic detector that were carried out in previous paragraph, additional care must be taken to assure that Silicon, the favoured candidate so far, could satisfy all the specific requirements of the Einstein Telescope Low Frequency interferometer.
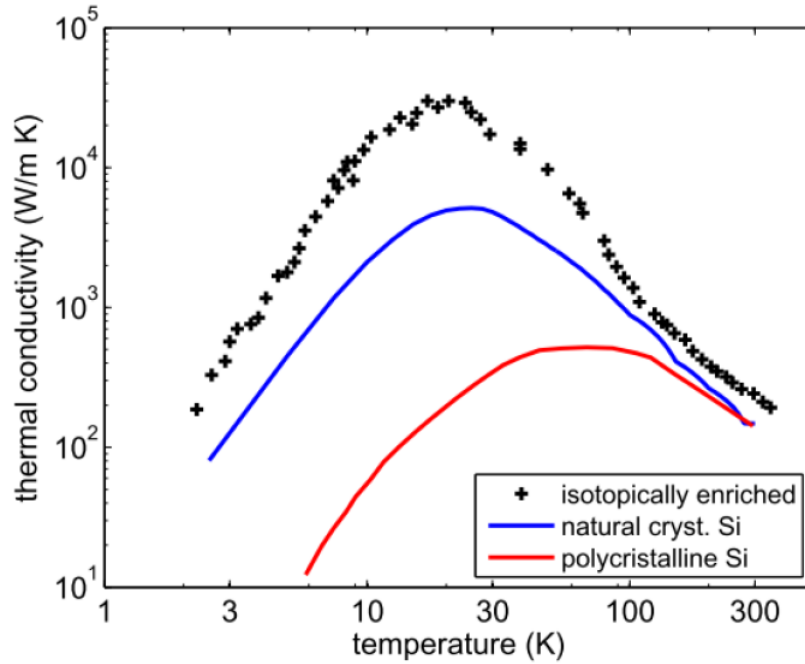
Figure 5.2: Thermal conductivity of polycrystalline Silicon compared to monocrystalline Silicon with different isotope fractions (Natural: $(92.2\% \, ^{28}Si, \, 4.7\% \, ^{29}Si, \, 3.1\% \, ^{30}Si)$; Enriched:$(100\%^{28}Si)$). Data from [47], [49].

The main design parameters for the High and Low Frequency interferometers of the Einstein Telescope are summarized in Tab.5.1. The reasons for the differences between the two interferometer have been explained in previous chapters. It should be noted that the shift to Silicon as mirror substrate material would require a shift also in the laser wavelength to $\lambda = 1550\,\mathrm{nm}$, due to the fact that crystalline Silicon is not transparent to $\lambda = 1064\,\mathrm{nm}$ light currently used in second generation interferometers. As a consequence, Erbium-Fiber lasers will replace Nd:Yag lasers in the Low Frequency interferometers. Of particular intrest for Thermal Noise computations are the circulating power inside the LF-interferometer arms and its mirror size. That is because in a real optical element, the Reflectance and Trasmittance do not sum up to unity due to a net optical absorption in the substrate that is proportional to the incident light power[1]. The larger the total absorbed optical power inside the mirror, the higher the stress that is put on the suspension fibers which are designed to extract the excess heat from the test mass system. This is a crucial issue in third generation cryogenic detectors, as Suspension Thermal Noise is expected to be one of the dominant noise contributions in the sub-10^1 Hz frequency region (Fig.4.3). Moreover the total heat capacity of the test mass system, that is proportional to the mirror mass, will determine the operating temperature of the mirror at a given absorption level, directly contributing to the total mirror thermal noise.

It is then of primary importance to obtain not only a characterization but also a deep understanding of the optical absorption process in candidate materials for the Einstein Telescope Low Frequency interferometer test masses at cryogenic temperatures. Still a detailed analysis of optical absorption in crystalline Silicon at cryogenic temperatures is lacking to this day.

Two different research groups investigated Silicon optical absorption at $\lambda = 1550\,\mathrm{nm}$ in the last decade obtaining somehow conflicting results, the first based at Leibniz University and Max Planck Institute in Hannover ([51], [52], [53]) and the second being a collaboration between scientists of the Laboratoire des Matériaux Avancés in Lyon and the Friedrich Schiller University in Jena ([54], [55]). While the first analysis pointed out that bulk absorption in crystalline Silicon substrates could reach values

---

[1]Or to the incident light power raised to an arbitrary power in the more general case of non-linear absorption.

Parameter	ET-HF	ET-LF
Arm Length	10 km	10 km
Input Power (after IMC)	500 W	3 W
Arm Power	3 MW	18 kW
Temperature	290 K	10 K
Mirror Material	Fused Silica	Silicon
Mirror Mass	200 kg	211 kg
Mirror Diameter / Thickness	62 cm/30 cm	min 15 cm/8 cm
Laser Wavelength	1064 nm	1550 nm
Beam Shape	TEM_{00}	TEM_{00}
Beam Waist	12 cm	9 cm
Scatter Loss per Surface	37.5 ppm	37.5 ppm
Filter Cavities	1×500 m	2×1000 m
Quantum Noise Suppression	10 dB FDS	10 dB FDS
Seismic Isolation	SA, 8 m tall	mod SA, 17 m tall

Table 5.1: Main design parameters for ET-HF and ET-LF interferometers (SA= SuperAttenuator, FDS=Frequency Dependent Squeezing). The parameters refer to the most recent ET-D design ([50]).

as low as $\alpha \leq 5$ ppm/cm [54], subsequent studies agreed on a different attenuation coefficient of $\alpha \approx 300$ ppm/cm, attributing the optical absorption to bulk [55] and surface [52] effects. It must be also noted that only [55] measurements are performed at cryogenic temperatures. This last result should be then given more importance, as the fragmentary evidences make it impossible to formulate a comprehensive theory that is capable to extend the room temperature values to cryogenic enviroments. This thesis work then aims at refining the present knowledge on crystalline Silicon optical absorption at $\lambda = 1550$ nm thanks to an independent direct measurement of the absorption coefficient, enabling the formulation of a coherent theoretical framework that is capable to explain Silicon optical absorption processes at various temperature scale and providing deciding elements for the substrate material choice in a third generation Gravitational Wave interferometer test masses.

Chapter 6

Experimental Set Up Design and Characterization

A cryogenic detetector such as Einstein Telescope Low Frequency interferometer requires very low overall absorptions in its optical elements. Test masses substrate candidates must ideally posses an absorption coefficient of few $\mathrm{ppm/cm}$. Measuring such a low levels of optical absorption is a non trivial operation: accuracies of commercially available powermeters reach at best few percentage points so that a direct measurment of a ppm power absorption in the sample is practically impossible. Moreover there exist no ready-to-use facilities or instrumentation that can provide a high accuracy optical absorption measurment in a cryogenic enviroment.

In the following chapter, we're going to present a technique for measuring crystalline Silicon optical absorbtion at $\lambda = 1550\,\mathrm{nm}$ and cryogenic temperatures.

6.1   The technique: calorimetric absorption measurements

The fraction of power absorbed by silicon α^* is given by the following relationship:

$$P_{abs} = \alpha^*_{Si} P_{in} \tag{6.1}$$

where P_{abs} is the power absorbed by the sample, while P_{in} is the total optical power input to the sample. The power balance for a system like the one in fig. 6.1 is:
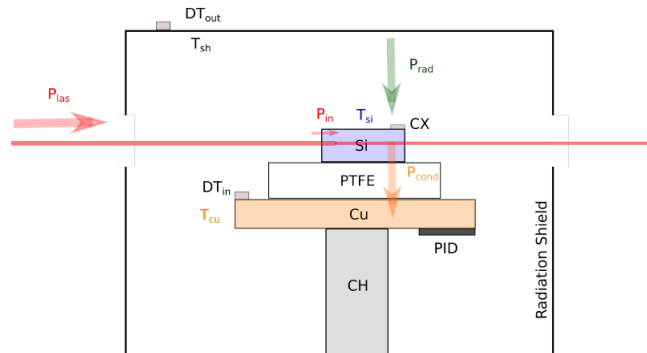

Figure 6.1: Schematic of the system

$$\kappa[T - T_{Cu}] - \sigma^*[T_{sc}^4 - T^4] + Mc_p\frac{dT}{dt} = P_{abs} \tag{6.2}$$

where Mc_p is the thermal capacity of the sample, $\sigma^* = A * \epsilon * \sigma$ (with A=sample surface, ϵ=Silicon emissivity and $\sigma = 5.76 * 10^{-8} \frac{W}{m^2 K^4}$ is the Stefan-Boltzmann constant), T_{sc} is the temperature of a thermal screen surrounding the sample and T_{Cu} is the temperature of the sample holder, which is thermally linked to the sample with a thermal conductivity κ.

When the beam is off and the system is in equilibrium $\frac{dT}{dt} = P_{abs} = 0$. The values at equilibrium of the sample, sample holder and thermal screen T_0, T_{0-sc}, T_{0-Cu} correspondent to this case, satisfy the equation

$$\kappa[T_0 - T_{0-Cu}] - \sigma^*[T_{0-sc}^4 - T_0^4] = 0 \tag{6.3}$$

Supposing that starting from this state, the sample is illuminated with a laser that is suddenly switched on, a power $P(t) = \theta(t)P_{abs}$ is injected, where $\theta(t)$ is the Heavyside step function. This will induce a variation of the three temperatures T, T_{sc}, T_{Cu} . Two assumptions can be made:

- $$T_{Cu}(t) = T_{0-sc}$$

- The temperature variation induced by $P(t)$ is small compared to the equilibrium temperatures from which we started. In other words

$$\begin{cases} T(t) = T_0 + \Delta T(t) & \Delta T(t) << T_0 \\ T_{sc}(t) = T_{0-sc} + \Delta T_{sc}(t) & \Delta T_{sc}(t) << T_{0-sc} \end{cases} \tag{6.4}$$

In this limit, the equation 6.2 can be linearized in ΔT and becomes

$$\kappa[\Delta T - \Delta T_{Cu}] - 4\sigma^*[T_{sc}^3 \Delta T_{sc} - T_0^3 \Delta T] + Mc_p \frac{d\Delta T}{dt} = P_{abs}\theta(t) \tag{6.5}$$

in another fashion equation 6.5 becomes

$$\kappa'\Delta T + Mc_p \frac{d\Delta T}{dt} = P_{abs}\theta(t) + 4\sigma^* T_{0-sc}\Delta T_{sc} \tag{6.6}$$

where $\kappa' = \kappa + 4\sigma^* T_0^3$
Experimentally we know that

$$\Delta T_{sc}(t) = \Delta T_{0-sc}[1 - e^{\frac{-t}{\tau_{sc}}}]$$

and typically $\Delta T_{sc} \approx 1K$ and $\tau_{0-sc} \approx 2000s$. Considering the homogeneous version of equation 6.6, the solution is

$$\Delta T_{homog} = Ae^{\frac{-t}{\tau}}$$

with $\tau = \frac{Mc_p}{\kappa'}$ As particular solution we can use

$$\Delta T_{part} = \Delta T_1 + \Delta T_2 e^{\frac{-t}{\tau_{sc}}}$$

and substituting it in eq.6.6 gives

$$\begin{cases} \Delta T_1 = [P_{abs} + 4\sigma^* T_{0-sc}^3 \Delta T_{0-sc}]/\kappa' \\ \Delta T_2 = [4\sigma^* T_0^3 \Delta T_{0-sc}\tau_{sc}]/[Mc_p - \kappa'\tau_{sc}] \end{cases} \tag{6.7}$$

Summing the homogeneous and the particular solution we have the final solution:

$$\Delta T(t) = \Delta T_1 + \Delta T_2 e^{\frac{-t}{\tau_{sc}}} - (\Delta T_1 + \Delta T_2)e^{\frac{-t}{\tau}} \tag{6.8}$$

where A was determined by the initial condition $\Delta T(t = 0) = 0$.
Let us now consider the derivative of $\Delta(T)$ at t=0. By deriving both sides of eq 6.8 we get

$$\left(\frac{d\Delta T}{dt}\right)_{t=0} = -\frac{\Delta T_2}{\tau_{sc}} + \frac{T_1 + T_2}{\tau} \tag{6.9}$$

Substituting from eq.6.1 and neglecting higher order terms we finally get:

$$\left(\frac{d\Delta T}{dt}\right)_{t=0} = \frac{P_{abs}}{Mc_p} = \frac{\alpha^*_{Si}}{Mc_p}P_{in} \tag{6.10}$$

Note that c_p, the specific heat of the silicon, depends on the temperature, especially at cryogenic temperatures. Since the variations in temperature to which our sample is subjected during irradiation are of the order of a few degrees in the first instance it was decided to neglect this variation. Therefore the total fraction of absorbed power is given by:

$$\alpha^*_{Si} = mMc_p \tag{6.11}$$

To obtain the absorption coefficient of the silicon we can consider the Lambert-Beer law:

$$P_{abs} = P_{in}[1 - e^{\alpha_{Si}*l}$$

where l is the optical path lenght of the beam inside the sample. Since in our case the absorption is very weak, we can linearize this equation, so that

$$\frac{P_{abs}}{P_{in}} = \alpha^* =_{Si} *l$$

Finally we have the simple equation:

$$\alpha_{Si} = \frac{m * M * c_p}{l}$$

6.2 Experimental setup

The aim of this work is to obtain a direct estimate of the crystalline Silicon optical absorption coefficient at cryogenic temperatures and for $\lambda = 1550\,\text{nm}$ light. In order to achieve this goal it is required to place a crystalline Silicon sample in a cryogenic environment, allowing for a $1550\,\text{nm}$ laser beam to pass through the test material while recording temperature changes of the sample. All the technical specifications of the analyzed Silicon sample are summarized in Tab.6.1.
All the technical specifications of the cryogenic system will be given in Sec.6.2.1 in addition to an in-depth account of calibration and characterization of cryogenic equipement (Sec.6.2.3, Sec.6.2.2) will present in detail the design process of the support system inside the cryogenic chamber, exploring the various thermodinamical and spatial constraints that had to be met in order to accomodate the sample above the cryocooler cold head. Design and characterization of the optical line are described in Sec.6.2.4. The presentation of the experimental set up will end with a brief outline of the Labview program that allowed to calibrate our setup and acquire the data.

---

[1]Normal to the main surface

Material	Crystalline Silicon
Growth Technique	Float-Zone
Doping Type	Intrinsic
Orientation[1]	$(1\,0\,0)$
Polished Surfaces	2
Resistivity	$> 500\,\Omega/\text{cm}$
x-axis Dimension (cm)	1.990 ± 0.005
y-axis Dimension (cm)	1.005 ± 0.005
z-axis Dimension (cm)	1.020 ± 0.005
Mass (g)	4.66 ± 0.01

Table 6.1: Parallelepipedal silicon sample technical specifications.

6.2.1 System Overview

The cryocooling apparatus we disposed of was a CTI-Cryogenics 8300 Compressor that employed a helium based thermodynamic cycle to perform heat extraction on a cylindrical cold head with diameter $d = 5cm$. The cold head was housed inside a CTI-Cryogenics vacuum chamber equipped with two CF-sealed 1550nm-coated optical windows and various access ports to allocate vacuum feedthroughs for thermometrical instrumentation and other electrical connections (see Fig.6.2). All the system was operated in high vacuum. In order to reach high-vacuum pressure inside the $0.1\,\text{m}^3$ CTI-Cryogenics chamber we employed a Varian Turbo-V 81-M turbo-molecular pump, in series with a pre-vacuum dry pump. We also installed a system of vacuum gauges that was able to monitor the chamber pressure.
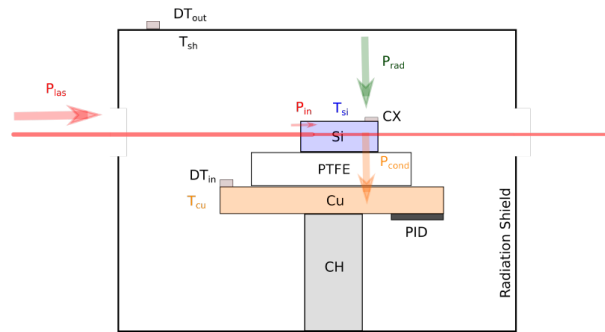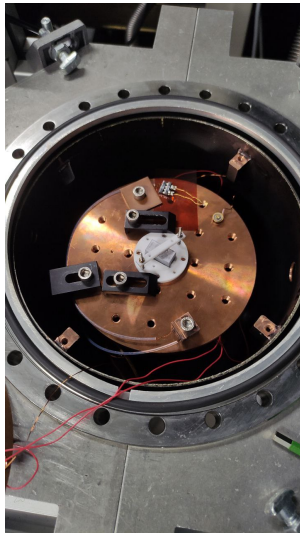

Figure 6.2: Left: Final set up of the cryogenic chamber interior; Right: Scheme of cryogenic chamber thermodynamics. Heat flow contributions: radiation heat flow (P_{rad}); conduction heat flow (P_{cond}); optical power of the laser beam at the input surface (P_{las}); optical absorption heat flow (P_{in}). Thermometers: in-loop DT-470 (DT_{in}) measuring copper support temperature (T_{cu}); out-of-loop DT-470 (DT_{out}) measuring radiadiation shield temperature (T_{sh}); CX-1050-SD (CX) measuting silicon sample temperature (T_{si}). Chamber parts and materials: cold head (CH); PID resistive heater (PID); copper (Cu); teflon ($PTFE$); crystalline silicon (Si).

In Fig.6.2 it can be also found a scheme of the system that was designed to house the Silicon crystal inside the cryogenic chamber. All the payload is enclosed inside the radiative shield, which is actively cooled. The supports and sample are mounted above the cold head. The copper support temperature

is stabilized to a constant value by a PID controlled resistive heater.

To fully monitor the temperature variation of the various system parts, three thermometers are employed: the in-loop LakeShore DT-470 thermometer is mounted on the copper sample holder to extract an error signal for the PID control; the out-of-loop LakeShore DT-470 thermometer is coupled to the radiation shield; the LakeShore CX-1050 thermometer is mechanically clamped on the sample upper surface to monitor temperature variations of the Silicon crystal by a suitably designed spring-loaded holder in teflon (PTFE). All the thermometers are wired with a 4-wire connection to the read-out instrumentation in order to bypass potential voltage drops that are happening in the wiring and assure to acquire an unbiased voltage signal.

DT-470 are diode thermometers so that they must be operated with a fixed excitation current to produce a temperature dependent voltage signal. They have a compact design allowing for easy clamping with a single M2 screw and they guarantee a fast response time which make them ideal to extract the error signal for the PID temperature stabilization system. A standard calibration curve for DT-470 thermometers which has $< 0.1K$ accuracy across all the operating temperature range is provided by the manufacturer. We disposed of two different Lakeshore thermometer reading instruments which were calibrated to convert the DT-470 voltage signal in a temperature measurement and which provided the proper excitation current for the thermometers; the Model 820 was employed to read the out-of-loop thermometer signal; the DR91C was used to acquire the in-loop thermometer signal and had a built-in anlog PID control system that allowed to stabilize the copper support temperature to the desired setpoint by sending a controlled current to the resistive heater.

LakeShore CX-1050-SD thermometer is instead an uncalibrated resistive thermometer and its resistance signal is acquired by an HP 3458A $6 - 1/2$ digit multimeter through a 4 wire connection. CX-1050-SD is much more compact than DT-470 thermometers, so that it can be directly installed on the sample. Its purpose is the direct measurement of the sample temperature increase upon absorption due to the laser beam and is therefore the most important sensor of the apparatus. To thermally couple the thermometer to the sample we opted for a mechanical clamping provided by a spring aided teflon cap. However for this thermometer a calibration curve was not available, so we needed to perform a preliminary calibration of the sensor, as explained below.

	DT-470	CX-1050-SD
Type	Diode	Resistive
Size	$\varnothing 7.95 \times 4.343\,\mathrm{mm}$	$3.175 \times 1.905 \times 1.080\,\mathrm{mm}$
Operating Range	$[1.4 - 500]\,\mathrm{K}$	$[0.1 - 325]\,\mathrm{K}$
Response Time[2]	$0.1\,\mathrm{s}$	$0.25\,\mathrm{s}$
Dissipation[3]	$17\mu\,\mathrm{W}$	$0.1\mu\,\mathrm{W}$

Table 6.2: LakeShore thermometers technical specifications.

6.2.2   Cryogenic Chamber Design

A fundamental requirement for the creation of a cryogenic environment for the study of Silicon crystal optical absorption is to set up a cryocooling facility that could accomodate the required sample housing and the thermometrical instrumentation, while disposing of a window system to allow for laser beam input and evacuation. The sample housing is specifically designed to partially decouple the Silicon crystal from the cold head of the cryocooling apparatus, so that the sample temperature can be set by

---

[2]At $T = 77\,\mathrm{K}$.

[3]At reccomended excitation and $T = 4.2\,\mathrm{K}$.

the thermal stage (at a price of a longer cooling time) and yet it is allowed to vary independently from the cold head temperature variations when heated by an external power source. This is achieved by inserting a layer of thermal insulating material between the crystal and the cold head wich sharply reduces the sample conductive heat dissipation; at equilibrium in cryogenic environment the dominant heat flow contributions on the sample becomes heat radiation to the chamber inner surfaces and thermal conduction to copper through teflon. To lower the sample equilibrium temperature as much as possible it is then necessary to encapsule the payload inside at least one radiation shield that prevents the sample to directly see the inner surface of the chamber at room temperature. The cryocooling apparatus should be properly dimensioned accordingly to the payload total thermal capacitance, to chamber heat dissipations and to the desired limit temperature on the sample.

The Silicon sample was placed along the optical axis of the chamber by means of a three stages support as shown in 6.3. The lower stage of the sample support is made of copper to ensure optimal thermal
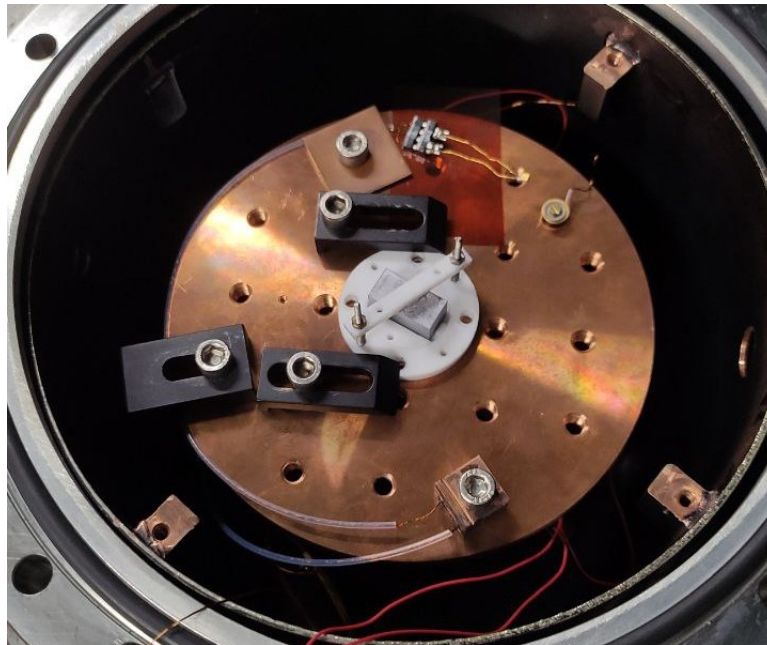
Figure 6.3: Three stage support and sample

coupling with the cold head. The CAD project with all the dimensions can be found in App.A.

The second stage of the support was made by two separate PTFE (teflon) pieces, a thermal insulating material which provides thermal decoupling between the silicon crystal and the copper plate. The stage is formed by an inner cylindric body that is concentrical to an outer toroidal piece; this configuration allows tu tune the orientation of the sample respect to the beam axis, so that the system could be positioned at Brewster Angle where beam reflections towards the radiation shield are minimized. The outer teflon support has only a structural function: it allows mechanical clamping of the upper stages of the sample housing to the copper support and cold head via four perpendicular $d = 4\,\text{mm}$ clearence holes; it is also equipped with four M2 threaded holes to allow for clamping of the third stage teflon cap. The inner teflon support instead houses the parallelepipedal crystal inside a dedicated socket. The area of contact between the sample and the support is reduced as much as possible to minimize conductive heat flow through teflon.

The third stage of the support consist of a teflon bar structure (teflon cap) which has the aim of keeping fixed the sample orientation respect to the beam axis during cooling phase. The bar is equipped with four $d = 2\,\text{mm}$ holes for screwing the piece to lower stages of the support. The contact area between the teflon cap and the sample is kept as small as possible to minimize conductive heat flow through teflon cap and screws towards copper. During developement phase the teflon cap also took on

a structural function, allowing for CX-1050-SD clamping to the crystal. This was achieved by placing the thermometer below the teflon cap contact surface and adding two M2 springs between the screw heads and the teflon cap upper surface.

6.2.3 CX-1050-SD Thermometer Calibration

Calibration of a resistive thermometer requires to obtain an unique and monotonical $T(R)$ function, taking advantage of a yet calibrated thermometer. To this purpose we clamped the resistive CX-1050-SD thermometer directly on thermal contact with the copper sample holder and used the in-loop DT-470 as a reference. In particular,the CX-1050-SD and DT-470 temperature acquisitions should be performed in equilibrium conditions after having stabilized the copper support temperature by means of the PID controlled resistive heater. This calibration technique was performed in the $T < 100\,\mathrm{K}$ temperature range. In a static calibration acquisition each $(T_{DT}\pm\sigma_T, R_{CX}\pm\sigma_R)$ data point is computed in the following way: both the in-loop DT-470 and the CX-1050-SD thermometer are installed on the copper support and the the copper temperature is stabilized at a given value with the use of the PID heaters. After equilibrium has been achieved the point $(T_{DT} \pm \sigma_T, R_{CX} \pm \sigma_R)$ is acquired.

With step of 5K the CX-1050-SD thermometer has been calibrated in the range [12-85]K. As a simple expression able to fit the observed datapoints, it was chosen an hyperbolic model, which was fitted to the data by performing an orthogonal distance regression method, in order to take into account both the incertitudes on R and T:
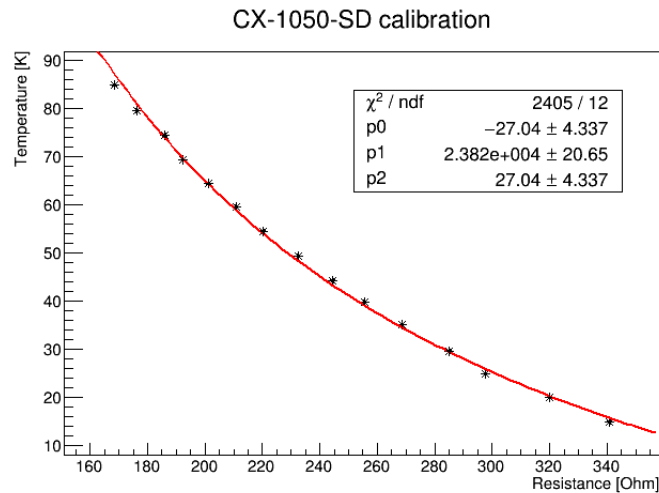
$$T(R) = p_0 + \frac{p_1}{R - p_2} \tag{6.12}$$
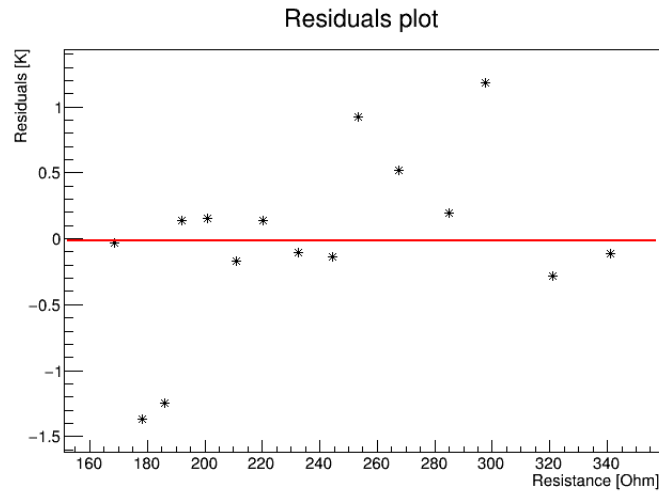

Figure 6.4: Hyperbolic fit of the data set

Figure 6.5: Residuals between the experimetal points and the fit hyperbolic function

From the residuals plot we decided to assume an a posteriori error of 1.5K for the temperature measurements obtained with the CX-1050-SD.

6.2.4 Optical Line

Optical elements   A simple optical line was set up to allow for $\lambda = 1550 \, \text{nm}$ laser beam alignment and polarization tuning. The $\lambda = 1550 \, \text{nm}$ source was provided by a Keopsys CEFL-KILO-05 Erbium fiber Laser. The Keopsys laser is equipped a feedback system that allows for $< 0.5\%$ RMS output power stabilization in the $[0.5 - 5] \, \text{W}$ range. A Faraday Isolator is installed after the fiber output to prevent beam reflection from reaching back the laser cavity. A Half-Wave plate (HWP) phase retardating plate is mounted before the Farady Isolator to control the ratio of the transmitted versus reflected power at Faraday Isolator. A small portion of the optical line is reserved for the insertion of the IR-photodiode for system calibration purposes. A complete scheme of the optical line can be found in Fig.6.6.
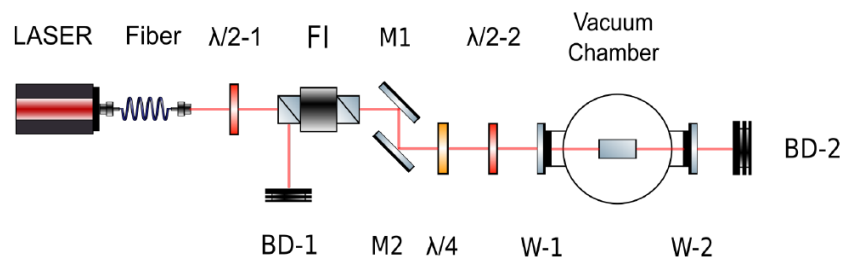

Figure 6.6: Schematic view of the optical line. $\lambda/2$: half waveplate; $\lambda/4$: quarter waveplate; FI: faraday isolator; BD: beam dump; M: mirror; W: window.

In order to properly perform an absorption measurement the optical line must met few crucial constraints. First of all we have to make sure that the laser beam enters and exits through the chamber interacting with anything but the sample, all reflections inside the cryogenic chamber must be minimized, in addition to prevent beam clipping phenomena, as any excess input power contribution would spoil the system thermodynamics when operated at cryogenic temperatures. In fact the aim of the experiment is to measure few ppm absorption on the silicon crystal, so that parasitic beam power heating

the chamber wall would increase the screen temperature, indirectly altering the sample temperature. Thus, alternative sample heating sources could easily dominate the absorption contribution and must be minimized.To this purpose the beam-sample system will be aligned at Brewster Angle to minimize the reflected power at sample input surface; a Qarter Waveplate-Half Waveplate system was installed just before the input window of the cryogenic chamber to control polarization ellipticity and orientation; the p-polarized beam is then accurately aligned respect to the sample input surface.

Beam characterization   Special care must be given to ensure that the beam is entering and exiting the sample in a central position respect to the sample surfaces, so that beam clipping on the sample is minimized. In order to further minimize beam clipping on the sample a focalizing lens with focal length approximately equal to the chamber radius should have been mounted in front of the entrance window, so to drastically reduce the radius of the beam that is entering the sample; as we did not dispose of a lens of such focal lenght, the only option to decrease the beam radius inside the sample was to reduce as much as possible the optical path of the line before the chamber.
It is then of primary importance to obtain informations on the spatial evolution of the beam radius along the optical line. It should be recalled that the sample input/output surfaces are rectangles of size $2 \times 1 \, \text{cm}^4$ and that the sample is entered at Brewster angle, that for Silicon at $\lambda = 1550 \, \text{nm}$ light corresponds to $\Theta_B \approx 74$. In order to comply with the 3σ rule for safe beam interaction with optical element, the largest beam radius that could be tolerated at input surface, accounting for the non-zero angle of incidence, is $r^{max} = \frac{l_x \cos(\Theta_B)}{6} \approx 0.9 \, \text{mm}$. As said, the only option that was available to reduce the beam radius in the sample region below this threshold was to minimize the optical line lenght.
It is then crucial to determine the spatial evolution of the beam radius along the line. CEFL-KILO fiber laser provides an highly collimated output. A knife edge test was performed at ten reference distances from the output fiber so to retrace the spatial evolution of the beam in between them. An exemplary edge test data is shown in Fig.6.7 along with a least square fit of the model describing trasmitted power for a partially shadowed beam:

$$s(x) = \frac{P}{2}\left[1 - \text{erf}\left(\frac{\sqrt{2}(x - x_0)}{w_z}\right)\right] \tag{6.13}$$

where x is the position of the scanning knife edge, x_0 is the center of the beam, P is the total power contained in the laser beam, and w_z is the $1/e^2$ beam radius at position z along the optical line.

The full set of data is reported in Tab. 6.3. A complete beam profiling was obtained by means of the software "Gaussian Beam" (6.8) and the the beam characterization is reported in Tab.6.4. As it can be seen, at the sample position ($z \approx 60cm$) the expected beam footprint on the sample surface is $1746 \pm 6 \, \mu\text{m}$, si that the 3σ rule is fulfilled.

---

[4]The $l_x = 2 \, \text{cm}$ side is placed parallel to the optical plane while the $l_y = 1 \, \text{cm}$ side is perperndicular.
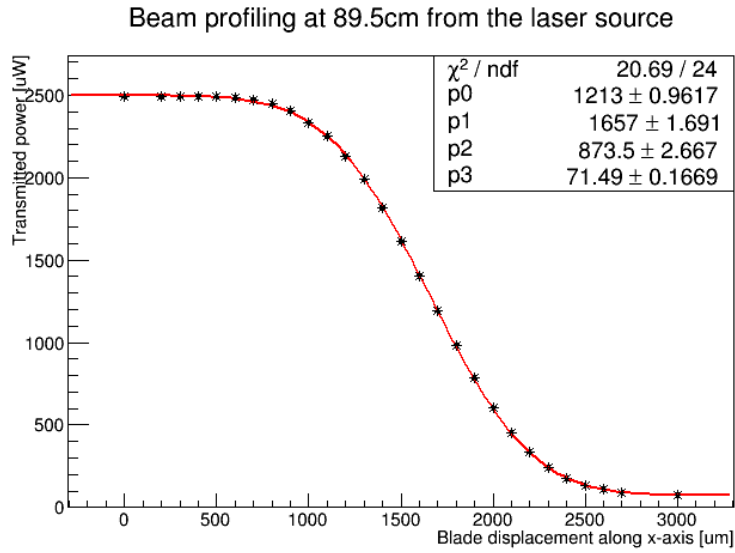
Beam profiling at 89.5cm from the laser source

χ² / ndf	20.69 / 24
p0	1213 ± 0.9617
p1	1657 ± 1.691
p2	873.5 ± 2.667
p3	71.49 ± 0.1669

Figure 6.7: Transmitted power versus knife edge position for tests performed at $z = 89.5\,\text{cm}$ distance from the fiber output.

z (cm)	Beam radius w_z (μm)
19.5	791 ± 3
29.5	805 ± 3
39.5	811 ± 3
49.5	830 ± 3
59.5	873 ± 3
69.5	833 ± 3
79.5	865 ± 3
89.5	874 ± 3
104.5	936 ± 3
119.5	990 ± 3

Table 6.3: Beam profiling

Optics	Position (mm)	Relative position (mm)	Properties	Waist (μm)	Waist position (mm)	Rayleigh range (mm)	Divergence (mrad)	Sensitivity (%/mm²)	Name	Lock
Input beam	234.431		n = 1, M² = 1	821.926	234.431	1369.25	0.600273	1.33396e-05	w0	absolute
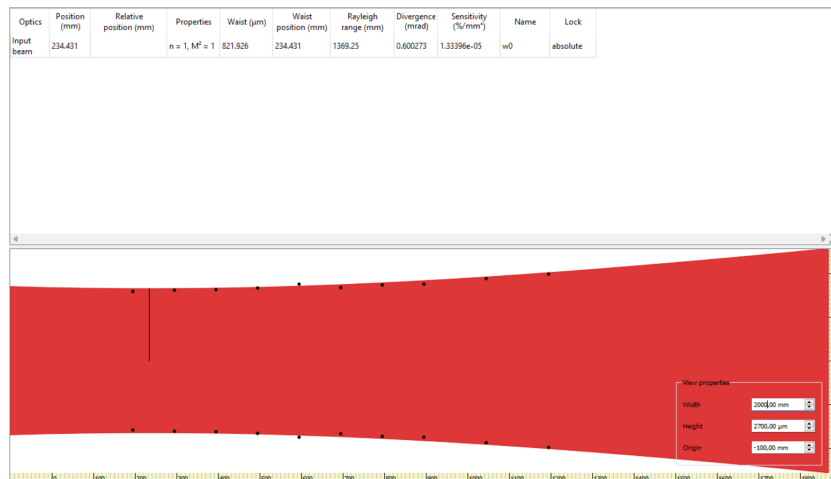
Figure 6.8: Simulation from the software "Gaussian Beam"

Waist position (cm)	Waist size w_z (μm)	Rayleigh range z_r (cm)
23.4 ± 0.1	822 ± 10	136.9 ± 0.1

Table 6.4: Beam profiling results

Power characterization   After having mounted the optical line, it was performed a characterization of the power transmitted by the optical windows and entering inside the vacuum chamber.This step was necessary because once the vacuum chamber is closed it is not possible to measure the power entering the sample. Given P_{out} the power output of the laser before the window of the vacuum chamber and P_{in} the power entering the sample, we expect:

$$P_{in} = p0 + p1 * P_{out}$$

. The result is reported in Fig 6.9 and from the fit we obtain a transmission coefficient of $(99.2 \pm 0.1)\%$ as expected from the manufacturer's specs, so that we can consider that the power entering into the chamber is equal to the one of the beam measured before the entrance window.
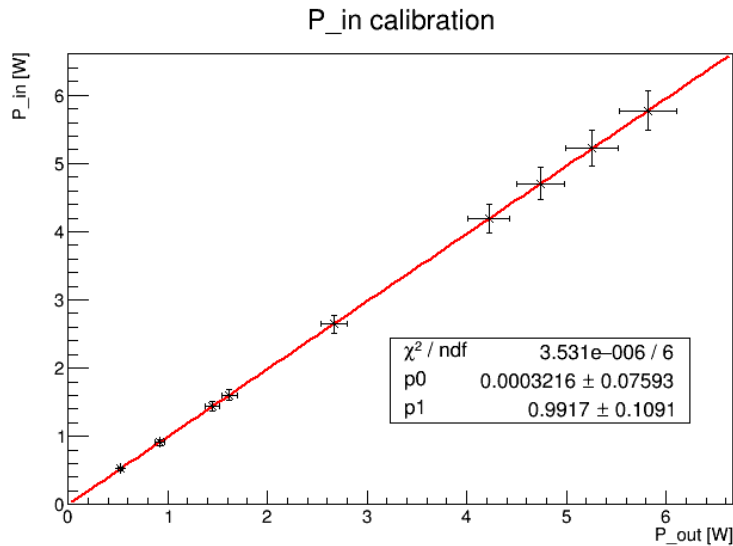
Figure 6.9: Power entering the sample calibration

6.2.5   Temperature variation without the sample

For the final absorption measurement, the thermometer will be clamped on the sample and since the sample is 1 cm high, the CX-1050-SD thermometer will be about 5 mm distant from the laser beam axis given that the beam passes in the center of the crystal.Since our technique assumes that the thermometer is measuring solely the sample temperature, it is important to ensure that no other phenomena may induce a parasitic heating of the CX-1050. In particular, given the high beam power and the low thermal capacity of the thermometer, one could imagine that the beam tails, or other light-driven secondary heatings are sufficient to change the thermometer temperature of an amount comparable to the quantity we want to measure. To check the heating induced by the beam tails, we removed the sample from the holder and we placed the thermometer at about 5 mm from the beam axis. then we switched on the beam at different powers (measured outside the vacuum chamber). In fig 6.10 an example of the output

graph of temperature variation at $P_{in} = 5.77W$. Two kinetics can be clearly distinguished, a fast one, with a duration of about 20 seconds and a slower one, which, in the time window of the experiment can be approximated with a linear growth $y = p_0 + p_1 * x$. The p_1 parameter represents the rate of temperature variation in K/s.
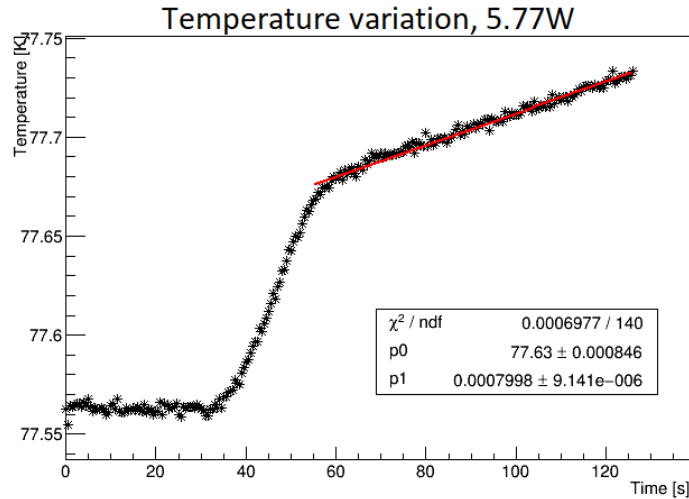

Figure 6.10: Temperature variation from the CX-1050-SD when the laser is 5mm distant from the thermometer

The slope of the slow heating kinetics is proportional to the beam power, as shown in fig. 6.11. This indicates that the heating is indeed provoked by some spurious illumination of the thermometer with the light beam. However, the dependency of this spurious heating rate on the laser power is $b = (1.24 \pm 0.02) * 10^-7 \frac{K}{s*mW}$. As it will be shown in the next paragraph, the heating rate vs power dependency measured when the thermometer is in contact with the sample is about one order of magnitude higher. We thus conclude that light-induced heating of the thermometer can account for about a 10% additional heating.
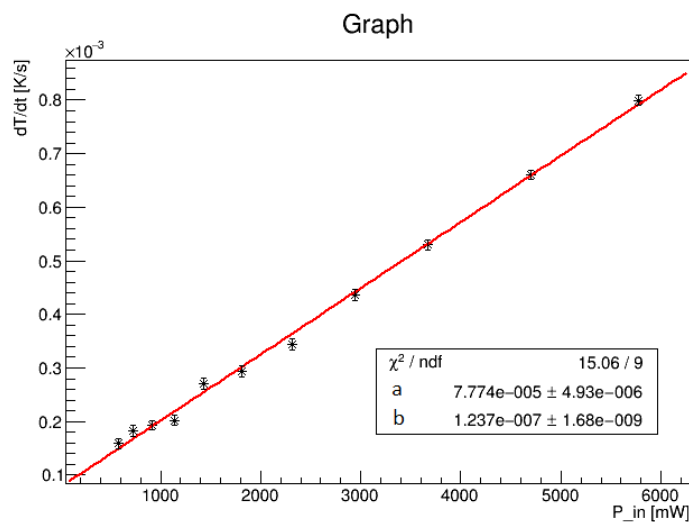
Figure 6.11: Rates of temperature variations at different input power

6.2.6   Experimental estimation of the Brewster angle

As a secondary check, we want to rule out the possibility that some radiation can induce a heating of the thermal shield inside the chamber. Due to the low temperatures and to the steep dependency of the Stefan-Boltzmann law on the shield temperature, even a modest temperature increase of the shield can provoke a measurable increases of the sample temperature. To carry out the absorption measurement, it was chosen to put the sample at the Brewster angle $\theta_{Brewster} \approx 74$, so that the incident radiation appropriately polarized in the horizontal direction (p-polarization) was not reflected from the surface of the sample. The angle was found by manually rotating the sample and checking with the powermeter
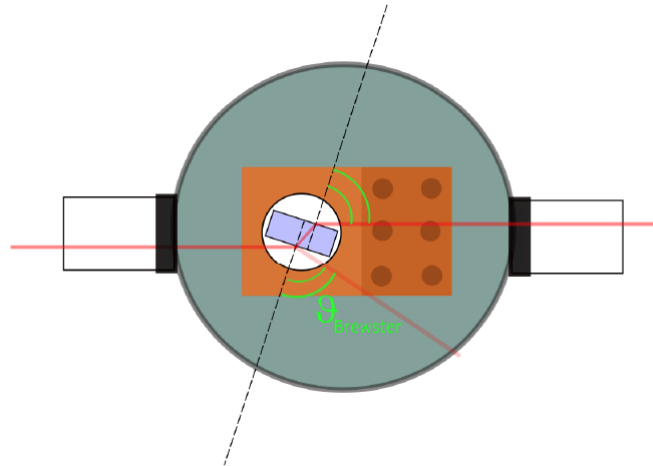
Figure 6.12: Scheme of the beam trajectory through the sample

that the reflected power was minimized. The minimum reflected power was about 0.03% of the incident power, so we proceeded to verify that this small fraction of power did not heat the vacuum chamber, which in turn would then irradiate the sample and heat it. To acquire this measurement we placed the sample at Brewster's angle and left the thermometer free to float, near the sample while laser was turned on.
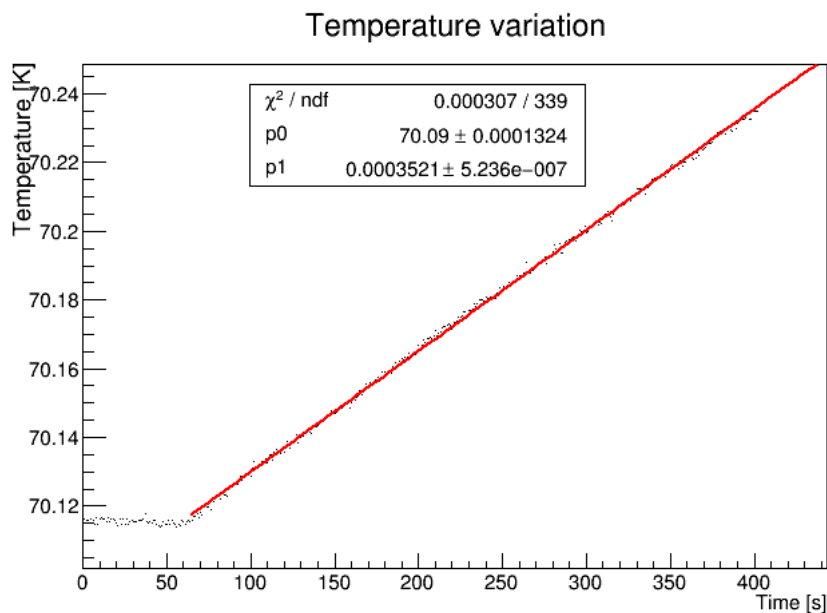

Figure 6.13: Temperature variation with floating thermometer near the sample

From the linear fit in 6.13 we see that the thermometer heats up with a rate of $(3.521\pm0.005)*10^{-4}\,\mathrm{K/s}$ when the input power is $P_{in} = 5.77W$. As we can see, the temperature increase is of the same order of magnitude of the one reported in fig. 6.10. However in that case the sample was not present in the chamber, while in this case the thermometer was kept well away from the laser beam. Therefore, we believe that fig. 6.10 and fig. 6.11 are displaying two different heating contributions, which we need to take into account in our measurements as a systematic overestimation of the sample absorption.

6.2.7 Digital Acquisition System

To carry out measurements through the acquisition electronics, programs were used in LabView. These programs have guaranteed the reading interface between the instrumentation and the user, via a laboratory PC with a GPIB connection. The diagram of the interface is shown below.
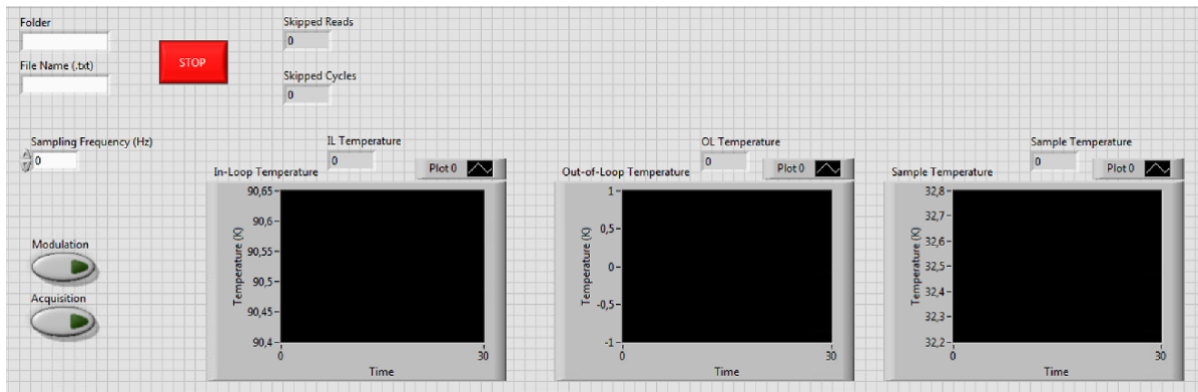

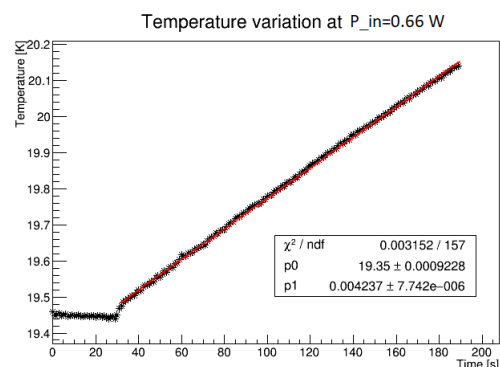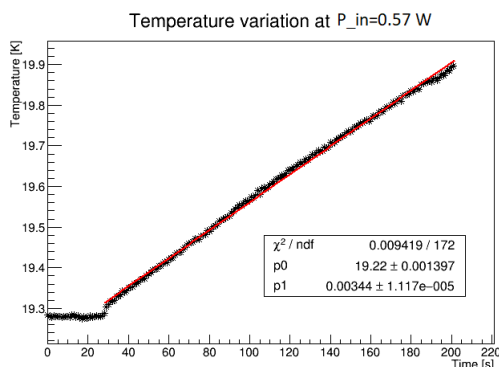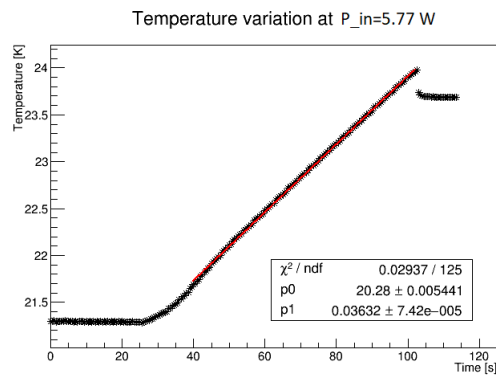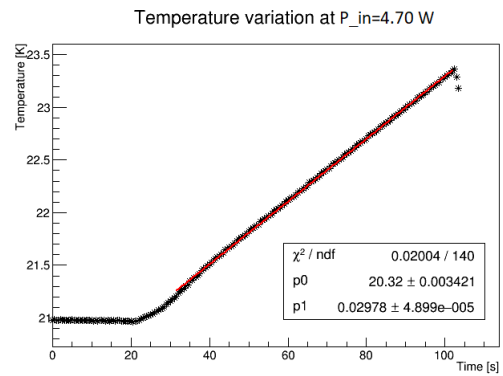Figure 6.14: Graphic interface of the acquisition program

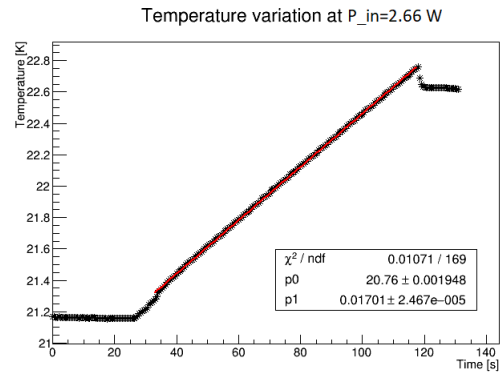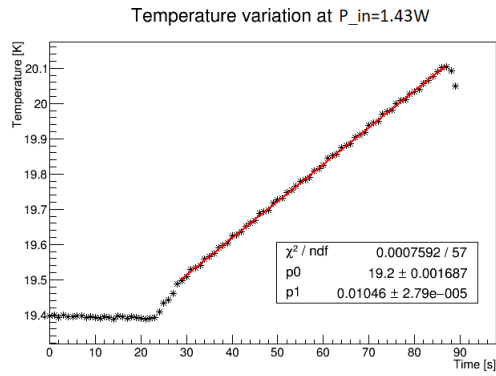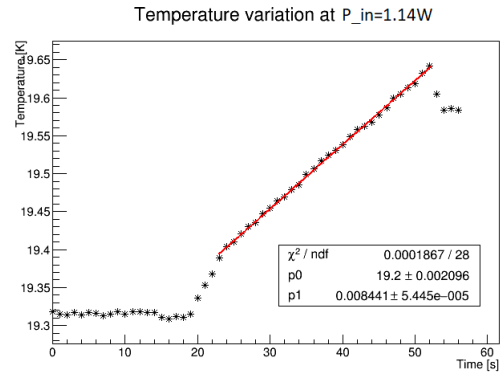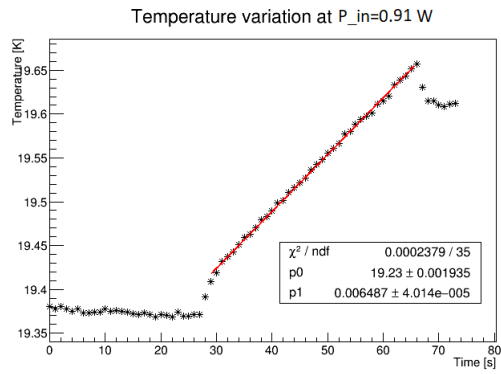# Chapter 7

Data Acquisition and Analysis

7.1 Impulsive measurement

As described in section 6.1 the optical absorption measurement of the silicon is obtained starting from the rate of change of the sample temperature immediately after the laser beam is sent through the sample itself. The measurement was carried out at two different temperatures of the sample $((20 \pm 1.5)K$ and $(32\pm1.5)K)$ to compare the absorption coefficient, expecting it to be the same thanks to the fact that the number of free carriers does not vary significantly. The figures below show the curves with the temperature measured with the CX-1050 thermometer thermally coupled to the sample. As soon as the beam is activated, an almost linear increase in temperature is observed. After some seconds the beam is blocked, so that the sample starts to cool again by exchanging heat with the vacuum chamber and with the cold head.

We proceeded with a linear fit, with the function $y = p_0 + p_1 * x$, of the temperature increase over time, for each different value of input power P_{in}, which was measured time by time, by checking the power of the beam outside the chamber. The window transmittance correction has been neglected, as reported in section 6.2.4. The graphs illustrating the various fits obtained and a summary table of the parameters of each fit are shown below. The error of the input power was obtained by propagating the power meter reading error (5% of the measurement) with the fit error for the P_{in} calibration in Sec.6.2.4.

Temperature variation at P_in=0.91 W
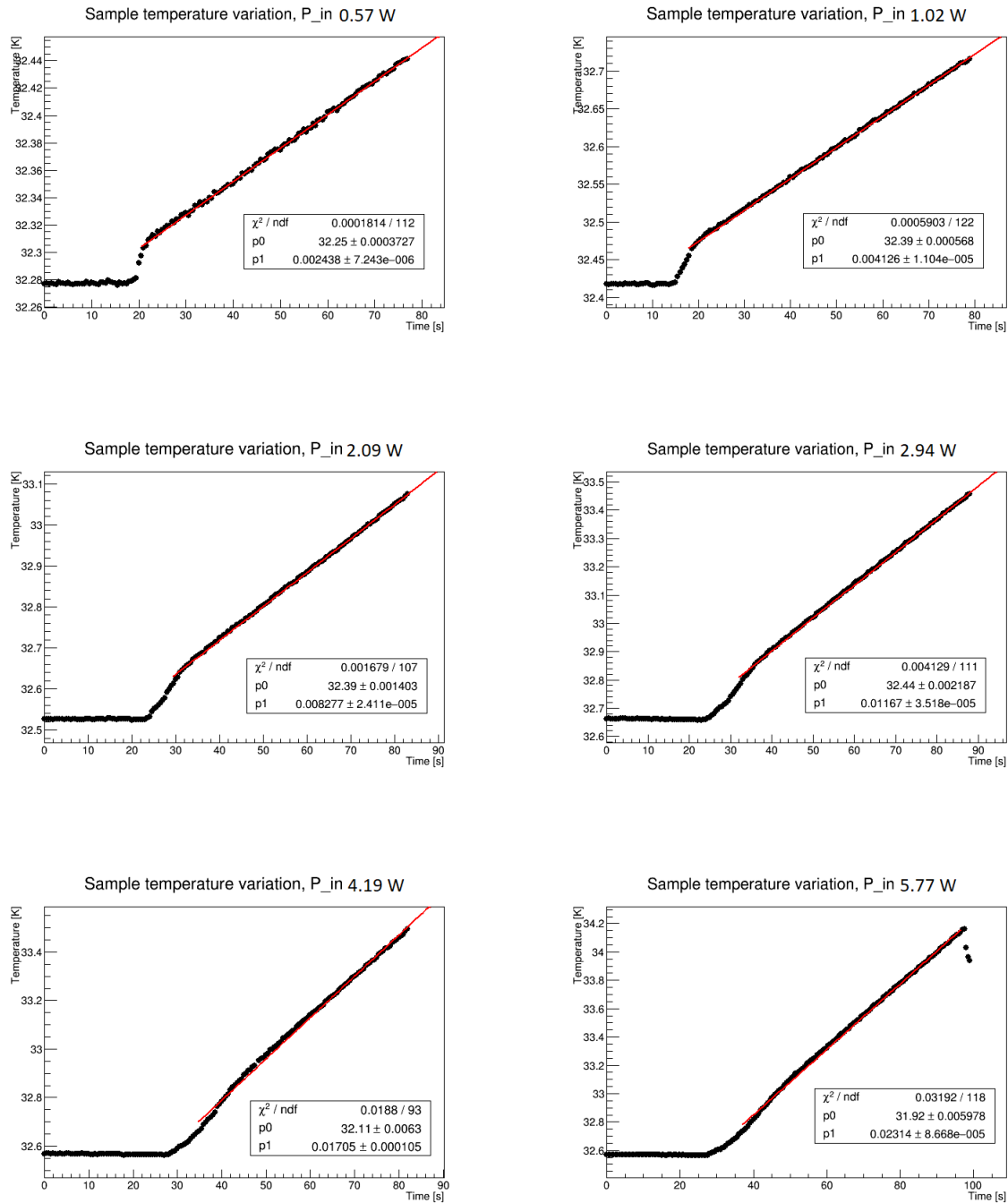

Temperature variation at P_in=1.14W

Temperature variation at P_in=1.43W

Temperature variation at P_in=2.66 W

Temperature variation at P_in=3.67 W

Temperature variation at P_in=4.70 W

Temperature variation at P_in=5.77 W
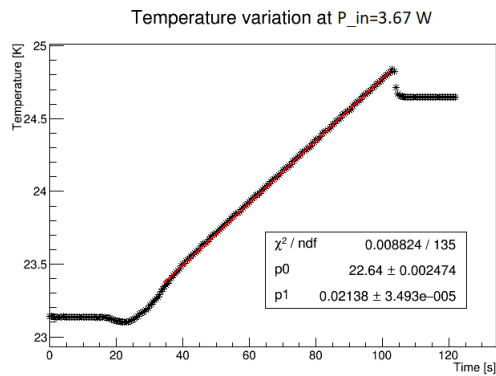
P_{in} (W)	p_0 (K)	p_1 (K/s)
0.57 ± 0.03	19.220 ± 0.001	0.00344 ± 0.00001
0.66 ± 0.03	19.350 ± 0.001	0.00424 ± 0.00001
0.91 ± 0.05	19.230 ± 0.001	0.00649 ± 0.00004
1.14 ± 0.06	19.200 ± 0.001	0.00844 ± 0.00005
1.43 ± 0.07	19.200 ± 0.001	0.01046 ± 0.00003
2.7 ± 0.1	20.760 ± 0.001	0.01701 ± 0.00003
3.7 ± 0.2	22.640 ± 0.001	0.02138 ± 0.00004
4.7 ± 0.2	20.320 ± 0.001	0.02978 ± 0.00005
5.8 ± 0.3	20.28 ± 0.001	0.03632 ± 0.00007

Table 7.1: Parameters from the linear fit of the sample temperature variation at different input power

The same acquisition was made at slightly higher temperatures and below the results are shown.

P_{in} (W)	p_0 (K)	p_1 (K/s)
0.57 ± 0.03	32.250 ± 0.001	0.00244 ± 0.00001
1.02 ± 0.05	32.390 ± 0.001	0.00413 ± 0.00001
2.09 ± 0.08	32.390 ± 0.001	0.00828 ± 0.00002
2.9 ± 0.1	32.440 ± 0.001	0.01167 ± 0.00004
4.19 ± 0.2	32.110 ± 0.001	0.0171 ± 0.0001
5.77 ± 0.3	31.920 ± 0.001	0.02314 ± 0.00009

Table 7.2: Parameters from the linear fit of the sample temperature variation at different input power

7.1.1 Absorption coefficient at $20 \pm 1.5\,\mathrm{K}$

For the acquisition done at about $20K$ is it possible to use the input power P_{in} and the coefficients p_1 shown in Table 7.1, corrected with the correction seen in sec. 6.2.5, to perform a fit of the equation 6.1. Thus performing a linear fit of eq. 6.1 it is obtained the graph shown in fig 7.1. Knowing the
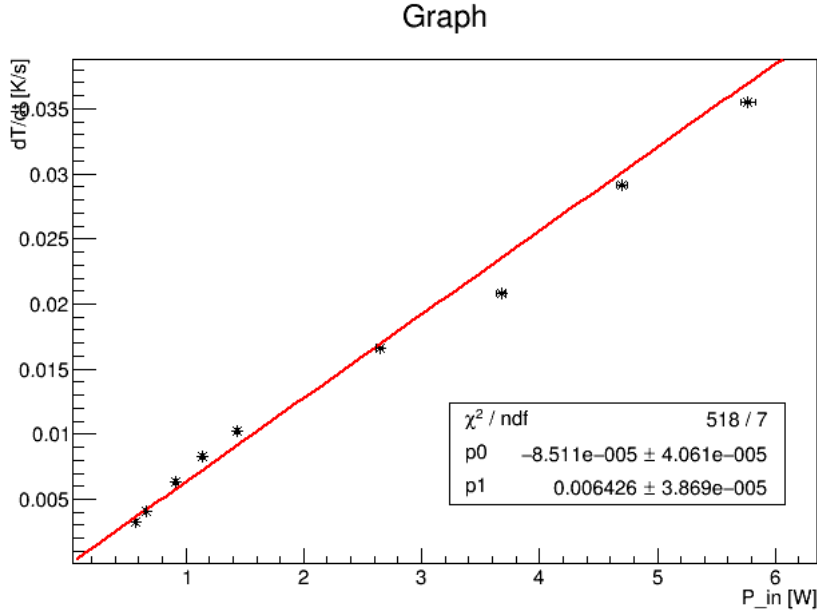

Figure 7.1: Temperature variation rate at different input power P_{in}

mass of the sample and using the specific heat c_p for cryogenic temperatures of the literature [62], it is possible to relate the p_1 coefficient of the fit in fig. 7.1 with the α^* seen in the eq. 6.12. Namely

$$\alpha^*_{Si} = p_0 M c_p \tag{7.1}$$

and propagating the errors of the three quantities in the above formula, it is obtained

$$\alpha^*_{Si} = (2.86 \pm 0.16) * 10^{-4} \tag{7.2}$$

To obtain the optical absorption coefficient of silicon per unit of length, it is sufficient to divide this value by the length of the optical path of the laser inside the sample $l = \dfrac{y}{cos(\theta_{refr})}$.

It is possible to obtain θ_{refr} from the Snell's law:

$$n_1 sin(\theta_{Brewster}) = n_{Si} sin(\theta_{refr}) \tag{7.3}$$

where n_1 is the refractive index of the vacuum, taken as equal to the unity, $\theta_{Brewster}$ is the angle of incidence of the beam entering the sample, n_{Si} is the refractive index of the silicon at the wavelength of $\lambda = 1550nm$ and θ_{refr} is the angle that the normal to the internal surface of the sample forms with the direction of the transmitted beam. For our setup we get:

$$\theta_{refr} = (16.03 \pm 0.08)$$

In which the error on θ_{refr} is obtained by propagation starting from the error of $\theta_{Brewster}$. Finally, the optical absorption measurement of the silicon at cryogenic temperatures was obtained:

$$\alpha_{Si} = \frac{\alpha^*_{Si}}{l} = (270 \pm 17)\frac{ppm}{cm} \tag{7.4}$$

7.1.2 Absorption coefficient at $32 \pm 1.5\,\mathrm{K}$

The same analysis was done at a slightly higher temperature using the parameters shown in Tab. 7.2, corrected with the correction seen in 6.2.5. The temperature variation rates versus the input power have been fitted with a linear function $y = p_0 + p_1 * x$. The fit is shown in the figure below. From
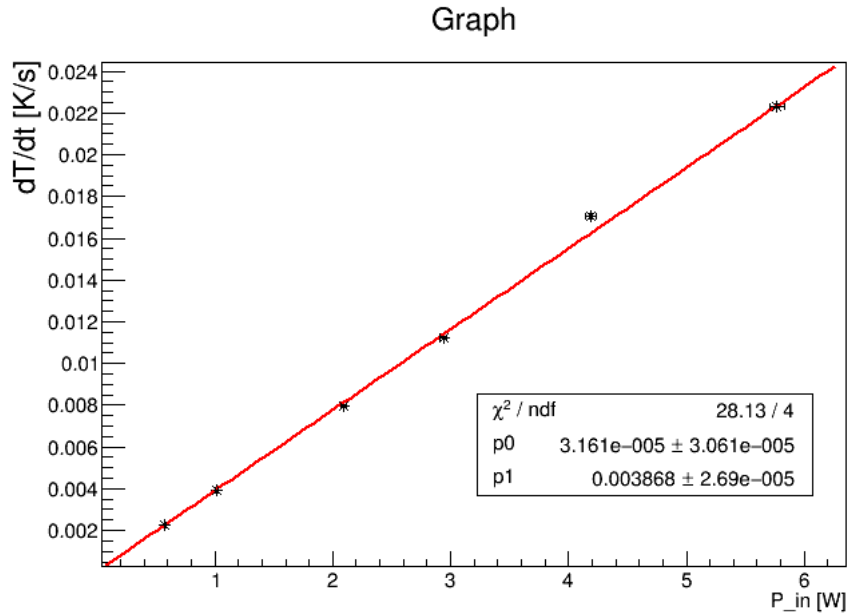

Figure 7.2: Temperature variation rate at different input power P_{in}

equation 7.1 it is obtained:

$$\alpha_{Si}^* = (3.01 \pm 0.19) * 10^{-4}$$

$$\alpha_{Si} = \frac{\alpha_{Si}^*}{l} = 284 \pm 18 \frac{ppm}{cm}$$

Chapter 8

Conclusions

Crystalline silicon is among the most favourite candidates to serve as test mass substrate material in third generation gravitational wave detectors. A summary of its excellent mechanical and thermal properties has been presented in Ch.5. Despite the large amount of literature on crystalline silicon properties that was prompted by a strong interest on the material by the telecommunication industry, little is known about its absorption spectrum at cryogenic temperatures with the sensitivity level demanded by gravitational wave detectors. To our knowledge, the only direct experimental evidence on silicon optical absorption for $\lambda = 1550\,\mathrm{nm}$ light in a cryogenic environment was obtained by [55], where it was found a nearly temperature independent optical absorption coefficient in the $[5-300]\,\mathrm{K}$ range with value: $\alpha_{Si} \approx 300\,\mathrm{ppm/cm}$. Assuming a highly pure, "perfect" material, this evidence was also in contrast with the existing theoretical expectations for a negligible optical absorption at low temperatures due to carrier freezeout.

In this thesis work, an apparatus for measuring optical absorption in Si at $1550\,\mathrm{nm}$ and in cryogenic conditions was optimized. The apparatus has been characterized and is able to measure absorption at the level of a few ppm/cm. This system will allow the study of silicon samples produced by various manufacturers with different techniques in order to determine the most suitable materials for use in ET.

The estimate provided of the optical absorption coefficient of the sample under examination is equal to:

$$\alpha_{Si}^{20K} = (270 \pm 17)\frac{ppm}{cm}$$

$$\alpha_{Si}^{32K} = (284 \pm 18)\frac{ppm}{cm}$$

The temperature variation of about $12K$ between one measurement and another does not involve a significant variation in the number of free carriers and this led us to think that the absorption coefficient should not change much between the measurement at $20K$ and that at $32K$. In fact the two absorption values coincide within the experimental errors, but they are still higher than the expected one. A reason for which the measurement is higher than the theoretical model could be attributed to the fact that the sample under analysis has undergone a polishing process that may have deposited on the sample elements with high absorption such as metal impurities (Fe, W , etc.), thus altering the surface and necessarily leading to an increase in the optical absorption coefficient. Given its inherently more defected nature with respect to bulk, the optical absorption component in the silicon due to surface effects (ref. [53], [52]) could make a major contribution compared to that of volume in the overall calculation of the optical absorption coefficient. Finally, our estimate of the absorption coefficient is also strongly influenced by the value of specific heat of the silicon used, so to improve the accuracy of the next experiments will be crucial to define a reliable estimate of this parameter in the samples considered.

8.1 Future prospects

Future prospects for the experiment will be based on a refinement of the already developed technique. Since the estimate obtained results to have a strong dependence on the specific heat considered, a refinement of the project under analysis will also pass through the direct measurement of the specific heat of the silicon samples used.The idea is to add a second laser line collinear with the probe one, in a range where Si is highly absorbing. In this way the system could be calibrated by comparing the measured temperature increase with the optical power, knowing that the latter is totally absorbed.
A further aspect that would be interesting to investigate concerns the development of techniques to isolate the contribution of surface absorption with respect to that of volume. This could be achieved by implementing the possibility of varying the section of the incident beam for the by keeping the beam power constant. In this way the surface contribution could be varied, while the volume contribution would remain constant, providing a way to separate the two contributions. A future prospect of the instrumental apparatus will also be to proceed with a systematic study of several silicon samples of the optical absorption coefficient at cryogenic temperatures, always at a wavelength of $1550 \, \text{nm}$.

Bibliography

[1] G.F. Smoot, J.L. Cervantes-Cota, S. Galindo-Uribarri, "A Brief History of Gravitational Waves", DOI: 10.3390/universe2030022.

[2] J. Weber, "Detection and Generation of Gravitational Waves" Physical Review, 1960.

[3] J. Weber, "Observation of the Thermal Fluctuations of a Gravitational-Wave Detector", Physical Review Letters, 1966.

[4] R. L. Forward, G. E. Moss, L. R. Miller, "Photon-Noise-Limited Laser Transducer for Gravitational Antenna", Appl. Opt. 10, 2495-2498 (1971).

[5] R. Weiss, Quarterly Progress Report 1972, No 105, 54-76. Research Laboratory of Electronics,MIT,`http://dspace.mit.edu/bitstream/handle/1721.1/56271/RLE_QPR_105_V.pdf?sequence=1`.

[6] LIGO Collaboration, "Sensitivity of the Advanced LIGO detectors at the beginning of gravitational wave astronomy", Phys. Rev. D 93, 112004.

[7] VIRGO Scientific Collaboration, "The Advanced Virgo detector", J. Phys.: Conf. Ser. 610 012014.

[8] LIGO Scientific Collaboration, "Observation of Gravitational Waves from a Binary Black Hole Merger", DOI: 10.1103/PhysRevLett.116.061102.

[9] R. Abbot et al., "GWTC-2: Compact Binary Coalescences Observed by LIGO and Virgo During the First Half of the Third Observing Run", arXiv:2010.14527.

[10] LIGO-VIRGO Collaboration et al., "Multi-messenger Observations of a Binary Neutron Star Merger", arXiv:1710.05833.

[11] R. v. Eötvös, Mathematische und Naturwissenschaftliche Berichte aus Ungarn, 8, 65, 1890

[12] E. Di Casola, S. Liberati, S. Sonego, "Nonequivalence of equivalence principles", DOI: 10.1119/1.4895342

[13] M. Maggiore, "Gravitational Waves: Volume 1: Theory and Experiments", OUP Oxford, 2007.

[14] S. Carroll, "Spacetime and Geometry: An Introduction to General Relativity", Pearson, 2013.

[15] R.X. Adhikari, "Gravitational Radiation Detection with Laser Interferometry", DOI:10.1103/RevModPhys.86.121.

[16] `https://science.gsfc.nasa.gov/663/research/index.html`.

[17] `https://www.lisamission.org`.

[18] R.N. Manchester, "Pulsar Timing Arrays and their Applications", AIP Conference Proceedings 1357, 65 (2011).

[19] J.E. Carlstrom, A.T. Lee, "Inflation Physics from the Cosmic Microwave Background and Large Scale Structure", DOI:10.1016/j.astropartphys.2014.05.013.

[20] LIGO Scientific Collaboration, "Advanced LIGO", DOI:10.1088/0264-9381/32/7/074001.

[21] M. Punturo et al., "The third generation of gravitational wave observatories and their science reach", DOI:10.1088/0264-9381/27/8/084007.

[22] A.E. Siegman, "Lasers", University Science Books, 1986.

[23] H.B. Callen, T.A. Welton, "Irreversibility and Generalized Noise", Phys. Rev. 83, (1951).

[24] Y. Levin, "Internal thermal noise in the LIGO test masses : a direct approach", DOI:10.1103/PhysRevD.57.659.

[25] M.L. Gorodetsky, "Thermal noises and noise compensation in high-reflection multilayer coating", DOI:10.1016/j.physleta.2008.09.056.

[26] G.M. Harry et al., "Thermal noise from optical coatings in gravitational wave detectors", Appl. Opt. 45, (2006).

[27] L.D. Landau, E.M. Lifshitz, "Theory of Elasticity, third edition", Pergamon, Oxford, 1986.

[28] V.B. Braginsky, M.L. Gorodetsky, S.P. Vyatchanin, "Thermodynamical fluctuations and photo-thermal shot noise in gravitational wave antennae", DOI: 10.1016/S0375-9601(99)00785-9.

[29] M. Cerdonio, L. Conti, A. Heidmann, M. Pinard, "Thermoelastic effects at low temperatures and quantum limits in displacement measurements", DOI:10.1103/PhysRevD.63.082003

[30] A. Freise et al., "Triple Michelson interferometer for a third generation gravitational wave detector", Class. Quantum Grav. 26 085012, 2009.

[31] S. Hild et al., "Sensitivity studies for third-generation gravitational wave observatories", DOI:10.1088/0264-9381/28/9/094013.

[32] B.S. Sathyaprakash et al., "Scientific Objectives of Einstein Telescope", DOI: 10.1088/0264-9381/29/12/124013.

[33] B.S. Sathyaprakash et al., "Cosmology and the Early Universe", arXiv:1903.09260.

[34] R. Schnabel, N. Mavalvala, D.E. McClelland, P.K. Lam, "Quantum metrology for gravitational wave astronomy", DOI:10.1038/ncomms1122.

[35] Y. Zhao et al., "Frequency-Dependent Squeezed Vacuum Source for Broadband Quantum Noise Reduction in Advanced Gravitational-Wave Detectors", DOI: 10.1103/PhysRevLett.124.171101.

[36] L. McCuller et al., "Frequency-Dependent Squeezing for Advanced LIGO", DOI: 10.1103/PhysRevLett.124.171102.

[37] R. Abbot et al., "Tests of General Relativity with GW150914", DOI: 10.1103/PhysRevLett.116.221101.

[38] Planck Collaboration, "Planck 2018 results. VI. Cosmological parameters", DOI: 10.1051/0004-6361/201833910.

[39] E. A. Huerta and J. R. Gair, "Intermediate–mass–ratio–inspirals in the Einstein Telescope: I. Signal–to–noise ratio calculations", DOI: 10.1103/PhysRevD.83.044020.

[40] J. R. Gair, I. Mandel, M. Coleman Miller, M. Volonteri, "Exploring intermediate and massive black-hole binaries with the Einstein Telescope", DOI: 10.1007/s10714-010-1104-3.

[41] L. Baiotti, B. Giacomazzo, L. Rezzolla, "Accurate evolutions of inspiralling neutron-star binaries: prompt and delayed collapse to black hole", DOI: 10.1103/PhysRevD.78.084033.

[42] G.B. McDonalds, "A Review of Pulsar Glitch Mechanisms", Ph.D. thesis, University of Johannesburg, 2007.

[43] B.J. Owen, "Maximum elastic deformations of compact stars with exotic equations of state", DOI: 10.1103/PhysRevLett.95.211101.

[44] LIGO Scientific Collaboration, Virgo Collaboration, "GW190521: A Binary Black Hole Merger with a Total Mass of $150 M_\odot$", DOI:10.1103/PhysRevLett.125.101102.

[45] K. Jani, D. Shoemaker, C. Cutler, "Detectability of Intermediate-Mass Black Holes in Multiband Gravitational Wave Astronomy", DOI: 10.1038/s41550-019-0932-7.

[46] Planck Collaboration, "Planck 2018 results. X. Constraints on inflation", DOI: 10.1051/0004-6361/201833887.

[47] Y. S. Touloukian, C. Y. Ho, "Thermophysical Properties of Matter; Vol.1 - Thermal Conductivity - Metallic Elements and Alloys" Plenum, 1970.

[48] Y. S. Touloukian, C. Y. Ho, "Thermophysical Properties of Matter; Vol.2 - Thermal Conductivity - Nonmetallic Solids" Plenum, 1970.

[49] T. Ruf et al., "Thermal conductivity of isotopically enriched silicon," Solid State Communications, vol. 115 (5), 2000.

[50] S. Hild et al., "Sensitivity Studies for Third-Generation Gravitational Wave Observatories", DOI: 10.1088/0264-9381/28/9/094013

[51] J. Steinlechner et al.,"Optical Absorption Measurements on Crystalline Silicon Test Masses at 1550 nm", DOI: 10.1088/0264-9381/30/9/095007.

[52] A. Khalaidovski, J. Steinlechner, R. Schnabel, "Indication for dominating surface absorption in crystalline silicon test masses at 1550nm", DOI: 10.1088/0264-9381/30/16/165001.

[53] A.S. Bell et al., "Anomalous optical surface absorption in nominally pure silicon samples at 1550 nm", DOI: 10.1088/1361-6382/aa8aac.

[54] J. Degallaix et al., "Bulk optical absorption of high resistivity silicon at 1550 nm", DOI: 10.1364/OL.38.002047.

[55] J. Degallaix et al., "Measurement of the optical absorption of bulk silicon at cryogenic temperature and the implication for the Einstein Telescope", DOI: 10.1088/0264-9381/31/18/185010.

[56] Y. Kraftmakher, "Modulation Calorimetry - Theory and Applications", Springer-Verlag Berlin Heidelberg, 2004.

[57] K.L. Hsu, D.E. Kline, J.N. Tomlinson, "Thermal conductivity of polytetrafluoroethylene", DOI: 10.1002/app.1965.070091106.

[58] N. Pearlman, P.H. Keesom, "The Atomic Heat of Silicon below $100\,\mathrm{K}$", DOI: 10.1103/Phys-Rev.88.398.

[59] R.J. Corruccini, J.J. Gniewek, "Specific Heats and Entalpies of Technical Solids at Low Temperatures", National Bureau of Standards Monograph 21, 1960.

[60] R. Hull, "Properties of Crystalline Silicon", INSPEC, 1999.

[61] B.J. Frey, D.B. Leviton, T.J. Madison, "Temperature-dependent refractive index of silicon and germanium", DOI:10.1117/12.672850.

[62] P.Flubacher, A.J. Leadbetter, J.A. Morrison "The heat capacity of pure silicon and germanium and properties of their vibrational frequency spectra"